OCT 1958

Journal of Research

of the

National Bureau of Standards

OF MICHIGAN
OCT 1958
PHYSICS
LIBRARY

JULY 1958

VOLUME 61 NUMBER 1

U. S. DEPARTMENT OF COMMERCE
Sinclair Weeks, Secretary
NATIONAL BUREAU OF STANDARDS
A. V. Astin, Director

JULY • 1958
VOLUME • 61
NUMBER • 1

JOURNAL OF RESEARCH
of the
NATIONAL BUREAU OF STANDARDS

The National Bureau of Standards

Functions and Activities

The functions of the National Bureau of Standards are set forth in the Act of Congress, March 3, 1901, as amended by Congress in Public Law 619, 1950. These include the development and maintenance of the national standards of measurement and the provision of means and methods for making measurements consistent with these standards; the determination of physical constants and properties of materials; the development of methods and instruments for testing materials, devices, and structures; advisory services to Government Agencies on scientific and technical problems; invention and development of devices to serve special needs of the Government; and the development of standard practices, codes, and specifications. The work includes basic and applied research, development, engineering, instrumentation, testing, evaluation, calibration services, and various consultation and information services. Research projects are also performed for other Government agencies when the work relates to and supplements the basic program of the Bureau or when the Bureau's unique competence is required. The scope of activities is suggested by the listing of divisions and sections on the inside of the back cover.

Publications

The results of the Bureau's work take the form of either actual equipment and devices or published papers. These papers appear either in the Bureau's own series of publications or in the journals of professional and scientific societies. The Bureau itself publishes three monthly periodicals, available from the Government Printing Office: The Journal of Research, which presents complete papers reporting technical investigations; the Technical News Bulletin, which presents summary and preliminary reports on work in progress; and Basic Radio Propagation Predictions, which provides data for determining the best frequencies to use for radio communications throughout the world. There are also five series of nonperiodical publications: The Applied Mathematics Series, Circulars, Handbooks, Building Materials and Structures Reports, and Miscellaneous Publications.

Information on the Bureau's publications can be found in NBS Circular 460, Publications of the National Bureau of Standards ($1.25) and its Supplement ($1.50), available from the Superintendent of Documents, Government Printing Office, Washington 25, D. C.

Order all publications from the Superintendent of Documents
U. S. Government Printing Office, Washington 25, D. C.

Use of funds for printing this publication approved by the Director of the Bureau of the Budget (May 14, 1956)

Journal of Research of the National Bureau of Standards Vol. 61, No. 1, July 1958 Research Paper 2877

The System Lime-Alumina-Water at 1°C

Elmer T. Carlson

A study was made of phase equilibria in the system CaO-Al_2O_3-H_2O at 1° C. The stable phases are believed to be gibbsite, tetracalcium aluminate hydrate, and $Ca(OH)_2$, but no solubility curve was established for gibbsite because of extreme slowness of reaction. The compound $3CaO \cdot Al_2O_3 \cdot 6H_2O$ appears to be metastable, being very slowly transformed to one or the other of the hexagonal hydrates. Metastable equilibrium curves were established for $CaO \cdot Al_2O_3 \cdot 10H_2O$ and $2CaO \cdot Al_2O_3 \cdot 8H_2O$. The concentration at their intersection (a metastable invariant point) is about 0.10 g of Al_2O_3 and 0.38 g of CaO per liter. The dicalcium compound can readily be dried to a $6H_2O$ stage, giving a characteristic X-ray pattern. During the long storage period required to approach equilibrium, most of the reaction mixtures picked up a little CO_2, apparently by absorption through the polyethylene containers, with formation of a carboaluminate, probably $3CaO \cdot Al_2O_3 \cdot CaCO_3 \cdot 11H_2O$.

1. Introduction

The system lime-alumina-water, largely because of its relation to the setting and hardening of hydraulic cements, is a field in which there has been a great deal of research over a period of many years. The literature on the subject has been thoroughly reviewed by Steinour (1951) [1],[1] by Bogue (1955) [2], and by Lea (1956) [3]. Extensive studies of phase equilibria in the system at room temperature have been reported by Bessey (25° C) [4], by Wells, Clarke, and McMurdie (21° C) [5], and by D'Ans and Eick (20° C) [6]. Equilibrium studies at temperatures from 50° to 250° C have been reported by Peppler and Wells [7] and at 100° to 1,000° C by Majumdar and Roy [8].

The phase diagrams given in the reports of the three investigations at room temperature are in fair agreement, in general; but all three are admittedly incomplete or uncertain in some respects, and on a few points there is direct conflict of opinion. Among the questions left unsettled are the following: (1) The existence of a hexagonal tricalcium aluminate hydrate, usually formulated $3CaO \cdot Al_2O_3 \cdot 12H_2O$. By many authorities such a compound is considered "well-established", and D'Ans and Eick [6] agreed with this view, though they did not attempt to show an equilibrium curve for it in their phase diagram. On the other hand, Wells, Clarke, and McMurdie [5] concluded that the supposed compound was actually a mixture of the dicalcium and tetracalcium aluminate hydrates. (2) The existence of more than one form of tetracalcium aluminate hydrate. This idea was first put forth by Assarsson [9], who concluded, on the basis of slight differences in index of refraction and X-ray pattern, that two very similar forms, which he termed α and β, existed at room temperature. D'Ans and Eick show widely different metastability areas for the two forms in their phase diagram, whereas Wells, Clarke, and McMurdie report only one form. (3) The area of stability, or metastability, of monocalcium aluminate hydrate. Although Assarsson [9] reported the formation of such a compound many years ago, its existence has been confirmed only recently, and none of the published phase diagrams shows any stability area for it.

[1] Figures in brackets indicate the literature references at the end of this paper.

The present study was undertaken in the hope of shedding some further light on the above questions, among others. The temperature, 1° C, was selected because Assarsson [9] had indicated that the formation of the monocalcium aluminate hydrate was favored by low temperature. Insofar as the information gained may be related to the practical problems of hydraulic cements, there is the further consideration that temperatures near the freezing point occasionally are encountered during the placing and hardening of such materials.

2. Experimental Work

2.1. Procedures and Materials

An ordinary household refrigerator, equipped with a special control device and a blower, served as a cold cabinet for storage of the reaction mixtures. The temperature was kept at 1° ±1° C, the relatively wide range being chiefly due to variations from point to point within the chamber rather than to the cycling interval. This range of temperature was acceptable because the solubilities change very little with temperature.

The primary starting materials were reagent-grade calcium carbonate, crystalline hydrated alumina (gibbsite), and distilled water. For most of the experiments the water was freshly boiled to expel carbon dioxide. Secondary starting materials, namely, calcium aluminates, were prepared by heating mixtures of calcium carbonate and gibbsite in the desired proportions. For the greater part of the subsequent work, a monocalcium aluminate preparation was desired that would yield a calcium aluminate solution of high concentration. This was obtained by heating the mix at 1,300° C. since preliminary experiments showed that the use of higher temperature, to effect complete combination, resulted in a comparatively unreactive product. In the preparation of calcium hydroxide solutions, calcium carbonate was converted to the oxide, slaked, shaken with water, and the mixture allowed to stand until it had settled clear.

When pulverized monocalcium aluminate is shaken with water it dissolves in amounts up to 2 g per liter or more, forming a solution slightly richer in lime than

469110—58——1

the parent solid, because of hydrolysis [10]. The solution thus formed is highly supersaturated with respect to certain hydrated compounds, but the initial rate of precipitation is slow, so that if the mixture is filtered after being shaken 30 to 60 minutes, the resulting filtrate will remain clear for several minutes or even hours. The same result can be attained somewhat more conveniently by substituting an an aluminous cement for the monocalcium aluminate. In the present study, however, the idea of using aluminous cement was abandoned when it was found that the cement at hand produced solutions containing an appreciable amount of sulfur as sulfide.

Supersaturated calcium aluminate solutions were prepared as described above, cooled in the refrigerator, and then mixed with varying proportions of previously cooled calcium hydroxide solution in 1-liter polyethylene bottles. These were stored in the cold-cabinet, shaken at intervals, and examined from time to time.

By similar methods the various hydrated calcium aluminates were prepared, filtered off, and used in subsequent experiments on solubility in water and in various concentrations of calcium hydroxide. Thus equilibrium was approached on the one hand from supersaturation, and on the other, from undersaturation. Additional solubility experiments were performed with $3CaO{\cdot}Al_2O_3{\cdot}6H_2O$ and $4CaO{\cdot}3Al_2O_3{\cdot}3H_2O$. These compounds were prepared hydrothermally, the first by heating a mixture of $Ca(OH)_2$ and gibbsite at 200° in the presence of water, the second similarly from $Ca(OH)_2$ and $CaO{\cdot}Al_2O_3$ at 250°.

Two methods of sampling the solutions for analysis were employed. If the solution was clear, the sample was taken directly with a pipet, usually 50-ml. If any turbidity was noted, the liquid was first filtered with the aid of a suction flask and a fritted glass crucible, fitted with a stopper and a tube that extended into the reaction vessel. Contamination with carbon dioxide thus was held to a minimum. (Filtration of lime solutions through fritted glass introduces a small error, apparently because of adsorption of lime on the glass. This error was disregarded, as in no case did it appreciably affect the position of the equilibrium curves.)

Aluminum and calcium oxides were determined by conventional methods. Because of the low concentrations, especially in the case of Al_2O_3, the errors were relatively high in the analyses of 50-ml samples; however, the final analysis in each case was done on a sample of 100 to 400 ml.

When portions of the solid were filtered off for analysis or examination they were not washed with water. Dissolution of the precipitate was thus avoided, and the minute amount of dissolved matter adhering to the precipitate was considered negligible. Usually the precipitates were dried in a desiccator containing calcium chloride and a CO_2 absorbent. More rapid drying, when desired, was accomplished by washing with alcohol and ether.

Precise determination of the optical properties of the hydrated calcium aluminate usually is difficult because of the minute size of the crystals, especially in the case of the plate-form phases. The crystals formed at 1° C were much smaller than those obtained under similar conditions at 25° C, so that identification by microscopic means often was impossible. X-ray diffraction, however, proved to be a very useful method for identification, even when several phases were present. The apparatus used was a Geiger-counter diffractometer, with copper $K\alpha$ radiation. The platy phases ordinarily were strongly oriented, and gave very strong reflections at the lower angles. With certain precipitates containing $2CaO{\cdot}Al_2O_3{\cdot}8H_2O$ it was found essential to obtain the X-ray pattern while the material was still damp, as important phase changes occurred on drying.

2.2. Solid Phases in the System CaO–Al_2O_3–H_2O

a. Hydrated Alumina

Various investigators [5, 6, 7, 10] have found gibbsite, $Al_2O_3{\cdot}3H_2O$, to be the stable form of hydrated alumina in this system at temperatures from 20° to 150° C. In the present study its stability at 1° C is assumed rather than proved. Actually, as suggested by D'Ans and Eick [6], the true stable phase may be anhydrous Al_2O_3 rather than gibbsite, but if so, the transformation does not occur even in geologic time. In the present study, gibbsite was identified in the precipitates from certain reaction mixtures, for example, No. 1 in table 3. In other cases, hydrated alumina in some form was believed present, even though the X-ray patterns gave no evidence of it. Occasionally, after filtration of a mixture, the filtrate would contain a little very fine suspended material, not readily soluble in dilute HCl. This was assumed to be alumina since all the other expected solid phases are readily soluble in acid. Again, the examination of one exceedingly finely divided precipitate (No. 1, table 2) under the electron microscope revealed aggregates of fibers believed to be alumina gel.

b. Calcium Hydroxide

This is a stable phase in the system at room temperature [5]. The solubility of coarsely crystalline $Ca(OH)_2$ in pure water was reported by Bassett [11] to be 0.130 g of CaO per 100-g solution at 0° C, and 0.128 at 5°. He also reported values of 0.143 and 0.151 for finely crystalline $Ca(OH)_2$ at 0° C. The marked effect of particle size on the solubility of $Ca(OH)_2$ at somewhat higher temperatures has been critically studied by Hedin [12]. In the present study no attempt was made to fix the solubility precisely, since the particle size was not subject to control. The value 1.30 g of CaO per liter at 1° has been accepted on the basis of Bassett's data.

c. $3CaO{\cdot}Al_2O_3{\cdot}6H_2O$

The isometric crystalline compound of composition $3CaO{\cdot}Al_2O_3{\cdot}6H_2O$ has been shown to be a stable phase in the system CaO-Al_2O_3-H_2O at temperatures from 20° to 200° C [4, 5, 6, 7, 8]. As will be brought out later, it probably is not a stable phase at 1° C.

d. $CaO \cdot Al_2O_3 \cdot 10H_2O$

Hydrated monocalcium aluminate was described, and its composition discussed, in an earlier paper [13]. It exists as a metastable phase in the system at 1°. It was obtained as crystals ranging from about 25μ down to submicroscopic size in different preparations. The larger crystals were well-developed hexagonal prisms with flattened terminal pyramids.

e. $2CaO \cdot Al_2O_3 \cdot 8H_2O$

Dicalcium aluminate hydrate, crystallizing in hexagonal plates, is a well-established metastable phase in the system at room temperature, and, with decreasing stability, even as high as 90° C [4, 5, 6, 7]. Whether the crystals really are hexagonal or of lower symmetry is not definitely known [1]. Despite this uncertainty, the phase is generally referred to as hexagonal, and this usage will be followed herein. McMurdie [5] indexed the X-ray lines on the basis of hexagonal symmetry, and his indices of 001 and 002 for the first two reflections will be adopted in the following discussion. Although the formula commonly adopted shows 8 molecules of water, the water of hydration is known to vary somewhat with the degree of drying. According to Salmoni [14] the fully hydrated compound may contain 11 molecules of water, but this can be reduced to 7 by drying the compound over $CaCl_2$, and to 5 by heating at 100°, without essential change in the crystal structure. Further drying is said to alter the structure irreversibly.

Although the dehydration of dicalcium aluminate hydrate was not systematically investigated in the present work, certain data were obtained that appear to necessitate a slight modification of the picture presented above. Drying of the precipitate from the moist condition to the octahydrate stage (over a saturated solution of NH_4Cl) resulted in only a very minor change in crystal-cell size. Thus the largest *d*-spacing (001) dropped from 10.9 or 10.8 A down to 10.6. The same effect has been noted by others [5]. There was evidence that this continues on further drying, down to d_{001}=10.4 A (approximately), but beyond that point an abrupt change was observed. A specimen dried to constant weight over $CaCl_2$, and having an approximate composition $2CaO \cdot Al_2O_3 \cdot 6H_2O$, gave an X-ray pattern indicating spacings distinctly different from those of the octahydrate. The largest spacing was 8.8 A. The only change in appearance under the microscope was a slight increase in refractive indices. Numerous preparations showed both hydrates coexisting in varying proportions.

An X-ray pattern of the lower hydrate is given in table 1, along with one of $2CaO \cdot Al_2O_3 \cdot 8H_2O$. The octahydrate pattern is included merely for comparison; the relative intensities given indicate a high degree of orientation of the mounted sample. No doubt this factor likewise affected the relative intensities in the second pattern, though to a smaller extent. Certain similarities between the two patterns are evident. On the basis of McMurdie's indexing, the pattern of $2CaO \cdot Al_2O_3 \cdot 8H_2O$ [5], together with the fact that the crystals do not lose their platy habit on dehydration to the $6H_2O$ stage, it appears likely that the lattice remains essentially unchanged except for shortening along the *c*-axis. This suggests that the water thus removed may have been present in loosely bound layers within the structure. The change from 8 to $6H_2O$ is completely reversible and occurs rather rapidly. Thus certain samples actually went from the higher to the lower hydrate while on the X-ray diffractometer, during a period of less than 1 hour.

The amount of water in the lower hydrate is known only approximately. The material used for the X-ray pattern (table 1) had the composition $2.10CaO \cdot Al_2O_3 \cdot 6.14H_2O$. Another preparation had the composition $1.95CaO \cdot Al_2O_3 \cdot 5.22H_2O$, but this was shown to contain a small percentage of the cubic $3CaO \cdot Al_2O_3 6 \cdot H_2O$ (which would also necessitate the presence of some form of Al_2O_3); the latter figure is therefore less reliable. The value, $6H_2O$, appears most probable from the data at hand.

TABLE 1. *X-ray diffraction lines of* $2CaO \cdot Al_2O_3 \cdot 8H_2O$ *and* $2CaO \cdot Al_2O_3 \cdot 6H_2O$

$2CaO \cdot Al_2O_3 \cdot 8H_2O$		$2CaO \cdot Al_2O_3 \cdot 6H_2O$	
Spacing	Relative intensity	Spacing	Relative intensity
A		*A*	
10.6	100	8.8	100
5.27	80	4.80	13
3.49	20	4.36	65
2.88	14	3.80	5
2.67	4	3.60	2
2.62	7	2.86	22
2.53	5	2.72	11
2.49	7	2.57	8
2.44	5	2.47	12
2.39	3	2.39	8
2.22	3	2.32	8
2.12	2	2.29	3
2.03	2	2.23	9
1.954	2	2.14	2
1.935	3	2.04	11
1.740	2	1.802	4
1.662	7	1.742	4
1.528	2	1.653	8
1.440	3	1.623	7
1.424	1	1.441	3
		1.352	4
		1.292	4
		1.289	3
		1.260	2

f. $4CaO \cdot Al_2O_3 \cdot 13H_2O$

Tetracalcium aluminate hydrate crystallizes in hexagonal plates, almost indistinguishable under the microscope from those of dicalcium aluminate hydrate. Like the latter compound its existence is well established, as a result of numerous investigations [1, 4, 5, 6, 9]. The comments given above concerning the symmetry of the dicalcium aluminate hydrate apply equally to the tetracalcium. Just as with the dicalcium compound the amount of water of crystallization is in some doubt. Most of the compositions reported in the literature range from 12 to $14H_2O$ [5]. The formula with $13H_2O$ has been generally adopted, but certain work of the

Building Research Station in England as reported by Lea [3] indicates that the fully hydrated compound may contain $19H_2O$. Some investigators, led by Assarsson [9], believe there are two forms, designated α and β, with the same degree of hydration but slightly different degrees of stability in the system; also perhaps a third form with one less molecule of water.

In the present study only one form of tetracalcium aluminate hydrate was produced, judging from the X-ray diffraction patterns. (Certain apparently contradictory evidence will be discussed below.) No special study was made of the amount of water of hydration. A slight shift in the X-ray diffraction lines with increased drying was noted.

g. $3CaO{\cdot}Al_2O_3{\cdot}CaCO_3{\cdot}11H_2O$

This compound obviously falls outside the system CaO-Al_2O_3-H_2O; nevertheless, it may appropriately be considered here. During the study of X-ray diffraction patterns of numerous preparations in the high-lime region of the system, a series of lines was frequently noted very close to those of $4CaO{\cdot}Al_2O_3{\cdot}13H_2O$. The maximum spacing averaged about 7.7 A, as compared with 8.2 for the tetracalcium compound. At first the new phase was tentatively considered to be the β-form of this compound, but when it later appeared in the low-lime region of the system as well, another explanation was sought. To ascertain whether it might be a carboaluminate such as that reported by Bessey [4], an attempt was made to prepare such a compound. From a mixture of calcium aluminate, calcium hydroxide, and ammonium carbonate solutions a precipitate was obtained, consisting of minute platy crystals having indices and birefringence somewhat higher than those of $4CaO{\cdot}Al_2O_3{\cdot}13H_2O$. The X-ray pattern agreed perfectly with the series of lines in question. Although the amount of material was insufficient for a precise analysis, the composition was reasonably close to the formula $3CaO{\cdot}Al_2O_3{\cdot}11H_2O$ suggested by Bessey. Further confirmation was deemed unnecessary, because just at that time a publication by Turriziani and Schippa [15] appeared describing the preparation of a carboaluminate of composition $3CaO{\cdot}Al_2O_3{\cdot}CaCO_3{\cdot}10.8H_2O$ and reporting an X-ray pattern in good agreement with those under consideration.

In only one of the preparations (No. 13, table 2) were the carboaluminate crystals of sufficient size to permit a determination of their indices of refraction, and even in this it was difficult because of the masking effect of the other phases. The high and low indices were 1.554 and 1.527, respectively.

The question as to the source of the CO_2 naturally arises. Although there was undoubtedly a little entry of atmospheric CO_2 when the bottles were opened for removal of samples, it seems likely that a more important factor was the passage of CO_2 through the walls of the polyethylene bottles. Polyethylene is known to be somewhat permeable to CO_2 [16], although the effect apparently was rather slow under the conditions of the present study. In most cases the amount was barely enough to be shown by the X-ray patterns. In a few it was much higher, possibly indicating that the bottle cap did not form a perfect seal.

h. Other Aluminates

Certain other hydrated calcium aluminates that have been reported by various investigators may also be mentioned. No evidence of a hexagonal tricalcium aluminate hydrate was found in this study. Compositions having approximately this ratio invariably gave X-ray patterns indicating mixtures of di- and tetracalcium aluminate hydrates. This negative evidence supports the view of Wells, Clarke, and McMurdie [5] that the alleged tricalcium compound does not occur.

Another tricalcium aluminate hydrate, in acicular form, and assigned the formula $3CaO{\cdot}Al_2O_3{\cdot}18$ to $21H_2O$, has been reported by several investigators [2]. It was not found in the present study. However, the author has previously prepared a compound of this general description and approximate composition. It was found only in aqueous extracts of an aluminous cement, and then only as a transitory phase. The solutions contained a trace of sulfide, which may or may not be significant.

The more basic aluminates that have been reported were not considered in this study, since they probably do not possess a field even of metastability in the system. There remains the compound $4CaO{\cdot}3Al_2O_3{\cdot}3H_2O$, which is formed under hydrothermal conditions but is unstable below 200° C. Although it has no place in the system at 1° C, a pair of experiments were conducted to study the course of its reactions.

2.3. Precipitation Experiments

A series of 10 supersaturated calcium aluminate solutions were prepared as described above, by diluting a master solution with various amounts of saturated lime water. They were then stored in the cold-cabinet. These are designated by numbers 1 to 10 in table 2. From time to time, samples of the solutions were taken for analysis, and small portions of the precipitates for examination. Data obtained at intermediate periods have been omitted from the table, except when needed to show the course of the reaction. The figures given for initial concentrations (columns 2 and 3) were calculated from the measured volumes of the analyzed master solutions. Concentrations at later periods (columns 5 and 6) were obtained by analysis, and the composition of the precipitate (column 7) was calculated from the difference. In the last column, the solid phase present in greatest amount is given first.

The change in concentration during precipitation may be visualized better by reference to figure 1, in which the concentration data for solutions 1 to 10, table 2, are plotted on rectangular coordinates. Initial concentrations are represented by the row of circles at the right. The lines extending downward to the left represent the changing concentrations.

TABLE 2. *Data showing changes in concentration and solid phases present during precipitation from calcium aluminate solutions at 1°C*

Experiment	Initial concentration		Reaction period	Concentration after reaction period		Molar ratio CaO:Al_2O_3, in precipitate (calculated)	Solid phases present [a]
	Al_2O_3	CaO		Al_2O_3	CaO		
	g/liter	*g/liter*		*g/liter*	*g/liter*		
			1 day	1.266	0.828		
1	1.278	0.833	11 days	0.144	.190	1.03	$CaO \cdot Al_2O_3 \cdot 10H_2O$; probably a little Al_2O_3 hyd.; trace of $2CaO \cdot Al_2O_3 \cdot 8H_2O$.
			13 mo	.112	.152	1.06	Same.
			1 day	.436	.393	1.24	
2	1.150	.879	11 days	.162	.316	1.04	$CaO \cdot Al_2O_3 \cdot 10H_2O$; trace of $2CaO \cdot Al_2O_3 \cdot 8H_2O$.
			75 days	.104	.300	1.01	Same, plus trace of $3CaO \cdot Al_2O_3 \cdot CaCO_3 \cdot 11H_2O$.
			1 day	.572	.412	2.07	
			7 days	.422	.402	1.58	
3	1.022	.925	11 days	.332	.330	1.57	$2CaO \cdot Al_2O_3 \cdot 8H_2O$; traces of $CaO \cdot Al_2O_3 \cdot 10H_2O$, $4CaO \cdot Al_2O_3 \cdot 13H_2O$, and $3CaO \cdot Al_2O_3 \cdot CaCO_3 \cdot 11H_2O$.
			13 mo	.112	.388	1.07	$2CaO \cdot Al_2O_3 \cdot 8H_2O$; $CaO \cdot Al_2O_3 \cdot 10H_2O$; $3CaO \cdot Al_2O_3 \cdot CaCO_3 \cdot 11H_2O$.
			1 day	.480	.499	2.06	
4	0.895	.970	11 days	.314	.329	2.01	$2CaO \cdot Al_2O_3 \cdot 8H_2O$; trace of $3CaO \cdot Al_2O_3 \cdot CaCO_3 \cdot 11H_2O$.
			1 mo	.316	.333	2.00	
			15 mo	.120	.394	1.35	$2CaO \cdot Al_2O_3 \cdot 8H_2O$; $CaO \cdot Al_2O_3 \cdot 10H_2O$; $3CaO \cdot Al_2O_3 \cdot CaCO_3 \cdot 11H_2O$.
			1 day	.230	.412	2.04	
5	.767	1.014	11 days	.174	.345	2.05	$2CaO \cdot Al_2O_3 \cdot 8H_2O$; trace of $3CaO \cdot Al_2O_3 \cdot CaCO_3 \cdot 11H_2O$.
			9 mo	.203	.366	2.09	Same.
			1 day	.168	.512	2.11	
6	.639	1.058	11 days	.110	.442	2.12	$2CaO \cdot Al_2O_3 \cdot 8H_2O$; $3CaO \cdot Al_2O_3 \cdot CaCO_3 \cdot 11H_2O$.
			9 mo	.085	.384	2.21	Same.
			1 day	.106	.543	2.54	
7	.511	1.108	11 days	.096	.556	2.42	$2CaO \cdot Al_2O_3 \cdot 8H_2O$; $4CaO \cdot Al_2O_3 \cdot 13H_2O$.
			11 mo	.078	.503	2.54	Same.
			1 day	.140	.670	3.62	
8	.383	1.154	11 days	.098	.570	3.73	$4CaO \cdot Al_2O_3 \cdot 13H_2O$; $2CaO \cdot Al_2O_3 \cdot 8H_2O$.
			11 mo	.072	.499	3.83	Same, plus $3CaO \cdot Al_2O_3 \cdot CaCO_3 \cdot 11H_2O$.
			1 day	.090	.870	3.52	
9	.256	1.191	11 days	.026	.726	3.67	$4CaO \cdot Al_2O_3 \cdot 13H_2O$; $2CaO \cdot Al_2O_3 \cdot 8H_2O$.
			11 mo	.016	.695	3.76	$4CaO \cdot Al_2O_3 \cdot 13H_2O$; $3CaO \cdot Al_2O_3 \cdot CaCO_3 \cdot 11H_2O$.
			1 day	.046	1.111	2.99	
10	.128	1.246	11 days	.004	1.018	3.34	$4CaO \cdot Al_2O_3 \cdot 13H_2O$.
			9 mo	.004	0.963	4.15	Same.
			3 hr	.570	.908	1.81	$2CaO \cdot Al_2O_3 \cdot 8H_2O$; $CaO \cdot Al_2O_3 \cdot 10H_2O$.
11	1.310	0.970	1 day	.208	.322	1.07	$CaO \cdot Al_2O_3 \cdot 10H_2O$.
			7 mo	.092	.260	1.06	Same.
			3 hr	.328	.366	2.16	$2CaO \cdot Al_2O_3 \cdot 8H_2O$; trace of $3CaO \cdot Al_2O_3 \cdot CaCO_3 \cdot 11H_2O$.
12	0.916	1.066	2 days	.312	.364	2.12	Same.
			5 mo	.240	.332	1.97	
			10 mo	.153	.372	1.65	$2CaO \cdot Al_2O_3 \cdot 8H_2O$; $CaO \cdot Al_2O_3 \cdot 10H_2O$.
			1 mo	.449	.317		
			2 mo	.364	.312	0.27	
13 [b]	.466	0.327	6 mo	.152	.229	.57	Gibbsite; $CaO \cdot Al_2O_3 \cdot 10H_2O$; $3CaO \cdot Al_2O_3 \cdot CaCO_3 \cdot 11H_2O$.
			13 mo	.100	.209	.54	Same.
			1 mo	.386	.269	1.32	Gibbsite.
14 [b]	.466	.327	3 mo	.320	.266	0.76	
			14 mo	.085	.200	.61	Gibbsite; $CaO \cdot Al_2O_3 \cdot 10H_2O$; $3CaO \cdot Al_2O_3 \cdot CaCO_3 \cdot 11H_2O$.
			1 mo	.104	.410	1.77	Gibbsite; few hexagonal plates.
15 [b]	.310	.610	11 mo	.103	.399	1.85	Gibbsite; $2CaO \cdot Al_2O_3 \cdot 8H_2O$; $3CaO \cdot Al_2O_3 \cdot CaCO_3 \cdot 11H_2O$.
			1 mo	.038	.691	3.12	Gibbsite; hexagonal plates.
16 [b]	.155	.893	11 mo	.022	.629	3.61	Gibbsite; $4CaO \cdot Al_2O_3 \cdot 13H_2O$; $3CaO \cdot Al_2O_3 \cdot CaCO_3 \cdot 11H_2O$.

[a] As used here, "trace" is equivalent to "barely sufficient to be detected on the X-ray diffraction pattern." [b] Gibbsite added to solution.

The calculated molar ratio of CaO to Al_2O_3 (C/A) in the precipitate in the early stages is indicated in each case.

Solution 1 was essentially unchanged after 1 day, but subsequently a very voluminous precipitate appeared. The X-ray diffraction pattern showed it to be chiefly $CaO \cdot Al_2O_3 \cdot 10H_2O$, with a detectable amount of $2CaO \cdot Al_2O_3 \cdot 8H_2O$. Under the electron microscope the predominant phase was observed to consist of slender prismatic crystals, less than 0.1 μ in thickness. A few much larger hexagonal crystals, presumably of $2CaO \cdot Al_2O_3 \cdot 8H_2O$, were noted. There were also a few masses of felted fibers, finer than the prismatic crystals. It could not be determined whether these were of the same composition or whether they were a different phase, possibly amorphous hydrated alumina. Precipitation was essentially complete after 11 days, and no change in appearance was observed after 13 months.

In the other members of the series, precipitation was more rapid, increasingly so as the CaO/Al_2O_3 ratio increased. No. 2 yielded a precipitate consisting largely of $CaO \cdot Al_2O_3 \cdot 10H_2O$, appearing as rosettes of prismatic crystals much coarser than those

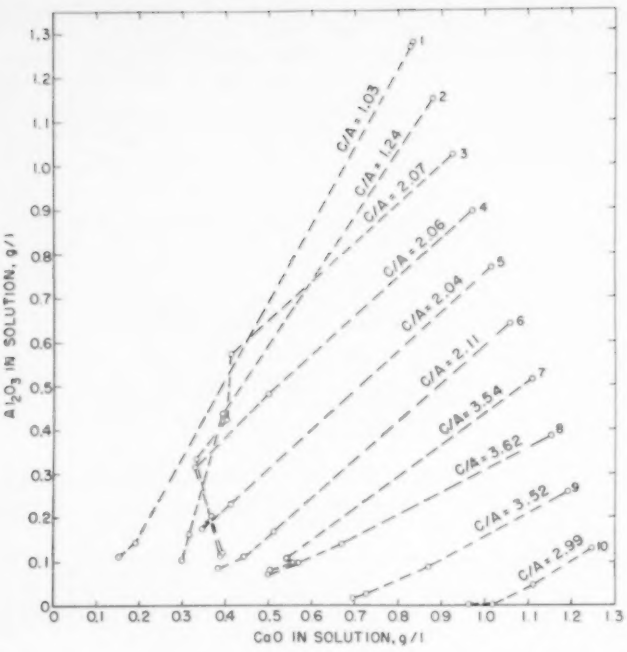

FIGURE 1. *Change in concentration of calcium aluminate solutions resulting from precipitation at 1° C.*

C/A=molar ratio, CaO/Al_2O_3. Numbers refer to experiments in table 1.

in No. 1. A detectable amount of the dicalcium compound was also present. After 75 days a steady state apparently had been reached, with no change except for the appearance of a detectable amount of the carboaluminate. At that time the precipitate was filtered off for use in further experiments.

The change in slope of the concentration curve for solution 2 suggested that the initial precipitate may have been richer in lime than was indicated by the analysis after 1 day. Another solution of comparable concentration therefore was prepared and examined at shorter intervals. This is designated No. 11 in table 2; it has been omitted from figure 1 to avoid confusion. The initial precipitate was observed to be $2CaO \cdot Al_2O_3 \cdot 8H_2O$, and the ratio of CaO to Al_2O_3 after 3 hr was nearer 2 than 1. However, after 1 day, only $CaO \cdot Al_2O_3 \cdot 10H_2O$ was observed. Thus the initially formed dicalcium compound must have redissolved, in agreement with the observed change in slope of the concentration curve.

Solutions 3, 4, 5, and 6 all precipitated $2CaO \cdot Al_2O_3 \cdot 8H_2O$ as the primary phase. The calculated CaO/Al_2O_3 is consistently slightly higher than 2. Any attempted explanation would be speculative, but it is clear that the inclusion of a small amount of tetracalcium aluminate or carboaluminate would tend to raise the ratio. The precipitate in No. 3 underwent partial conversion to $CaO \cdot Al_2O_3 \cdot 10H_2O$ within 7 days, as indicated by the change in CaO/Al_2O_3 ratio, later confirmed by X-ray diffraction. The same reaction occurred in No. 4, but in this case it did not start until after 1 month.

Experiment 12, table 2 (omitted from fig. 1) was intermediate between Nos. 4 and 5 in initial CaO/Al_2O_3 ratio. It behaved like No. 4, except that the appearance of the monocalcium aluminate was still longer delayed. Nos. 5 and 6 showed none of the latter compound even after 9 months.

Solutions 7, 8, and 9 precipitated mixtures of $2CaO \cdot Al_2O_3 \cdot 8H_2O$ and $4CaO \cdot Al_2O_3 \cdot 13H_2O$, with very little change after 11 days except for the appearance of small amounts of carboaluminate. The molar CaO/Al_2O_3 ratio in the precipitate was between 2 and 4. The initial ratio in the precipitate from solution 10 was calculated to be 2.99. This is suspected of being in error, as the low-alumina concentration in this region greatly magnifies the effect of small analytical errors. The X-ray patterns of the precipitate showed only $4CaO \cdot Al_2O_3 \cdot 13H_2O$.

To recapitulate: No. 1 precipitated only $CaO \cdot Al_2O_3 \cdot 10H_2O$; Nos. 11, 2, 3, 4, and 12 gave $2CaO \cdot Al_2O_3 \cdot 8H_2O$ first, which was replaced by $CaO \cdot Al_2O_3 \cdot 10H_2O$, more slowly and less completely as the proportion of CaO in solution increased; Nos. 5 and 6 gave only $2CaO \cdot Al_2O_3 \cdot 8H_2O$; Nos. 7, 8, and 9 yielded mixtures of the dicalcium and tetracalcium aluminate hydrates; and No. 10 precipitated only the tetracalcium compound.

Reaction mixtures 13 to 16 constitute a series in which the initial concentration of both Al_2O_3 and CaO was much lower than in the foregoing group. One gram of solid gibbsite was added in each case, in an attempt to induce precipitation of this stable phase instead of the metastable aluminates. As indicated by the results in table 2, this attempt was unsuccessful. Aside from supplying additional data, this group is of interest chiefly in that the crystalline phases formed very slowly, yielding crystals of adequate size for optical study.

2.4. Solution Experiments

It is evident from the foregoing that the approach to equilibrium from supersaturation at 1° C is a very slow process. Attempts were therefore made to approach it from the opposite direction, that is, by determining the solubilities of the various solid phases in different concentrations of calcium hydroxide. In each experiment the solid phase was added in moderate excess to pure water or to lime water of known concentration. The procedures for storage, analysis, and examination were the same as for the precipitation experiments.

a. Hydrates Formed by Precipitation

It will be convenient to consider first, as a group, the three ternary compounds found in the precipitation experiments; namely, $CaO \cdot Al_2O_3 \cdot 10H_2O$, $2CaO \cdot Al_2O_3 \cdot 8H_2O$, and $4CaO \cdot Al_2O_3 \cdot 13H_2O$. Data for this group are given in table 3, concerning which a few explanatory notes are in order. Final concentrations were determined by analysis, whereas initial concentrations were calculated. In certain cases the solids were introduced in the form of a suspension in the solution in which they were prepared. This accounts for the fact that not all the experiments started from zero Al_2O_3 concentration.

TABLE 3. *Solubilities of* $CaO \cdot Al_2O_3 \cdot 10H_2O$, $2CaO \cdot Al_2O_3 \cdot 8H_2O$, *and* $4CaO \cdot Al_2O_3 \cdot 13H_2O$ *in calcium hydroxide solutions*

Experiment	Solid phases initially present	Initial concentration		Duration of contact	Final concentration		Solid phases present at end of experiment
		Al_2O_3	CaO		Al_2O_3	CaO	
		g/liter	*g/liter*	*Months*	*g/liter*	*g/liter*	
1	$CaO \cdot Al_2O_3 \cdot 10H_2O$	0.000	0.000	12	0.070	0.169	$CaO \cdot Al_2O_3 \cdot 10H_2O$; calcite, gibbsite.
2	$CaO \cdot Al_2O_3 \cdot 10H_2O$	.056	.211	2	.119	.222	$CaO \cdot Al_2O_3 \cdot 10H_2O$; carboaluminate.
3	$CaO \cdot Al_2O_3 \cdot 10H_2O$	.056	.283	2	.118	.290	$CaO \cdot Al_2O_3 \cdot 10H_2O$; very little carboaluminate.
4	$CaO \cdot Al_2O_3 \cdot 10H_2O + 2CaO \cdot Al_2O_3 \cdot 8H_2O$	.000	.000	5	.130	.308	$CaO \cdot Al_2O_3 \cdot 10H_2O$; $2CaO \cdot Al_2O_3 \cdot 8H_2O$.
5	$2Ca \cdot Al_2O_3 \cdot 8H_2O$	.000	.000	5	.161	.339	$2CaO \cdot Al_2O_3 \cdot 8H_2O$; carboaluminate.
6	$2Ca \cdot Al_2O_3 \cdot 8H_2O$	.000	.12	6	.182	.324	$2CaO \cdot Al_2O_3 \cdot 8H_2O$; carboaluminate.
7	$2CaO \cdot Al_2O_3 \cdot 8H_2O$ [a]	.001	.35	4	.081	.419	$2CaO \cdot Al_2O_3 \cdot 8H_2O$; $CaO \cdot Al_2O_3 \cdot 10H_2O$.
8	$2CaO \cdot Al_2O_3 \cdot 8H_2O$ [a]	.001	.52	4	.049	.537	$2CaO \cdot Al_2O_3 \cdot 8H_2O$.
9	$2CaO \cdot Al_2O_3 \cdot 8H_2O$ [a]	.001	.69	4	.024	.630	$2CaO \cdot Al_2O_3 \cdot 8H_2O$; $4CaO \cdot Al_2O_3 \cdot 13H_2O$.
10	$2CaO \cdot Al_2O_3 \cdot 8H_2O + 4CaO \cdot Al_2O_3 \cdot 13H_2O$	.005	.514	4	.040	.550	$2CaO \cdot Al_2O_3 \cdot 8H_2O$; $4CaO \cdot Al_2O_3 \cdot 13H_2O$.
11	$2CaO \cdot Al_2O_3 \cdot 8H_2O + 4CaO \cdot Al_2O_3 \cdot 13H_2O$	.005	.743	4	.014	.693	$2CaO \cdot Al_2O_3 \cdot 8H_2O$; $4CaO \cdot Al_2O_3 \cdot 13H_2O$.
12	$2CaO \cdot Al_2O_3 \cdot 8H_2O + 4CaO \cdot Al_2O_3 \cdot 13H_2O$	.005	.922	3	.008	.889	$2CaO \cdot Al_2O_3 \cdot 8H_2O$; $4CaO \cdot Al_2O_3 \cdot 13H_2O$.
13	$2CaO \cdot Al_2O_3 \cdot 8H_2O + 4CaO \cdot Al_2O_3 \cdot 13H_2O$	.003	1.143	4	.001	1.098	$2CaO \cdot Al_2O_3 \cdot 8H_2O$; $4CaO \cdot Al_2O_3 \cdot 13H_2O$.
14	$4CaO \cdot Al_2O_3 \cdot 13H_2O$ [b]	.000	0.000	1	.020	0.314	$4CaO \cdot Al_2O_3 \cdot 13H_2O$.
15	$4CaO \cdot Al_2O_3 \cdot 13H_2O$ [b]	.000	.000	1	.028	.396	$4CaO \cdot Al_2O_3 \cdot 13H_2O$.
16	$4CaO \cdot Al_2O_3 \cdot 13H_2O$ [b]	.000	.000	1	.026	.442	$4CaO \cdot Al_2O_3 \cdot 13H_2O$.
17	$4CaO \cdot Al_2O_3 \cdot 13H_2O$ [b]	.000	.000	1	.024	.489	$4CaO \cdot Al_2O_3 \cdot 13H_2O$.
18	$4CaO \cdot Al_2O_3 \cdot 13H_2O$ [b]	.000	.000	1	.026	.565	$4CaO \cdot Al_2O_3 \cdot 13H_2O$.
19	$4CaO \cdot Al_2O_3 \cdot 13H_2O$ [b]	.000	.000	1	.022	.610	$4CaO \cdot Al_2O_3 \cdot 13H_2O$.
				Weeks			
20	$4CaO \cdot Al_2O_3 \cdot 13H_2O$ [b]	.000	.40	6	.009	.758	$4CaO \cdot Al_2O_3 \cdot 13H_2O$.
21	$4CaO \cdot Al_2O_3 \cdot 13H_2O$ [b]	.000	.65	6	.008	.868	$4CaO \cdot Al_2O_3 \cdot 13H_2O$.
22	$4CaO \cdot Al_2O_3 \cdot 13H_2O$ [b]	.000	.80	6	.001	.971	$4CaO \cdot Al_2O_3 \cdot 13H_2O$.
23	$4CaO \cdot Al_2O_3 \cdot 13H_2O$ [b]	.000	1.00	6	.002	1.103	$4CaO \cdot Al_2O_3 \cdot 13H_2O$.

[a] Contained a minor amount of $CaO \cdot Al_2O_3 \cdot 10H_2O$.
[b] Contained $Ca(OH)_2$. In experiments 14 to 19, concentration of $Ca(OH)_2$ in solution was varied by using increasing amounts of the solid preparation.

Great difficulty was experienced in obtaining single-phase preparations for starting materials. Thus the dicalcium aluminate hydrate used in experiments 7 to 9 contained some monocalcium aluminate hydrate. This phase persisted in No. 7 but dissolved in the two more basic solutions. Tetracalcium aluminate hydrate usually was obtained as a mixture with the dicalcium compound. (Such a mixture was used in experiments 10 to 13.) In order to avoid the less basic aluminate it was found necessary to have free calcium hydroxide present. The latter contaminant dissolved completely during the solution experiments, and in experiments 14 to 19 the equilibrium concentration of $Ca(OH)_2$ was varied merely by varying the amount of solid originally used.

In this group of experiments a steady state was attained in a week or two, no doubt because of the extreme fineness of the crystals. The final concentrations given in table 3 are represented in figure 2 by filled circles, and the tentative solubility curves

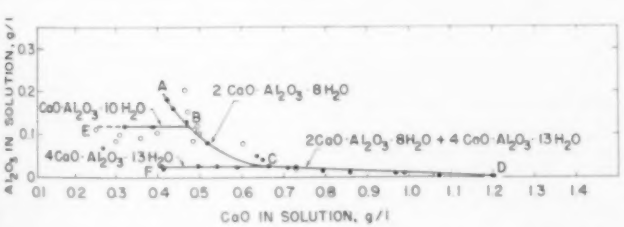

FIGURE 2. *Solubilities of* $CaO \cdot Al_2O_3 \cdot 10H_2O$, $2CaO \cdot Al_2O_3 \cdot 8H_2O$, *and* $4CaO \cdot Al_2O_3 \cdot 13H_2O$ *in calcium hydroxide solutions at 1° C.*

Curves are based on data from table 3 (filled circles). Data from table 2 (open circles) are included for comparison.

are drawn with reference to these points. The open circles represent the final data from the precipitation experiments (table 2), and are included here to facilitate comparison of the two sets of data.

Curve ABC, figure 2, represents approximately the solubility values for $2CaO \cdot Al_2O_3 \cdot 8H_2O$. The corresponding concentration values from table 2 lie somewhat above the curve, but not far from it. Curve CD fits equally well the data for solubility of $4CaO \cdot Al_2O_3 \cdot 13H_2O$ or for a mixture of the tetra- and dicalcium compounds, including the values from both table 2 and table 3. The horizontal line FC fits the data for $4CaO \cdot Al_2O_3 \cdot 13H_2O$ in the region below 0.6 g of CaO per liter. (There is, of course, no counterpart of this in table 2.) Line EB represents roughly the solubility of $CaO \cdot Al_2O_3 \cdot 10H_2O$. Here the values from table 2 (open circles) all fall below the curve, as does the value for experiment 1 in table 3.

There should be an invariant point (metastable) at the intersection (B) of the curves for the mono- and dicalcium aluminate hydrates. The precipitates obtained in experiments 4 and 7 in table 3, and 3 and 4 in table 2, ended essentially as mixtures of $CaO \cdot Al_2O_3 \cdot 10H_2O$ and $2CaO \cdot Al_2O_3 \cdot 8H_2O$. Three of these had compositions very close to B, probably within the limits of accuracy of the procedures, but the fourth was appreciably removed. This may reasonably be attributed to lack of attainment of equilibrium.

Point C does not represent an invariant point. The compound $4CaO \cdot Al_2O_3 \cdot 13H_2O$ appears to be in equilibrium all along the line FCD. The fact that $2CaO \cdot Al_2O_3 \cdot 8H_2O$ coexists, seemingly indefinitely, with $4CaO \cdot Al_2O_3 \cdot 13H_2O$ between C and D (and in

fact, beyond D to the limit of $Ca(OH)_2$ solubility), points to extreme slowness of attainment of equilibrium in the area. If this view is correct, there should be two solubility curves between C and D, one for each hydrate, but they must be practically coincident.

b. $3CaO \cdot Al_2O_3 \cdot 6H_2O$

From earlier investigations [5, 6, 7] it is known that the isometric $3CaO \cdot Al_2O_3 \cdot 6H_2O$ exists as a stable phase in the system $CaO\text{-}Al_2O_3\text{-}H_2O$ from 20° to about 200° C. The experiments summarized in table 4 comprise a series in which the solubility of this compound in water and in calcium hydroxide at 1° C was sought. The results were highly erratic. The most interesting fact, however, is that the original solid phase was largely replaced by $2CaO \cdot Al_2O_3 \cdot 8H_2O$ in experiments 3 and 4 and partially by $4CaO \cdot Al_2O_3 \cdot 13H_2O$ in Nos. 7, 9, and 11. Inasmuch as these hexagonal phases were known to be absent from the original solid, it must be concluded that $3CaO \cdot Al_2O_3 \cdot 6H_2O$ is not stable in these areas. The final concentrations here fall close to the solubility curves for the respective hexagonal phases.

The final concentration data in table 4 are plotted in figure 3, superimposed upon the solubility curves of the hexagonal aluminates, borrowed from figure 2. It is evident that the plotted points, taken as a single group, cannot be connected by any reasonable curve. The experiments may, however, be separated into two groups: (a) those in which the residue was partially transformed to di- and tetracalcium aluminate hydrates, and (b) those in which the $3CaO \cdot Al_2O_3 \cdot 6H_2O$ remained unchanged (except for minor formation of carboaluminate). Group (a) is represented in figure 3 by filled circles, which fall not far from curve ABCD, the solubility curve of the di- and tetracalcium aluminates. Group (b) is represented by open circles, which appear to be scattered at random appreciably below curve ABCD.

It is concluded that $3CaO \cdot Al_2O_3 \cdot 6H_2O$ is less stable than $2CaO \cdot Al_2O_3 \cdot 8H_2O$ and $4CaO \cdot Al_2O_3 \cdot 13H_2O$ at 1° C, but that it goes into solution extremely slowly. For some unexplained reason, certain experiments in group (b) failed to reach equilibrium concentrations even after as long as 16 months of storage. Others

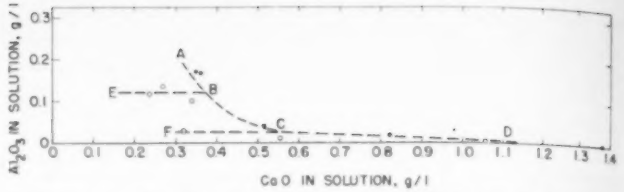

FIGURE 3. *Solubility of* $3CaO \cdot Al_2O_3 \cdot 6H_2O$ *in calcium hydroxide solutions at 1° C.*

Open circles represent mixtures in which the solid phase was essentially unchanged; closed circles those in which phase transformations had occurred. Solubility curves, taken from figure 2, are included as a frame of reference.

in group (a) reached concentrations relatively quickly (within 1 month for experiments 3 and 4), at which time they were supersaturated with respect to the hexagonal phases, whereupon the latter precipitated out. Even here the reaction had not gone to completion after prolonged storage. It is conceivable that the small amount of carboaluminate appearing during the long storage period may have formed a protective film on the crystals.

c. $4CaO \cdot 3Al_2O_3 \cdot 3H_2O$

Although the 4:3:3 ternary compound is stable only above approximately 200° C [7], it was considered of interest to study its behavior at 1° C. In water the compound dissolved slowly, without formation of a precipitate, and after 10 months had reached the surprisingly high concentration of 0.382 g of Al_2O_3 and 0.285 g of CaO per liter. By reference to figure 2 it appears that such a solution must be highly supersaturated with respect to $CaO \cdot Al_2O_3 \cdot 10H_2O$.

The solubility in calcium hydroxide was studied at only one concentration, 0.58 g of CaO per liter. The reaction proceeded slowly, and involved simultaneous dissolution of the 4:3:3 compound and precipitation of $2CaO \cdot Al_2O_3 \cdot 8H_2O$. The final concentration was 0.092 g of Al_2O_3 and 0.435 g of CaO per liter, which is close to curve BC, figure 2.

d. Gibbsite ($Al_2O_3 \cdot 3H_2O$)

An attempt was made to determine the solubility of gibbsite in a series of lime solutions ranging from 0.2 g of CaO per liter up to saturation, but the results were unsatisfactory. After 4 months at 1° C, the Al_2O_3 in solution was barely detectable. In an effort to speed up the process, the mixtures were allowed to

TABLE 4. *Solubility of* $3CaO \cdot Al_2O_3 \cdot 6H_2O$ *in calcium hydroxide solutions*

Experiment	Initial concentration, CaO	Duration of contact	Final concentration		Solid phases present at end of experiment
			Al_2O_3	CaO	
	g/liter	*Months*	*g/liter*	*g/liter*	
1	0.000	16	0.117	0.235	$3CaO \cdot Al_2O_3 \cdot 6H_2O$; $3CaO \cdot Al_2O_3 \cdot CaCO_3 \cdot 11H_2O$.
2	.000	15	.134	.268	Do.
3	.000	9	.166	.360	$2CaO \cdot Al_2O_3 \cdot 8H_2O$; $3CaO \cdot Al_2O_3 \cdot 6H_2O$; $3CaO \cdot Al_2O_3 \cdot CaCO_3 \cdot 11H_2O$.
4	.000	9	.169	.349	Do.
5	.128	15	.100	.338	$3CaO \cdot Al_2O_3 \cdot 6H_2O$; $3CaO \cdot Al_2O_3 \cdot CaCO_3 \cdot 11H_2O$.
6	.257	16	.028	.319	$3CaO \cdot Al_2O_3 \cdot 6H_2O$; $3CaO \cdot Al_2O_3 \cdot CaCO_3 \cdot 11H_2O$.
7	.434	15	.040	.515	$3CaO \cdot Al_2O_3 \cdot 6H_2O$; $4CaO \cdot Al_2O_3 \cdot 13H_2O$; very little $3CaO \cdot Al_2O_3 \cdot CaCO_3 \cdot 11H_2O$.
8	.535	14	.010	.554	$3CaO \cdot Al_2O_3 \cdot 6H_2O$; $3CaO \cdot Al_2O_3 \cdot CaCO_3 \cdot 11H_2O$.
9	.778	14	.018	.822	$3CaO \cdot Al_2O_3 \cdot 6H_2O$; $3CaO \cdot Al_2O_3 \cdot 11H_2O$; $4CaO \cdot Al_2O_3 \cdot 13H_2O$.
10	1.039	14	.003	1.055	$3CaO \cdot Al_2O_3 \cdot 6H_2O$; $3CaO \cdot Al_2O_3 \cdot CaCO_3 \cdot 11H_2O$.
11	[a] 1.476	10	.001	1.371	$Ca(OH)_2$; $3CaO \cdot Al_2O_3 \cdot 6H_2O$; very little $4CaO \cdot Al_2O_3 \cdot 13H_2O$.

[a] Contained excess $Ca(OH)_2$ in suspension.

stand 6 months at room temperature, after which they were again stored at 1° for 10 months. In the first solution (0.2 g of CaO per liter), the Al_2O_3 concentration rose from 0.002 to 0.012 g per liter during the storage at room temperature, and failed to change on subsequent storage at 1° C. This figure approximates the solubility in lime solution of the same concentration at 21° C [5] and the true value at 1° would be expected to be lower.

In all the more basic solutions (0.4 g of CaO per liter and higher) there was precipitation of $4CaO \cdot Al_2O_3 \cdot 13H_2O$, indicating that the gibbsite had dissolved sufficiently to exceed the solubility of this aluminate. Final concentrations fell close to curve FCD, figure 2.

Because of the long time involved, further work on the solubility of gibbsite in lime solutions at 1° C was abandoned. The only conclusions to be drawn from the present data are: (1) That gibbsite appears stable in lime solutions up to 0.2 g of CaO per liter; (2) that the equilibrium concentration of Al_2O_3 at this point is between 0.002 and 0.012 g per liter; and (3) that at some higher lime concentration, the solubility curve of gibbsite intersects that of $4CaO \cdot Al_2O_3 \cdot 13H_2O$.

2.5. Phase Equilibrium Diagram

From the foregoing data it is possible to construct at least a partial diagram of stable and metastable phase equilibria in the system CaO-Al_2O_3-H_2O at 1° C. Such a diagram is presented in figure 4. Certain assumptions and qualifications are necessary.

One assumption is that the carbon dioxide in solution and the carboaluminate precipitated were without effect. While this cannot be strictly true, it is evidently not far from correct. Carbon dioxide in very small concentration is known to react with lime solutions, forming calcite. In the present work the carboaluminate formed in preference to calcite in nearly every case, hence the CO_2 remaining in solution must have been even less. Also, the precipitated carboaluminate probably is the least soluble of the phases present (possibly excepting gibbsite), and it would therefore not alter the equilibrium concentration.

The position of the solubility curve of gibbsite, GF, is merely an estimate. The position of D, the solubility of calcium hydroxide, is based on values in the literature [11]. Curve CD, of course, cannot meet the horizontal axis at D; rather there must be an invariant point nearby, with an Al_2O_3 concentration about 0.001 g per liter. Two curves are assumed to exist between this invariant point and C; the lower one the stable curve for $4CaO \cdot Al_2O_3 \cdot 13H_2O$, the upper a metastable curve for $2CaO \cdot Al_2O_3 \cdot 8H_2O$.

Curve ABC is essentially a compromise between data obtained respectively from precipitation and from solution experiments. The upper end (near A) takes into account the inflection points of certain lines (3 and 4) in figure 1. Curve EB is somewhat uncertain as to position, as there is considerable scatter among the points on which it is based.

With these qualifications and assumptions in mind, the diagram may now be summarized. The stable phases are gibbsite, tetracalcium aluminate hydrate, and calcium hydroxide. The position of point F, the invariant between gibbsite and $4CaO \cdot Al_2O_3 \cdot 13H_2O$, is not known. The invariant between $4CaO \cdot Al_2O_3 \cdot 13H_2O$ and $Ca(OH)_2$, at D, is estimated to be at 0.001 g of Al_2O_3 and 1.30 g of CaO per liter, and the solubility of $Ca(OH)_2$ (from the literature [11]) is likewise placed at 1.30 g of CaO per liter. The compound $2CaO \cdot Al_2O_3 \cdot 8H_2O$ is in metastable equilibrium with solution along curve ABCD, the section CD being practically coincident with the curve for $4CaO \cdot Al_2O_3 \cdot 13H_2O$. Nothing is known as to its extent above A. Curve EB represents the equilibrium of $CaO \cdot Al_2O_3 \cdot 10H_2O$ and solution; its leftward extent is unknown. The point B is a metastable invariant between $2CaO \cdot Al_2O_3 \cdot 8H_2O$, $CaO \cdot Al_2O_3 \cdot 10H_2O$, and solution.

Metastable solutions to the right of AB tend to precipitate $2CaO \cdot Al_2O_3 \cdot 8H_2O$ until the concentration reaches AB, whereupon $CaO \cdot Al_2O_3 \cdot 10H_2O$ is formed, and the concentration shifts toward B (see table 2, experiments 3, 4, 11). Solutions richer in lime (for example, No. 7 in table 2) precipitate both di- and tetracalcium aluminate hydrates until the concentration reaches BC. At this point, presumably, $4CaO \cdot Al_2O_3 \cdot 13H_2O$ continues to precipitate out, but as long as there is any $2CaO \cdot Al_2O_3 \cdot 8H_2O$ left, the latter will continue to control the concentration of the solution, which thus will still lie on BC. In time the dicalcium compound should be used up, and the concentration fall to curve FC, but this stage was not reached in any of the precipitation experiments described above.

The area under GFCD represents stable solutions. Solutions above GF are supersaturated with respect to gibbsite, but the rate of precipitation is extremely slow. Solutions in the general area ABE can precipitate $CaO \cdot Al_2O_3 \cdot 10H_2O$.

3. Discussion

3.1. Relation to Earlier Data

After reviewing the literature on the system CaO-Al_2O_3-H_2O, one is impressed by the wide variance, not so much in the actual data as in the interpretation of the data. Some of the results obtained in the present study may help to explain some of the contradictory conclusions.

Several investigators of the calcium aluminates have stressed the necessity for rigid exclusion of carbon dioxide; yet it is probable that complete absence of CO_2 has seldom, if ever, been attained. Even freshly boiled distilled water retains some CO_2, and the rubber stoppers commonly used for closures of the reaction flasks are by no means impermeable to atmospheric CO_2. Formation of calcite has, in fact, been reported in some cases [10]. This phase, if present, is conspicuous under the microscope by reason of its high birefringence and distinctive crystal shape. It is only natural that the absence of calcite might lead the investigator to assume the absence of CO_2 from his reaction vessel. On the

469110—58—2

other hand, if any of the carboaluminate, $3CaO \cdot Al_2O_3 \cdot CaCO_3 \cdot 11H_2O$, were present, it might readily be mistaken for $4CaO \cdot Al_2O_3 \cdot 13H_2O$. This might help to explain the discrepancies in reported refractive indices (as has been suggested by Bessey [4]), as well as the presumed multiplicity of forms of tetracalcium aluminate hydrate. By reference to tables 2 and 3 it may be noted that the carboaluminate was present in mixtures including almost the entire range of lime concentration. It may be significant that D'Ans and Eick [6] showed a similar range for the solubility of their β-tetracalcium aluminate hydrate, whereas the α-form was confined to the more basic region approximating that indicated by Wells, Clarke, and McMurdie [5] for the tetracalcium compound.

Another possible source of confusion is the apparent instability of $2CaO \cdot Al_2O_3 \cdot 8H_2O$ on drying. As was brought out above, this compound by itself underwent a dehydration to $2CaO \cdot Al_2O_3 \cdot 6H_2O$, on drying over $CaCl_2$, and the product gave an X-ray diffraction pattern that might conceivably have been mistaken for that of $4CaO \cdot Al_2O_3 \cdot 13H_2O$. This reaction was reversible. A different phenomenon was observed with precipitates consisting of mixtures of di- and tetracalcium aluminate hydrates. After drying over $CaCl_2$, such precipitates often gave patterns showing the lines of $4CaO \cdot Al_2O_3 \cdot 13H_2O$ only. Presumably the dicalcium compound had undergone decomposition to the tetracalcium compound and alumina.[2] This effect was not reversible. For precipitates of this type it was found necessary to obtain the X-ray pattern while the material was moist. Obviously this change on drying could lead to a false conclusion as to the solid phases prese in contact with the solution.

3.2. Relation to the System at 21° C

If the equilibrium diagram (fig. 4) is studied in comparison with the diagram published by Wells, Clarke, and McMurdie [5] for the same system at 21° C, certain marked differences are noted, as well as some similarities. Curve ABCD in figure 4 has its counterpart in the 21° C diagram, and the same area of contusion between di- and tetracalcium aluminates exists in the approximate range CD. However, the 21° C diagram does not show a stable solubility curve for $4CaO \cdot Al_2O_3 \cdot 13H_2O$ comparable to FC. It should be noted in this connection that D'Ans and Eick [6] show a metastable solubility curve for the β form of this hydrate in the general area of FC. The absence from the 1° diagram of a stability field for the isometric $3CaO \cdot Al_2O_3 \cdot 6H_2O$ is also a difference of major importance. The existence of a metastable solubility curve for monocalcium aluminate hydrate at 1°, of course, was not unexpected. The other differences between the diagrams for 1° and 21° are more

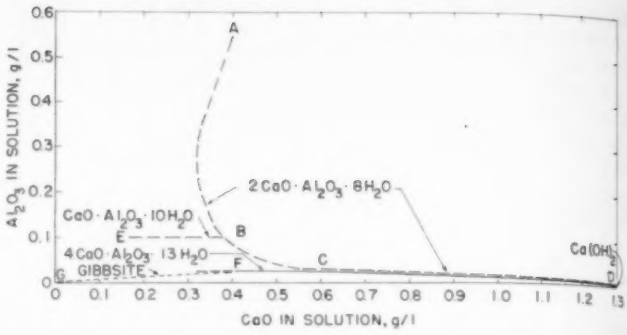

FIGURE 4. *Portion of the system* $CaO-Al_2O_3-H_2O$ *at 1° C.*

ABCD, metastable equilibrium curve for $2CaO \cdot Al_2O_3 \cdot 8H_2O$; EB, metastable solubility curve for $CaO \cdot Al_2O_3 \cdot 10H_2O$; GF, (assumed) stable equilibrium curve for gibbsite; FCD, stable equilibrium curve for $4CaO \cdot Al_2O_3 \cdot 13H_2O$.

surprising, and it appears that further studies at one or more intermediate temperatures may be needed to define all the stability and metastability areas.

3.3. Application to Cement Hydration

The system $CaO-Al_2O_3-H_2O$ is not directly applicable to portland cement, which is predominantly a calcium silicate cement, with enough calcium sulfate added to combine with most of the alumina in the early stages. On the other hand, it has been shown [10] that the hydration of aluminous cements, at least to a first approximation, can be explained in terms of reactions in the system $CaO-Al_2O_3-H_2O$. Aluminous cements are known to react with water to form highly supersaturated calcium aluminate solutions slightly more basic than monocalcium aluminate. The crystalline phase that precipitates first may be $CaO \cdot Al_2O_3 \cdot 10H_2O$ or $2CaO \cdot Al_2O_3 \cdot 8H_2O$, or a mixture of these, depending on temperature, basicity, and probably other factors. From the data in table 2 it may be concluded that, at 1° C, $CaO \cdot Al_2O_3 \cdot 10H_2O$ either would precipitate first or would form rapidly after an initial precipitation of the dicalcium compound. Earlier work [10] indicates that, at room temperature, $2CaO \cdot Al_2O_3 \cdot 8H_2O$ forms initially and persists for long periods. However, it is clear from other data in the same report that the reactions of cement in paste form are not necessarily identical with those in the presence of a large excess of water. Thus $CaO \cdot Al_2O_3 \cdot 10H_2O$, rather than $2CaO \cdot Al_2O_3 \cdot 8H_2O$, was shown by X-ray diffraction to be the predominant phase in pastes of aluminous cements after hydration at room temperature (24° C). From the data in the present report, coupled with that given in an earlier paper [13], it is concluded that monocalcium aluminate hydrate is also the chief crystalline product of hydration of aluminous cements at 1° C.

In connection with the hydration of cements, the carboaluminate, $3CaO \cdot Al_2O_3 \cdot CaCO_3 \cdot 11H_2O$, should also be mentioned. From tables 2 and 3 it is apparent that this phase was encountered throughout the range of lime concentrations studied, despite efforts to exclude CO_2. Most other investigators likewise

[2] While this paper was in process of publication, two other papers bearing in part on this phenomenon appeared in the literature. The authors, Roberts[18] and Schippa and Turriziani [19], report similar observations, but offer a different explanation. According to their views, the X-ray lines here attributed to dicalcium aluminate hydrate may actually represent a different form of tetracalcium aluminate hydrate (with 19 H_2O, according to Roberts).

have sought to eliminate the extra component. In practice, however, cement is always mixed and placed in the presence of atmospheric CO_2, hence the carboaluminate may form freely. Evidence of it has been found in the X-ray patterns of hardened pastes of aluminous cements. In one of the studies previously referred to [10] it was reported as "phase x"; the position of the diffraction lines now permits its identification as the carboaluminate.

Some of the recent investigations of Farran [17] into the nature of the contact film between hardened cement and aggregate are also of interest in this connection. Farran found that aluminous cement appeared to react superficially with calcite aggregate. The X-ray pattern of the reaction product included a series of lines that agree well with the pattern obtained in the present study for the carboaluminate. Farran was of the opinion that the pattern indicated the presence of a solid solution between $4CaO{\cdot}Al_2O_3{\cdot}13H_2O$ and a carboaluminate. Such a composition previously had been suggested by Bessey [4] for the mineral hydrocalumite. In the present work, however, and solely on the basis of the X-ray patterns, the carboaluminate and $4CaO{\cdot}Al_2O_3{\cdot}13H_2O$ appear to exist side by side, with no evidence of solid solution between the two.

These questions cannot be resolved without further data. There can be little doubt, however, that carbon dioxide may play a significant role during, and subsequent to, the hardening of aluminous cements, and probably of other hydraulic cements as well.

4. Summary

A study of the system CaO-Al_2O_3-H_2O at 1° C has been made. The stable phases appear to be gibbsite ($Al_2O_3{\cdot}3H_2O$), $4CaO{\cdot}Al_2O_3{\cdot}13H_2O$, and $Ca(OH)_2$. Metastable equilibrium curves were determined for $2CaO{\cdot}Al_2O_3{\cdot}8H_2O$ and $CaO{\cdot}Al_2O_3{\cdot}10H_2O$. A metastable invariant point for the latter two hydrates and solution exists at about 0.10 g of Al_2O_3 and 0.38 g of CaO per liter. The compounds $2CaO{\cdot}Al_2O_3{\cdot}8H_2O$ and $4CaO{\cdot}Al_2O_3{\cdot}13H_2O$ crystallize together over a wide range of concentration, but the former is presumed to be metastable throughout the range. The isometric $3CaO{\cdot}Al_2O_3{\cdot}6H_2O$ appears to be metastable at 1° C, being transformed very slowly to one or more of the hexagonal hydrates.

No evidence was found of the existence of a hexagonal tricalcium aluminate hydrate. Only one form of the tetracalcium aluminate hydrate was observed. A similar phase, which was observed in minor amounts in most of the solid residues in contact with solutions, especially after prolonged storage, was identified as a carboaluminate, probably $3CaO{\cdot}Al_2O_3{\cdot}CaCO_3{\cdot}11H_2O$. The hydrate $2CaO{\cdot}Al_2O_3{\cdot}8H_2O$, on being dried over $CaCl_2$, was found to lose 2 molecules of water reversibly. The lower hydrate has a characteristic X-ray pattern. Coprecipitated mixtures of $2CaO{\cdot}Al_2O_3{\cdot}8H_2O$ and $4CaO{\cdot}Al_2O_3{\cdot}13H_2O$, after drying over $CaCl_2$, showed lines only of $4CaO{\cdot}Al_2O_3{\cdot}13H_2O$ on the X-ray patterns. The dicalcium compound presumably was decomposed to the tetracalcium and amorphous alumina. This reaction was not reversible.

Owing to the extreme slowness of dissolution at 1° C, the solubility curve of gibbsite was not established.

During the earlier stages of this study the author was ably assisted by G. J. Halley. The X-ray diffraction patterns were prepared by H. E. Swanson and coworkers of the Microstructure Section. Their assistance is hereby gratefully acknowledged.

5. References

[1] H. H. Steinour, Aqueous cementitious systems containing lime and alumina, Research and Develop. Lab. Portland Cement Assoc., Research Dept. Bul. 34 (Feb. 1951).

[2] R. H. Bogue, The chemistry of portland cement, 2d ed. (Reinhold Publ. Corp., New York, N. Y., 1955).

[3] F. M. Lea, The chemistry of cement and concrete, 2d ed. (St. Martin's Press, Inc., New York, N. Y., 1956).

[4] G. E. Bessey, The calcium aluminate and silicate hydrates, Proc. of the Symposium on the Chem. of Cements, Stockholm, 1938. Ingeniörs Vetenskaps Akad., p. 178, Stockholm (1939).

[5] L. S. Wells, W. F. Clarke, and H. F. McMurdie, Study of the system CaO-Al_2O_3-H_2O at temperatures of 21° and 90° C, J. Research NBS **30**, 367 (1943) RP1539.

[6] J. D'Ans and H. Eick, The system CaO-Al_2O_3-H_2O at 20° C and the hardening of aluminous cements. Zement-Kalk-Gips **6,** 197 (1953).

[7] R. P. Peppler and L. S. Wells, The system of lime, alumina, and water from 50° to 250° C, J. Research NBS **52,** 75 (1954) RP2476.

[8] A. J. Majumdar and R. Roy, The system CaO-Al_2O_3-H_2O, J. Am. Ceram. Soc. [12] **39,** 434 (1956).

[9] G. Assarsson, The conditions of formation of the hydrated compounds in the system CaO-Al_2O_3-H_2O (liquid) and the hydration of the anhydrous calcium aluminates, Sveriges Geol. Undersökn [C] **30,** No. 399, p. 202 (1936).

[10] L. S. Wells and E. T. Carlson, Hydration of aluminous cements and its relation to the phase equilibria in the system lime-alumina-water, J. Research NBS **57,** 335 (1956) RP2723.

[11] H. Bassett, Notes on the system lime-water, and on the determination of calcium, J. Chem. Soc., part II, 1270 (1934).

[12] R. Hedin, Saturation concentration of calcium hydroxide, Svenska Forskningsinst. för Cement Betong vid Kgl. Tek. Högskol. Stockholm, Handl. No. 27, p. 14 (1955).

[13] E. T. Carlson, Some observations on hydrated monocalcium aluminate and monostrontium aluminate, J. Research NBS **59,** 107 (1957) RP2777.

[14] R. Salmoni, The dicalcium aluminate hydrates, Gazz. chim. ital. **64,** 719 (1934).

[15] R. Turriziani and G. Schippa, On the existence of hydrated calcium monocarboaluminate, Ricerca sci. **26,** 2792 (1956).

[16] A. W. Myers, C. E. Rogers, V. Stannett, and M. Szwarc, Permeability of polyethylene to gases and vapors, Modern Plastics **34,** No. 9, 157 (1957).

[17] J. Farran, Mineralogical contribution to the study of the adherence between the hydrated constituents of cements and the embedded materials, Rev. matériaux construct. et trav. publ., C. No. 490, 155; No. 492, 191 (1956).

[18] M. H. Roberts, New calcium aluminate hydrates. J. Appl. Chem. **7,** 543 (1957).

[19] G. Schippa and R. Turriziani, The Hydrated calcium aluminates. Ricerca sci. **27,** 3654 (1957).

WASHINGTON, December 27, 1957.

Journal of Research of the National Bureau of Standards Vol. 61, No. 1, July 1958 Research Paper 2878

Heat Content of Zirconium and of Five Compositions of Zirconium Hydride from 0° to 900° C[1]

Thomas B. Douglas and Andrew C. Victor

Using a precise Bunsen ice calorimeter, a "silver core" furnace, and a "drop" method, the heat content (enthalpy) of zirconium metal and five samples of zirconium hydride (24 to 52 atomic percent hydrogen) was measured over the range 0° to 900° C. Thermal hysteresis of the hydrides was investigated in several cases, and corrections were applied for the impurities in the samples. At each temperature up to 550° C the heat contents of the hydrides relative to 0° C were found to vary linearly with composition, a fact in accord with the phase diagram of the system. The effective heat capacity of each hydride sample reached its maximum value between 550° and 600° C, a behavior that can be interpreted as due to the endothermic formation of the high-temperature beta phase.

1. Introduction

The fact that palladium metal absorbs considerable amounts of hydrogen gas has been known for a very long time. Although many metals form similar alloylike solid hydrides, those of the family of chemical elements titanium, zirconium, hafnium, and thorium have become well known because of their ease of formation, wide ranges of composition, and relative stability. In the case of zirconium no gaseous hydrides are known, but the metal expands and absorbs continuously variable amounts of hydrogen even at room temperature, forming brittle, metalliclike materials whose compositions approach ZrH_2. Only those with the largest amounts of hydrogen have decomposition pressures that exceed 1 atm below 1,000° C.

Many of the physical properties of the zirconium hydrides have been investigated intensively, especially in recent years. These properties include their crystal structures as determined by X-ray and neutron diffraction, their paramagnetic susceptibilities, and the diffusion rates and equilibrium pressures of hydrogen at various temperatures and compositions. This paper reports an extensive series of measurements of the heat content of zirconium and five compositions of its hydrides from 0° to 900° C.

2. Samples and Their Compositions

The samples of zirconium hydride whose heat contents were measured are listed in table 1 in the order of increasing hydrogen content. Their compositions, corrected for chemical impurities in the manner presently to be described, are expressed in several forms that are commonly used. Zirconium metal is included with the hydrides, as it is a member of the series not only in a formal sense but also in terms of its properties. The zirconium sample was crystal-bar material, and was obtained from the U. S. Bureau of Mines, Albany, Oregon.

In the case of pure zirconium hydrides the three ways of expressing the hydrogen content used in table 1 are related to one another, and to the hydrogen as parts per million by weight (ppm), by the following numerical formulas. (The symbols are defined in table 1.)

TABLE 1. *Samples and their compositions*

Sample	Source of sample	Composition		
		Weight % H (w)	Atom % H (A)	Atomic ratio H/Zr (x)
1	U. S. Bureau of Mines	0.000	0.0	0.000
2	Wright Air Dev. Ctr.	.356	24.5	.324
3	Sylvania	.611	35.7	.556
4	do	.769	41.2	.701
5	do	1.092	50.0	.999
6	Wright Air Dev. Ctr.	1.170	51.7	1.071

$$\text{ppm}=10{,}000w=110.5A/(1-0.00989A)=11{,}050x/(1+0.01105x) \quad (1)$$

$$A=90.50w/(1+0.895w)=100x/(1+x) \quad (2)$$

$$x=0.905w/(1-0.01w)=A/(100-A). \quad (3)$$

The methods used in preparing the hydride samples were as follows: Samples 2 and 6 were prepared by the Power Plant Laboratory of the Wright Air Development Center. The zirconium used had been prepared by the Carborundum Metal Corporation. The hydriding temperature was 1,800°F (982°C), and a period of 2 hr was allowed in order to preclude temperature gradients along the bar. The furnace was shut down thereafter and the bar cooled in the furnace for at least 8 hr. The percentages of hydrogen furnished with the samples were determined by the manufacturer by three different methods, described as vacuum fusion, weight gain, and volumetric analysis. The three methods agreed very closely, and the estimated accuracy was stated to be of the order of 0.5 percent of the hydrogen present. Samples 2 and 6 were each supplied in two pieces, which were measured as a single sample to increase the precision, as in each case both pieces were stated to have the same composition and were found to have room-temperature densities that were identical within the uncertainty of measurement.

[1] This work was supported by the U. S. Air Force, Wright Air Development Center, under USAF Delivery Order No. AF 33 (616) 56-21. The contract was initiated under Project No. 7360, "Materials Analysis and Evaluation Techniques," Task No. 73603, "Thermal Measurements."

Samples 3, 4, and 5 were supplied by Sylvania Electric Products, Inc., Atomic Energy Division. It was stated that at the time of their preparation only a commercial grade of zirconium was available. The metal was heated to 920°C, and exposure to hydrogen gas was then begun. As the system slowly cooled (reaching 800°C in about 45 min), the pressure of hydrogen was maintained equal to the equilibrium pressure of the solid phase down to 0.2 atm. No further adjustments of pressure were made during the subsequent slow cooling overnight to room temperature, because it was believed that changes in the composition of the solid during this time were insignificant. It was stated that the greatest difference in temperature in any one sample did not exceed 4 deg C. Tests for homogeneity were not made on these particular samples, but were on others, which showed no composition differences within the accuracy of analyzing for hydrogen. The compositions of samples 3, 4, and 5 given in table 1 are based on analyses at Sylvania Electric Products, Inc., using a combustion method. Additional specimens that were approximate duplicates of these three compositions also were supplied. No heat-content measurements were made on them, but the parallel specimens were ground to a particle size of 60 to 100 mesh and were analyzed at the National Bureau of Standards for carbon and hydrogen by a combustion method. The hydrogen contents thus found differed from the values reported by Sylvania by amounts that, expressed as percentages of the hydrogen present, varied from −1.5 to +3 percent.

The chemical impurities found by analysis in the six samples are given in detail in table 2. These values were obtained by qualitative spectrographic analysis, except where otherwise indicated, and presumably no value was determined where none is listed. Samples 3, 4, and 5 themselves were not analyzed for carbon, but the value given is probably approximately correct, as it is the mean of those found (0.29 to 0.35%) for the duplicates of these samples.

TABLE 2. *Impurities in the zirconium hydride samples*

(Percentage by weight)

Element	Sample—					
	1	2	3	4	5	6
Hf	0.0145	0.01	[a]0.60	[a]0.44	[a]0.48	0.01
Fe	.030	.1	[a].88	[a].53	[a].41	.1
C	[b].02	[b].06	[b].32	[b].32	[b].32	[b].06
N	[b].005	[b].01	------	------	------	[b].01
O	[b].006	[b].017	------	------	------	[b].017
Si	<.002	------	[a].48	[a].35	[a].34	------
Ni	<.002	.007	[a].04	[a].08	[a].07	.007
Cr	<.001	.01	[a].10	[a].06	[a].06	.01
Al	.00025	.01	[a].12	[a].12	[a].17	.01
Mn	<.001	.01	[a]<.01	[a]<.01	[a]<.01	.01
Ti	.0035	------	[a].06	[a]<.01	[a]<.01	------
Pb	<.001	.005	[a].03	[a]<.01	[a]<.01	.005
Mg	<.001	.005	<.01	<.01	<.01	.005
Sn	<.0005	.005	<.001	<.01	<.01	.005
Be	------	.0001	------	------	------	.0001
V	<.002	.005	<.0001	<.0001	<.0001	.005
Ag	------	------	<.001	<.001	<.001	------
Ca	------	------	<.01	<.01	<.01	------
Cu	<.001	------	<.01	<.01	<.01	------
Zn	<.005	------	------	------	------	------
Cd	<.00005	------	<.0001	<.0001	<.0001	------
B	.00005	------	<.0001	<.0001	<.0004	------
Mo	<.001	------	<.0001	<.0001	<.0001	------
Co	<.0005	------	<.0001	<.0001	<.0001	------
Total.%	0.09	0.25	2.6	1.9	1.9	0.25

[a] By quantitative spectrographic analysis. [b] By chemical analysis.

The method of correcting the hydrogen compositions for the impurities shown by analysis is consistent with the method of correcting the thermal values described later, and was as follows: The total mass of those impurities whose small atomic sizes indicate clearly that they must be interstitial instead of substitutional in the zirconium lattice (carbon, nitrogen, and oxygen) were subtracted from the total sample mass. The remaining impurities were then assumed to be replaced atom for atom by zirconium before recalculating a corrected sample mass and a corrected percentage by weight of hydrogen.

3. Measurements of Heat Content

The calorimetric apparatus and method used have been described in critical detail in several reports and papers of the Bureau during the past 10 years [1].[2]

In the heat-content measurements the sample was contained in a thin-walled cylinder of the alloy 80Ni-20Cr sealed by a gold gasket. The hydride samples were not clad with any protective coating to prevent the escape of hydrogen, for in the worst case (at 900° C and 1-atm pressure of hydrogen) the 4 cm^3 of gas space in the container will hold only 0.08 mg of hydrogen gas, and this is only about 0.04 percent of the total hydrogen in the sample used. Small losses in mass attributed to loss of hydrogen did occur at the highest temperatures (800° C and above), as discussed later, but these aggregate losses equaled only a small fraction of the hydrogen in the solid sample. As the container appeared to remain sealed in most cases, these losses of hydrogen presumably occurred by diffusion through the container walls.

Briefly, the method of heat measurement was as follows: The specimen and container were suspended in the furnace for sufficient time to ensure their reaching the known constant temperature of the furnace, which was always adjusted to a rounded value. They were then allowed to fall into a precision Bunsen ice calorimeter, which, by absorbing mercury equivalent in volume to the shrinkage caused by the melting of ice, measured the heat evolved by the sample and container in cooling to 0° C. A similar measurement on the empty container at the same furnace temperature provided correction for the heat the container itself contributed and for the small amount of heat lost during the fall into the calorimeter. The furnace temperature was measured by a calibrated platinum-rhodium thermocouple, and below 650° C also by a calibrated platinum resistance thermometer to increase the accuracy and guard against any otherwise unknown

[2] Figures in brackets indicate the literature references at the end of this paper.

shift in the calibration of either the thermometer or the thermocouple. Before being sealed, the sample container was filled with pure helium gas, which also flowed through calorimeter and furnace cores during the measurements. This minimized the times required to reach thermal equilibrium and the oxidation of the container surfaces.

The heat leak of the calorimeter is normally small and quite constant, averaging only several tenths of a calorie per hour. In many of the measurements on the zirconium hydrides, particularly those with the highest hydrogen contents, the sample continued to evolve heat in the calorimeter (up to a total of 1 cal extra) for as long as 1½ hr beyond the 20 min normally required for reaching thermal equilibrium. This slow evolution of heat was presumably due to a slow approach to final phase equilibrium, and was taken into account when the precision of the measurements seemed to justify doing so. One of the authors has used the heat-content data reported in this paper to derive, by two independent methods, the shape of one of the boundaries of the zirconium-hydrogen phase diagram (the hydrogen-rich α boundary) from 0° to 550° C. The approximate agreement of the results, using the two methods, is evidence that in this temperature range approximate phase and thermal equilibrium were obtained in the present heat-content measurements [2].

The basic heat-content data obtained are given in detail in tables 3 to 8. Heat is expressed in calories (1 cal=4.1840 absolute joules). The second column indicates the relative chronological order of the individual runs with the sample, so that the effect of intervening exposure of the sample to other temperatures may be traced.

Each value recorded in the sixth column for the heat found for the empty container is the mean for two or more measurements at the particular furnace temperature, with the following exception. The heat content of the empty container was measured several times during the series of measurements, but only at 100-deg-C intervals from 100° to 900° C (and also at 550° C), and the values for all other temperatures were found from smooth plots of the deviations from simple monotonic empirical functions of temperature. In the present case, such interpolation led to errors less than those caused by the zirconium hydride samples themselves, although in the case of samples capable of being measured with the highest precision, this procedure would hardly be accurate enough. Different values for the empty container at the same temperature arose when in cases of emergency a new container or container part had to be substituted.

The tabulation "corrections for losses of H_2" that had occurred during exposure of the sample to the highest temperatures were made on an empirical basis, being estimated from the drift of heat values from run to run at the same temperature, from the relative duration of exposures to the high temperature, and from the losses of mass undergone by the sample. At two different temperatures, such as 850° and 900° C, it would be expected that the rates of drift of the heat value and the sample mass would be approximately proportional to the equilibrium pressures of hydrogen. This relationship was found to hold roughly, and led to the belief that the corrections applied are of at least the right order of magnitude, especially as the drifts were often decidedly outside the usual precision of measurement with this apparatus. (Presumably no problem of possibly sluggish reproportionation between two solid phases existed above 800° C.) It will be noted that this method of correction leads to exact agreement in the next-to-the-last column when only two measurements were made at the given temperature.

Alternatively, it would have been possible, in principle, to apply corrections for the losses of hydrogen calculated from a comprehensive correlation of the heat-content data with the phase diagram of the zirconium-hydrogen system. However, this was not practical for two reasons. In the first place, while it appeared that two of the samples each lost a total of 8 mg of hydrogen (most of this at 900° C), some of the loss may have been obscured by small gains of oxygen simulataneously acquired by the sample, and the two corrections are widely different per milligram change in sample mass. In the second place, the theoretical correlation would often have led to corrections that were uncertain because they involved small differences between relatively large numbers. It is interesting to note, however, that such a correlation was made and that in nearly every case the corrections so predicted had not only the same sign but also the same order of magnitude as those found empirically.

The hydride compositions were corrected for the chemical impurities by subtracting the mass of carbon, nitrogen, and oxygen and then assuming the remaining impurities to be replaced by the same number of zirconium atoms. The corresponding corrections to the heat values shown in tables 3 to 8 were made in two steps. First, the additively calculated heat contributions by the interstitial elements carbon, nitrogen, and oxygen were subtracted. Then it was assumed that the heat capacity of zirconium is the same *per atom* as that of the remaining impurities it was assumed to replace. However, in the case of carbon and silicon, appreciable deviations from equality of atomic heat capacities at the same temperature were taken into account by using the actual heat capacities of the free elements.

From the third columns of tables 3 to 8 it will be noted that in some runs the sample was first held for a while above the temperature of the measurement before being cooled for a final period of equilibration at the nominal temperature. (This elevated temperature was actually only 30 deg higher for zirconium at 870° C, and only 40 deg higher for the hydrides at 500° C.) These runs, in which equilibrium was approached from a higher temperature, were made for comparison with those approached from a lower temperature in order to set limits to the error in heat content that could have resulted from lack of phase equilibrium, and separate mean values have been recorded in the last columns of the table to show

TABLE 3. *Individual measurements of heat content—zirconium metal (sample 1)*

Furnace temperature, t	Order in which run was made	Time interval at—		Sample mass	Heat observed		Corrections for composition		Corrected $H_t - H_0$°C, net for sample	
		$t+50°$	$t°$		With sample	Container only	Loss of H_2	Impurities	Single run	Mean (set)
°C		min	min	g	cal	cal	cal g^{-1}	cal g^{-1}	cal g^{-1}	cal g^{-1}
100	16	0	31	20.0757	288.6	150.0	0.00	0.00	6.91	6.91
	17	0	31	20.0757	288.6	150.0	.00	.00	6.91	
	24	0	39	20.0757	288.6	150.0	.00	.00	6.90	
	25	0	44	20.0757	288.6	150.0	.00	.00	6.91	
200	18	0	38	20.0757	595.3	310.6	.00	−.01	14.17	14.08
	19	0	33	20.0757	594.3	310.6	.00	−.01	14.12	
	20	0	37	20.0757	593.2	310.6	.00	−.01	14.07	
	21	0	56	20.0757	593.4	310.6	.00	−.01	14.08	
	22	0	46	20.0757	592.2	310.6	.00	−.01	14.02	
	23	0	36	20.0757	593.8	310.6	.00	−.01	14.10	
	26	0	41	20.0757	594.9	310.6	.00	−.01	14.15	
	27	0	32	20.0757	592.7	310.6	.00	−.01	14.04	
	45	0	42	20.0757	592.9	311.6	.00	−.01	14.00	
	46	0	53	20.0757	593.6	311.6	.00	−.01	14.04	
300	7	0	43	20.0757	916.5	476.7	.00	−.04	[a] (21.87)	21.80
	8	0	35	20.0757	915.1	476.7	.00	−.04	21.80	
	9	0	47	20.0757	915.4	476.7	.00	−.04	21.81	
	10	0	48	20.0757	915.0	476.7	.00	−.04	21.79	
	11	0	31	20.0757	915.0	476.7	.00	−.04	21.79	
400	12	0	31	20.0757	1240.6	648.2	.00	−.03	29.48	29.44
	13	0	31	20.0757	1240.4	648.2	.00	−.03	29.46	
	47	0	47	20.0757	1239.2	651.0	.00	−.03	29.36	
	48	0	37	20.0757	1240.8	649.2	.00	−.03	29.44	
	49	0	51	20.0757	1241.1	649.2	--------	--------	29.45	
500	3	0	30	20.0757	1574.4	825.0	.00	−.04	37.29	37.37
	4	0	30	20.0757	1578.0	825.0	.00	−.04	37.47	
	5	0	31	20.0757	1576.9	825.0	.00	−.04	37.41	
	6	0	33	20.0757	1575.7	825.0	.00	−.04	37.35	
	14	0	31	20.0757	1575.5	825.0	.00	−.04	37.34	
	15	0	34	20.0757	1575.2	825.0	.00	−.04	37.33	
600	1	0	33	20.0757	1923.6	1009.5	.00	−.06	45.47	45.46
	2	0	50	20.0757	1923.1	1009.5	.00	−.04	45.45	
700	28	0	40	20.0757	2290.0	1204.0	.00	−.08	54.02	53.97
	29	0	50	20.0757	2288.7	1204.0	.00	−.08	53.95	
	30	0	42	20.0757	2288.7	1204.0	.00	−.08	53.95	
800	31	0	61	20.0757	2666.4	1408.0	.00	−.08	62.61	62.57
	32	0	55	20.0757	2666.4	1408.0	.00	−.08	62.61	
	37	0	50	20.0757	2664.8	1408.3	.00	−.08	62.51	
	38	0	60	20.0757	2665.4	1408.3	.00	−.08	62.54	
850	33	0	60	20.0757	2863.8	1510.8	.00	−.10	67.30	67.23
	34	0	62	20.0757	2864.3	1510.8	.00	−.10	67.32	
	39	0	62	20.0757	2861.6	1511.1	.00	−.10	67.17	
	40	0	53	20.0757	2860.7	1511.1	.00	−.10	67.14	
	59	0	78	15.0776	2528.3	1513.5	.00	−.10	67.20	
	60	0	66	15.0776	2528.8	1513.5	.00	−.10	67.23	
870	43	58	52	20.0757	3123.9	1552.7	.00	−.09	78.17	78.16
	44	64	70	20.0757	3123.2	1552.7	.00	−.09	78.14	
875	54	0	60	15.0776	2760.5	1565.6	.00	−.09	79.16	79.16
880	55	0	57	15.0776	2781.5	1576.1	.00	−.09	79.86	79.86
885	50	0	63	15.0776	2801.3	1586.5	.00	−.09	80.48	80.49
	52	0	72	15.0776	2803.5	1586.5	.00	−.09	80.62	
	58	0	70	15.0776	2799.5	1586.5	.00	−.09	80.36	
890	56	0	61	15.0776	2818.3	1597.0	.00	−.09	80.91	80.91
895	57	0	57	15.0776	2835.2	1607.5	.00	−.09	81.33	81.33
900	35	0	62	20.0757	3265.1	1614.3	.00	−.09	82.14	81.91
	36	0	80	20.0757	3263.3	1614.3	.00	−.09	82.05	
	41	0	60	20.0757	3258.6	1615.4	.00	−.09	81.76	
	42	0	61	20.0757	3258.8	1615.4	.00	−.09	81.77	
	51	0	62	15.0776	2854.2	1618.0	.00	−.09	81.90	
	53	0	58	15.0776	2853.5	1618.0	.00	−.09	81.85	

[a] Omitted from the mean because of inferior precision.

these differences. It will be noted, as one would expect, that in every case the higher heat was found when the approach was from a higher temperature. Also, longer times at the nominal temperature usually narrowed the discrepancy between the two directions of approach, though not rapidly enough to be a practical means of coming as close to equilibrium as the precision of the apparatus enables one to measure.

When a hydride sample had been measured at high temperatures, such as 900° C, before being remeasured at some lower temperature in the manner described above, the remeasurements were begun in the usual way by approaching the furnace temperature from a lower temperature, and the corrections applied for previous loss of hydrogen were calculated so as to give perfect agreement with the results ob-

TABLE 4. *Individual measurements of heat content—zirconium hydride 0.356% H by weight (sample 2)*

Furnace temperature, t	Order in which run was made	Time interval at—		Sample mass	Heat observed		Corrections for composition		Corrected $H_t - H_0°C$, net for sample	
		$t+50°$	$t°$		With sample	Container only	Loss of H_2	Impurities	Single run	Mean (set)
°C		min	min	g	cal	cal	cal g^{-1}	cal g^{-1}	cal g^{-1}	cal g^{-1}
100	13	0	67	19.8280	296.7	150.3	0.00	0.00	7.39	7.38
	14	0	43	19.8280	296.4	150.3	.00	.00	7.37	
200	15	0	42	19.8280	619.7	311.6	.00	−.02	15.52	15.50
	16	0	80	19.8280	618.9	311.6	.00	−.02	15.48	
300	6	0	63	19.8280	963.9	477.3	.00	−.04	24.50	24.49
	7	0	53	19.8280	963.5	477.3	.00	−.04	24.48	
400	4	0	64	19.8280	1337.6	650.6	.00	−.05	34.59	34.62
	5	0	50	19.8280	1338.7	650.6	.00	−.05	34.65	
500	1	0	61	19.8280	1733.1	812.6	.00	−.07	46.36	46.36
	2	0	48	19.8280	1733.2	812.6	.00	−.07	46.36	
	3	40	71	19.8280	1733.4	812.6	.00	−.07	46.37	46.37
540	23	0	69	19.1375	1881.0	899.8	+.15	−.08	51.34	51.38
	24	0	52	19.1375	1882.2	899.8	−.15	−.08	51.41	
550	8	0	64	19.8280	2062.1	918.0	−.15	−.08	57.62	57.86
	9	0	49	19.8280	2032.2	918.0	−.15	−.08	[a](56.11)	
	22	0	78	19.1375	2028.8	918.0	+.15	−.08	58.11	
600	10	0	52	19.8280	2561.8	1010.5	+.15	−.08	78.16	78.14
	11	0	72	19.8280	2560.9	1010.5	+.15	−.08	78.11	
	12	40	74	19.8280	2565.3	1010.5	+.15	−.08	78.33	78.37
	17	40	96	19.8280	2566.8	1010.5	+.15	−.08	78.41	
700	18	40	56	19.8280	2741.6	970.1	.00	−.11	89.24	89.24
	19	0	87	19.8280	2741.1	970.1	.00	−.11	89.21	89.21
800	20	0	70	19.8280	3083.1	1132.9	+.12	−.12	98.36	98.31
	21	0	57	19.8280	3079.3	1132.9	+.22	−.12	98.26	
900	25	0	61	19.1375	3675.6	1615.4	+.35	−.13	107.87	107.76
	26	0	76	19.1375	3668.9	1615.4	+.48	−.13	107.65	

[a] Given no weight. Apparently the time in the furnace was inadequate.

tained before the exposure to higher temperatures. This method of applying corrections for previous loss of hydrogen did not, of course, affect the principal purpose of making a new series of measurements, which was to ascertain the difference in heat resulting from heating and from cooling the sample to the desired furnace temperature.

4. Mean Heat Capacities of Zirconium and the Zirconium Hydride Samples

The heat content of zirconium has been measured by Mixter and Dana (0° to 100° C) [3], Jaeger and Veenstra (21° to 801° C) [4], Coughlin and King (25° to 1,098° C) [5], Skinner (25° to 1,000° C) [6], Redmond and Lones (150° to 1,050° C) [7], and Scott (60° to 960° C) [8]. Reviewing the first two investigations, Kelley [9] gave equations for the heat content and heat capacity over the range 25° to 627° C. Scott's zirconium had a purity comparable to that indicated in table 2, but presumably most of the earlier measurements were on samples containing considerable hafnium for which no corrections were applied. According to Dulong and Petit's law, in the case of zirconium each 1 percent of hafnium would lower the observed heat content and heat capacity per unit mass by about ½ percent.

Pure zirconium metal undergoes a transformation of crystalline structure at a temperature that, partly due to its sensitivity to small amounts of certain impurities, does not seem to be known very precisely. Coughlin and King [5] observed a rapid rise in heat content over a range of some 80 deg C. Since it is known that oxygen or nitrogen, when dissolved in the metal, has such an effect, they assumed their sample to contain one or both of these impurities. The heat-content measurements of Redmond and Lones [7] were of low precision, and they reported no evidence for a heat-absorbing transformation. Though two investigators [6, 8] reported 870° C as the transformation temperature, two compilations [10, 11] have given 862° and 863° C, respectively, and the last temperature has been somewhat arbitrarily assumed in this paper. (The assumption of another of these temperatures would have had very little effect on the value of the heat of transformation derived from the data.)

The present authors were limited by their apparatus to temperatures not higher than 40 deg C above the transformation temperature. As the preliminary measurements at 870° and 900° C had indicated a value for the mean heat capacity between these two temperatures of 11 cal/g atom-deg C, a value that seems too high for this element, additional measurements of heat content were made at 5-deg intervals over this temperature range. The mean relative heat content at each of these temperatures (last column of table 3) is plotted in figure 1. Considering the very small temperature intervals and the large magnitudes of all these measured heats, the precision is good; but (above the transformation temperature) there is a decided negative curvature at the lower temperatures, which may be due to small amounts of oxygen and nitrogen.

TABLE 5. *Individual measurements of heat content—zirconium hydride, 0.611% H by weight (sample 3)*

Furnace temperature, t	Order in which run was made	Time interval at—		Sample mass	Heat observed		Corrections for composition		Corrected $H_t - H_{0°C}$, net for sample	
		$t+50°$	$t°$		With sample	Container only	Loss of H_2	Impurities	Single run	Mean (set)
°C		min	min	g	cal	cal	cal g^{-1}	cal g^{-1}	cal g^{-1}	cal g^{-1}
100	1	0	54	19.6516	291.6	150.4	0.00	−0.16	[a](7.02)	
	2	0	40	19.6516	303.5	150.4	.00	−.16	7.63	7.62
	3	0	42	19.6516	303.7	150.4	.00	−.16	7.64	
	4	0	52	19.6516	303.0	150.4	.00	−.16	7.60	
200	5	0	54	19.6516	640.2	310.3	.00	−.36	16.42	16.42
	6	0	37	19.6516	640.1	310.3	.00	−.36	16.42	
300	7	0	47	19.6516	1011.4	475.3	.00	−.58	26.70	26.70
	8	0	41	19.6516	1011.2	475.3	.00	−.58	26.69	
400	9	0	42	19.6515	1402.7	648.0	.00	−.85	37.55	37.57
	10	0	38	19.6516	1403.0	648.0	.00	−.85	37.57	
	13	0	51	19.6516	1402.5	648.0	.00	−.85	37.55	
	19	0	40	19.6516	1404.4	648.0	.00	−.85	37.64	
	20	0	51	19.6516	1404.3	648.0	.00	−.85	37.64	
	25	0	55	19.6516	1402.7	648.0	.00	−.85	37.56	
	26	0	40	19.6516	1402.6	648.0	.00	−.85	37.55	
	27	0	56	19.6516	1402.0	648.0	.00	−.85	37.52	
	28	0	41	19.6516	1402.9	648.0	.00	−.85	37.57	
500	11	0	54	19.6516	1831.5	826.3	.00	−1.12	50.03	50.00
	12	0	40	19.6516	1830.6	826.3	.00	−1.12	49.98	
	40	0	52	18.8850	1789.6	827.0	+.09	−1.12	49.94	
	41	0	71	18.8850	1791.7	827.0	+.09	−1.12	50.06	
	42	41	55	18.8850	1791.1	827.0	+.09	−1.12	50.03	50.02
	43	38	43	18.8850	1790.7	827.0	+.09	−1.12	50.00	
550	16	0	50	19.6516	2063.6	916.8	.00	−1.29	57.07	57.02
	17	0	76	19.6516	2062.2	916.8	.00	−1.29	57.00	
	18	0	40	19.6516	2061.8	916.8	.00	−1.29	56.98	
575	29	0	45	19.6516	2386.1	962.9	.00	−1.52	70.90	70.1
	30	0	76	19.6516	2404.8	962.9	.00	−1.52	71.85	
	33	0	110	19.6516	2318.4	962.9	.00	−1.52	67.46	
600	14	0	41	19.6516	2663.2	1009.8	.00	−1.72	82.42	82.36
	15	0	80	19.6516	2660.7	1009.8	.00	−1.72	82.29	
	36	0	40	18.8850	2578.4	1010.5	+1.05	−1.72	82.35	
	37	0	80	18.8850	2578.8	1010.5	+1.05	−1.72	82.37	
	38	41	40	18.8850	2642.1	1010.5	+1.05	−1.72	85.72	85.67
	39	40	78	18.8850	2640.1	1010.5	+1.05	−1.72	85.62	
650	31	0	40	19.6516	2953.6	1106.8	0.00	−1.90	92.08	92.12
	32	0	52	19.6516	2955.0	1106.8	.00	−1.90	92.15	
	44	0	40	18.8850	2870.4	1115.7	+1.11	−1.90	92.12	
	45	0	61	18.8850	2870.6	1115.7	+1.11	−1.90	92.14	
	46	40	60	18.8850	2871.6	1115.7	+1.11	−1.90	92.19	92.24
	47	40	93	18.8850	2873.4	1115.7	+1.11	−1.90	92.28	
700	21	0	54	19.6516	3174.3	1205.6	0.00	−2.05	98.13	98.15
	22	0	40	19.6516	3175.1	1205.6	.00	−2.05	98.17	
800	23	0	40	19.6516	3624.9	1409.1	+.07	−2.34	110.48	110.48
	24	0	50	19.6516	3623.1	1409.1	+.16	−2.34	110.48	
900	34	0	40	19.6516	4059.9	1616.1	+.38	−2.61	122.13	122.13
	35	0	55	19.6516	4053.8	1616.1	+.69	−2.61	122.13	

[a] Omitted from the mean because of inferior precision.

The straight line was drawn on the assumption that the scatter of points at and above 880° C is random. The mean heat capacity of β-zirconium corresponding to the slope of this line is subject to considerable uncertainty because of the smallness of the total temperature interval. Extrapolation to the transformation temperature leads to a value of 9.8 cal g^{-1} for the heat of transformation of the metal. The following values (in the same units) have previously been given: 4.7 [12], 7.7 [10], 10.1 [5], 10.9 [8], and 11.4 [6]. The large spread of these values is undoubtedly largely due to the usual necessity of interpolating the heat content of this element through a considerable temperature range because the transformation indicated by the thermal data was not sharp.

In table 9 are given the values of mean heat capacity of zirconium observed in the present investigation. These values were calculated from the differences between successive values in the last column of table 3 up to 850° C, and from the line in figure 1 above 863° C. Also given for comparison are the percentage deviations of the smoothed values of other investigators from the values of the second column.

Similarly, the mean observed heat capacities of the five samples of zirconium hydride whose heat contents were measured were calculated for the temperature intervals of measurement from the successive differences in the last columns of tables 4 to 8. These values are given in table 10. (The compositions may be identified from table 1.) In the intervals where the apparant heat capacity was found to be unusually large, particularly between 550° and 600° C, extensive phase transformation was occurring, and as a consequence the effective

TABLE 6. *Individual measurements of heat content—zirconium hydride, 0.769% H by weight (sample 4)*

Furnace temperature, t	Order in which run was made	Time interval at—		Sample mass	Heat observed		Corrections for composition		Corrected $H_t - H_0°C$, net for sample	
		$t+50°$	$t°$		With sample	Container only	Loss of H_2	Impurities	Single run	Mean (set)
°C		min	min	g	cal	cal	cal g^{-1}	cal g^{-1}	cal g^{-1}	cal g^{-1}
100	1	0	56	19.3007	303.2	150.4	0.00	−0.12	7.79	7.80
	2	0	39	19.3007	303.2	150.4	.00	−.12	7.80	
200	3	0	55	19.3007	642.6	310.3	.00	−.29	16.92	16.93
	4	0	40	19.3007	642.8	310.3	.00	−.29	16.94	
300	5	0	56	19.3007	1019.8	475.3	.00	−.48	27.73	27.71
	6	0	41	19.3007	1019.0	475.3	.00	−.48	27.69	
400	7	0	58	19.3007	1414.1	648.0	.00	−.71	38.98	38.97
	8	0	40	19.3007	1413.6	648.0	.00	−.71	38.96	
500	9	0	56	19.3007	1847.4	826.3	.00	−.92	51.98	51.99
	10	0	41	19.3007	1847.7	826.3	.00	−.92	52.00	
	30	0	60	19.3007	1847.6	826.3	+.05	−.92	52.05	
	31	0	57	19.3007	1845.8	826.3	+.05	−.92	51.95	
	32	0	60	19.3007	1845.8	826.3	+.05	−.92	51.95	
	33	0	60	19.3007	1846.7	826.3	+.05	−.92	52.00	
550	13	0	56	19.3007	2085.9	917.4	.00	−1.06	59.48	59.54
	14	0	187	19.3007	2091.1	917.4	.00	−1.06	59.75	
	15	0	52	19.3007	2084.2	917.4	.00	−1.06	59.39	
560	20	0	56	19.3007	2217.4	935.9	.00	−1.11	65.29	64.5
	21	0	126	19.3007	2199.5	935.9	.00	−1.11	64.36	
	22	0	62	19.3007	2189.6	935.9	.00	−1.11	63.85	
575	18	0	53	19.3007	2508.5	963.7	.00	−1.28	78.76	78.67
	19	0	89	19.3007	2505.1	963.7	.00	−1.28	78.58	
600	11	0	56	19.3007	2722.3	1009.8	.00	−1.40	87.33	87.37
	12	0	89	19.3007	2723.9	1009.8	.00	−1.40	87.41	
	35	0	42	16.7834	2507.0	1021.7	+.17	−1.40	87.27	
	36	0	73	16.7834	2510.6	1021.7	+.17	−1.40	87.48	
	37	40	61	16.7834	2535.8	1021.7	+.17	−1.40	88.99	88.88
	38	40	95	16.7834	2532.4	1021.7	+.17	−1.40	88.78	
650	16	0	51	19.3007	3037.2	1107.0	.00	−1.55	98.46	98.41
	17	0	40	19.3007	3035.2	1107.0	.00	−1.55	98.35	
	39	0	43	16.7834	2779.5	1115.7	+.83	−1.55	98.42	
	40	0	69	16.7834	2779.2	1115.7	+.83	−1.55	98.40	
	41	41	66	16.7834	2778.9	1115.7	+.83	−1.55	98.38	98.42
	42	41	90	16.7834	2780.2	1115.7	+.83	−1.55	98.45	
700	23	0	50	19.3007	3252.5	1205.6	.00	−1.67	104.38	104.36
	24	0	41	19.3007	3251.6	1205.6	.00	−1.67	104.34	
800	25	0	45	19.3007	3691.4	1409.1	+.07	−1.90	116.42	116.39
	26	0	42	19.3007	3688.2	1409.1	+.14	−1.90	116.32	
	27	0	45	19.3007	3689.1	1409.1	+.21	−1.90	116.44	
900	28	0	55	19.3007	4127.6	1616.1	+.48	−2.12	128.48	128.48
	29	0	40	19.3007	4124.1	1616.1	+.68	−2.12	128.50	
	34	0	50	19.3007	4118.6	1616.1	+.93	−2.12	128.47	

heat capacity was not only changing rapidly with temperature but the mean values recorded are subject to large uncertainties because of the impossibility of reaching equilibrium in the measurements within a reasonable time. On the other hand, in those temperature ranges where mean heat capacity appears to vary regularly with temperature (particularly from 0° to 540° or 550° C), it is justifiable to assume the recorded values to be the instantaneous heat capacities in the middle of their respective temperature ranges and to interpolate for intermediate temperatures in the usual way.

The regions of regular variation can be more quickly located by an inspection of figure 2, since for each composition, each two adjacent points are connected by a straight line whose slope is proportional to the corresponding value in table 10. It is also justifiable to interpolate for values for intermediate compositions at any temperature up to 540° C, as discussed in section 5.

5. Discussion of the Heat Capacities of the Hydride Samples

The observed discontinuities in the heat-capacity-temperature functions of the five samples of zirconium hydride can be interpreted qualitatively in terms of the phase diagram of the system. One version of this diagram is shown in figure 3. The three solid solutions indicated are designated α, β, and γ. A similar diagram was given by Vaughan and Bridge as a result of their high-temperature X-ray diffraction studies [13]; but the results of different investigators, using various methods, do not agree well as to the shapes of some of the phase-field boundaries, two of which seem to be particularly uncertain and are therefore shown as dashed lines. The dotted vertical lines and their points indicate the compositions and temperatures for which measured values of relative heat content are reported in this paper.

TABLE 7. *Individual measurements of heat content—zirconium hydride, 1.029% H by weight (sample 5)*

Furnace temperature, t	Order in which run was made	Time interval at—		Sample mass	Heat observed		Corrections for composition		Corrected $H_t - H_{0°C}$, net for sample	
		$t+50°$	$t°$		With sample	Container only	Loss of H_2	Impurities	Single run	Mean (set)
°C		min	min	g	cal	cal	cal g^{-1}	cal g^{-1}	cal g^{-1}	cal g^{-1}
100	1	0	51	18.9319	306.5	150.0	0.00	−0.12	8.15	8.15
	2	0	44	18.9319	306.5	150.0	.00	−.12	8.15	
200	3	0	40	18.9319	655.7	310.6	.00	−.30	17.93	18.00
	4	0	41	18.9319	656.3	310.6	.00	−.30	17.96	
	5	0	41	18.9319	657.5	310.6	.00	−.30	18.02	
	14	0	42	18.9319	679.4	310.6	.00	−.30	[a](19.18)	
	15	0	56	18.9319	658.0	310.6	.00	−.30	18.05	
	16	0	43	18.9319	658.0	310.6	.00	−.30	18.05	
300	6	0	38	18.9319	1050.1	476.7	.00	−.49	29.80	29.69
	7	0	41	18.9319	1048.7	476.7	.00	−.49	29.72	
	8	0	45	18.9319	1048.4	476.7	.00	−.49	29.71	
	17	0	46	18.9319	1046.3	476.4	.00	−.49	29.60	
	18	0	54	18.9319	1045.8	476.4	.00	−.49	29.57	
	19	0	42	18.9319	1049.0	476.4	.00	−.49	29.74	
400	11	0	60	18.9319	1462.4	648.2	.00	−.73	42.27	42.30
	12	0	48	18.9319	1461.3	648.2	.00	−.73	42.22	
	13	0	53	18.9319	1461.2	648.2	.00	−.73	42.21	
	33	0	46	18.9319	1464.1	648.2	.00	−.73	42.37	
	34	0	60	18.9319	1464.9	648.2	.00	−.73	42.41	
	41	0	48	18.9319	1456.0	648.2	+.38	−.73	42.32	
	42	0	61	18.9319	1455.7	648.2	+.38	−.73	42.30	
500	9	0	57	18.9319	1910.4	825.0	.00	−.97	56.36	56.39
	10	0	43	18.9319	1911.7	825.0	.00	−.97	56.43	
	43	0	50	17.2397	1796.3	812.6	+.30	−.97	56.39	
	44	0	70	17.2397	1796.3	812.6	+.30	−.97	56.39	
	45	40	52	17.2397	1798.7	812.6	+.30	−.97	56.53	56.59
	46	30	80	17.2397	1800.8	812.6	+.30	−.97	56.65	
550	20	0	53	18.9319	2164.4	917.2	.00	−1.11	64.77	64.56
	21	0	41	18.9319	2160.3	917.2	.00	−1.11	64.56	
	22	0	62	18.9319	2158.4	917.2	.00	−1.11	64.45	
	23	0	75	18.9319	2158.4	917.2	.00	−1.11	64.45	
575	26	0	60	18.9319	2384.2	963.4	.00	−1.23	73.82	73.62
	27	0	64	18.9319	2376.8	963.4	.00	−1.23	73.43	
600	24	0	62	18.9319	2561.3	1009.5	.00	−1.33	80.64	80.67
	25	0	70	18.9319	2562.6	1009.5	.00	−1.33	80.71	
	47	0	51	17.2397	2408.0	992.9	−.10	−1.33	80.66	
	48	0	72	17.2397	2408.3	992.9	−.10	−1.33	80.67	
	49	40	52	17.2397	2416.0	992.9	−.10	−1.33	81.12	81.10
	50	40	79	17.2397	2415.5	992.9	−.10	−1.33	81.09	
650	28	0	60	18.9319	2878.4	1107.9	.00	−1.49	92.03	92.02
	29	0	53	18.9319	2877.8	1107.9	.00	−1.49	92.00	
700	30	0	54	18.9319	3179.5	1204.0	.00	−1.67	102.68	102.77
	31	0	60	18.9319	3182.4	1204.0	.00	−1.67	102.83	
	32	0	75	18.9319	3181.9	1204.0	.00	−1.67	102.81	
	51	0	53	17.2397	2991.6	1182.9	−.54	−1.67	102.70	
	52	0	72	17.2260	2992.3	1182.9	−.54	−1.67	102.83	
	53	43	67	17.2260	3011.1	1182.9	−.54	−1.67	[b](103.92)	103.02
	54	43	91	17.2260	2995.7	1182.9	−.54	−1.67	103.02	
750	35	0	60	18.9319	3478.7	1305.3	.00	−1.82	112.98	113.01
	36	0	63	18.9319	3479.8	1305.3	.00	−1.82	113.04	
800	37	0	60	18.9319	3786.4	1408.0	.00	−1.97	123.66	123.76
	38	0	85	18.9319	3790.3	1408.0	.00	−1.97	123.87	
850	39	0	61	18.9319	4086.2	1510.8	+.40	−2.14	134.30	134.32
	40	0	60	18.9319	4086.9	1510.8	+.40	−2.14	134.34	
	55	0	57	17.2260	3836.5	1510.8	+1.45	−2.14	134.32	
	56	0	61	17.2260	3830.5	1510.8	+1.80	−2.14	134.32	
900	57	0	61	17.2260	4044.3	1615.4	+2.26	−2.25	141.01	141.01
	58	0	58	17.2260	4028.4	1615.4	+3.18	−2.25	141.01	

[a] Omitted from mean because of inferior precision. [b] Given no weight. Apparently the time in the furnace was inadequate.

The mean observed heat contents up to 500° C of zirconium and the five hydride samples, taken from the last columns of tables 3 to 8 and converted to cal mole^{-1} of ZrH_x, are plotted against the over-all composition x in figure 4. The linearity of the values for the five hydride samples is in general good and accords with the prediction of the phase diagram (fig. 3) that these five samples are mixtures in different proportions of the same two phases at each temperature up to 550° C. (The sample $ZrH_{0.234}$ obeys this relation only up to 540° C.) In fact, the proximity of the observed points to the fairly steep lines at the higher temperatures may be considered to afford an approximate check on the general interconsistency of the hydride compositions found by analysis. The coefficients of the equations of the straight lines drawn through these points in figure 4 were determined by the method of least squares and

TABLE 8. *Individual measurements of heat content—zirconium hydride, 1.170% H by weight (sample 6)*

Furnace temperature, t	Order in which run was made	Time interval at—		Sample mass	Heat observed		Corrections for composition		Corrected $H_t - H_{0°C}$, net for sample	
		$t+50°$	$t°$		With sample	Container only	Loss of H_2	Impurities	Single run	Mean (set)
°C		min	min	g	cal	cal	cal g^{-1}	cal g^{-1}	cal g^{-1}	cal g^{-1}
100	10	0	58	18.6311	276.1	122.9	0.00	−0.01	8.21	8.23
	11	0	66	18.6311	276.8	122.9	.00	−.01	8.25	
200	12	0	65	18.6311	593.3	251.9	.00	−.03	18.29	18.29
300	7	0	55	18.6311	944.8	385.8	.00	−.04	30.10	29.99
	8	0	84	18.6311	943.2	385.8	.00	−.04	29.88	
400	9	0	57	18.6311	1321.0	524.2	.00	−.05	42.72	42.72
500	1	0	73	18.6311	1735.2	666.6	.00	−.08	57.27	57.27
	2	45	93	18.6311	1739.2	666.6	.00	−.08	57.49	57.49
550	3	0	66	18.6311	1981.6	740.5	.00	−.08	66.53	66.42
	4	0	57	18.6311	1977.4	740.5	.00	−.08	66.31	
600	5	0	73	18.6311	2451.0	815.2	.00	−.09	87.71	87.71
	6	40	72	18.6311	2458.0	815.2	.00	−.09	88.08	88.08
700	13	0	80	16.6219	3044.8	1207.6	.00	−.11	110.43	110.42
	14	0	61	16.6219	3044.2	1207.6	.00	−.11	110.40	
800	15	0	60	16.6219	3587.8	1410.7	.00	−.13	130.86	130.92
	16	0	50	16.6219	3589.8	1410.7	.00	−.13	130.98	
850	17	0	52	16.6219	3799.5	1513.5	+.17	−.14	137.57	137.57
	18	0	64	16.6219	3795.5	1513.5	+.41	−.14	137.57	
900	19	0	50	16.6219	3996.2	1618.0	+1.11	−.15	144.05	144.05
	20	0	60	16.6219	3972.8	1618.0	+2.52	−.15	144.05	

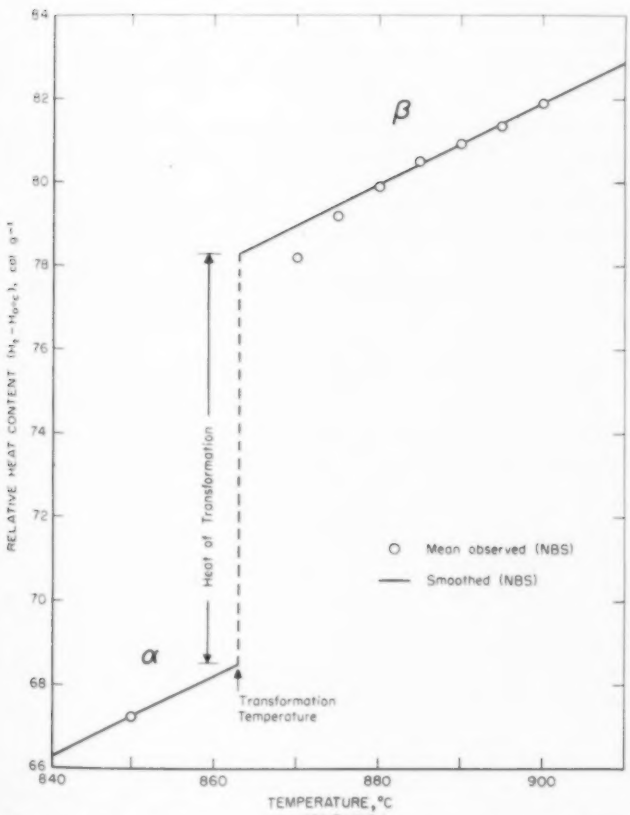

FIGURE 1. *Heat content of zirconium near its transformation temperature.*

are given in table 11. These relations can be used as a means of interpolating below 550° C for smooth values of the relative heat contents of compositions on which no measurements were made.

The phase diagram shown in figure 3 indicates a first-order phase transition at a eutectoid temperature of approximately 550° C. Though the slopes in figure 2 represent only average heat capacities over the finite temperature intervals of measurement, it is apparent that the heat capacity of each hydride sample reaches a maximum value within the range 540° to 600° C, corresponding to this phase transition. However, it will be observed that the particularly high heat capacities are spread over a temperature range, a fact to be interpreted as due to considerable lack of phase equilibrium at these temperatures. This is not an unusual situation in the case of all-solid systems. The interpretation is supported by the unusually poor reproducibility of duplicate heat values at 560° and 575° C and the hysteresis found at 600° C, as may be noted from the last two columns of tables 4 to 8.

As the temperature rises above 600° C, the heat capacities of samples 3 to 6 decrease rather abruptly to smaller values at temperatures that differ for the four samples. This fact also can be given a qualitative interpretation in terms of the phase diagram, for above a certain temperature each hydride sample investigated should become all β phase, and therefore at higher temperatures there would no longer be a contribution to the over-all, or observed, heat capacity by latent heat of phase reproportionation.

TABLE 9. *Mean observed heat capacities of zirconium metal*

Temperature interval	Mean heat capacity (this investigation)	Deviations of smoothed values of other investigators				
		Bulletin 476 [9]	Coughlin and King [5]	Skinner [6]	Redmond and Lones [7]	Scott [8]
°C	*cal g⁻¹ deg C⁻¹*	%	%	%	%	%
0 to 100	0.0691	−2	+1	−3	+2	−2
100 to 200	.0717	−3	+4	−2	+5	−3
200 to 300	.0772	−6	+1	−5	+2	−8
300 to 400	.0764	0	+5	0	+8	−6
400 to 500	.0793	+2	+3	−1	+9	−7
500 to 600	.0809	+5	+3	0	+11	−7
600 to 700	.0851	-----	0	−2	+10	−9
700 to 800	.0860	-----	+1	0	+13	−7
800 to 850	.0932	-----	−6	−6	+7	−11
850 to 863	.099	-----	−11	−10	+2	−15
Heat of transformation (cal g⁻¹)	9.8	-----	+3	+17	-----	+11
863 to 900	0.097	-----	−18	−24	-----	−26

TABLE 10. *Mean observed heat capacities of five samples of zirconium hydride*

Temperature range	Sample 2 (x=0.324)	Sample 3 (x=0.556)	Sample 4 (x=0.701)	Sample 5 (x=0.999)	Sample 6 (x=1.071)
°C	*cal g⁻¹ deg C⁻¹*	*cal g⁻¹ deg C⁻¹*	*cal g⁻¹ deg C⁻¹*	*cal g⁻¹ deg C⁻¹*	*cal g⁻¹ deg C⁻¹*
0 to 100	0.0738	0.0762	0.0780	0.0815	0.0823
100 to 200	.0812	.0880	.0913	.0985	.1006
200 to 300	.0899	.1028	.1078	.1169	.1170
300 to 400	.1013	.1087	.1126	.1261	.1273
400 to 500	.1174	.1244	.1302	.1419	.1466
500 to 540	.1255	.1402	.1510	.1614	.1808
540 to 550	.648				
550 to 560	.408	.522	.50	.362	.430
560 to 575			.945		
575 to 600		.56	.378	.290	
600 to 650	.1096	.163	.206	.2228	.2252
650 to 700		.1194	.1188	.2176	
700 to 750	.0909	.1233	.1203	.2022	.2050
750 to 800				.2150	
800 to 850	.0945	.1165	.121	.2112	.1330
850 to 900				.134	.130

TABLE 11. *Equations of smoothed heat content versus composition of zirconium hydrides up to 550°C*

$H_t - H_{0°C} = A + Bx$, cal per mole of ZrH_x		
Temperature, t	A	B
°C		
100	637.5	114.0
200	1305.6	356.5
300	2041.8	694.9
400	2849.4	1039.7
500	3794.2	1410.0
550	4277.0	1705.8

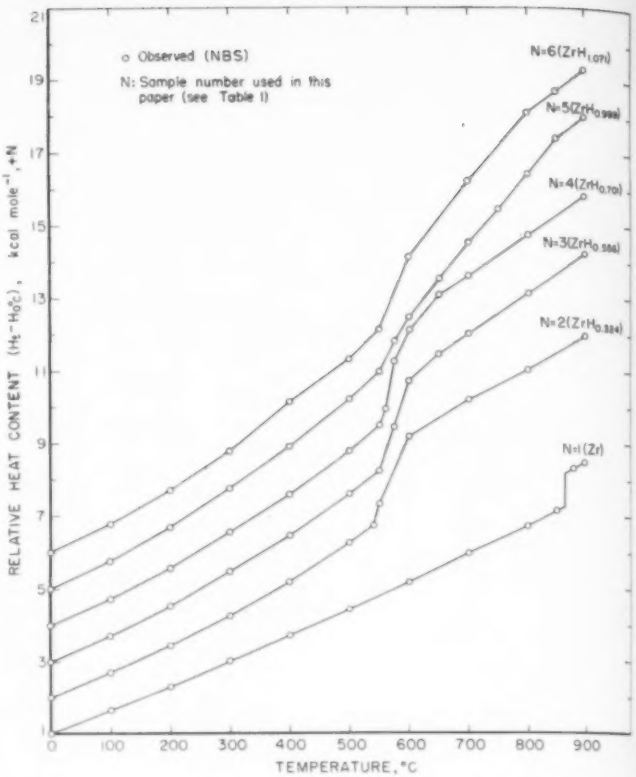

FIGURE 2. *Heat content versus temperature, zirconium and several zirconium hydrides.*

With due consideration to those few cases where phase equilibrium was obviously not reached during the measurements of heat content, it is possible to derive numerous quantitative energy and phase relations in the zirconium-hydrogen system from the precise thermal data reported in this paper. Such derivations are described in detail in a current publication [2].

The zirconium metal and its analysis were received from the U. S. Department of the Interior, Bureau of Mines, Albany, Oregon, through the courtesy of M. L. Wright. Several members of the National Bureau of Standards staff performed valuable services during the work. J. K. Russell made a number of the heat-content measurements on two of the hydride samples. Martha Darr carried out all the spectrochemical analyses of the Sylvania hydride samples, and R. A. Paulson analyzed the zirconium metal and duplicates of the Sylvania hydride samples for carbon and hydrogen.

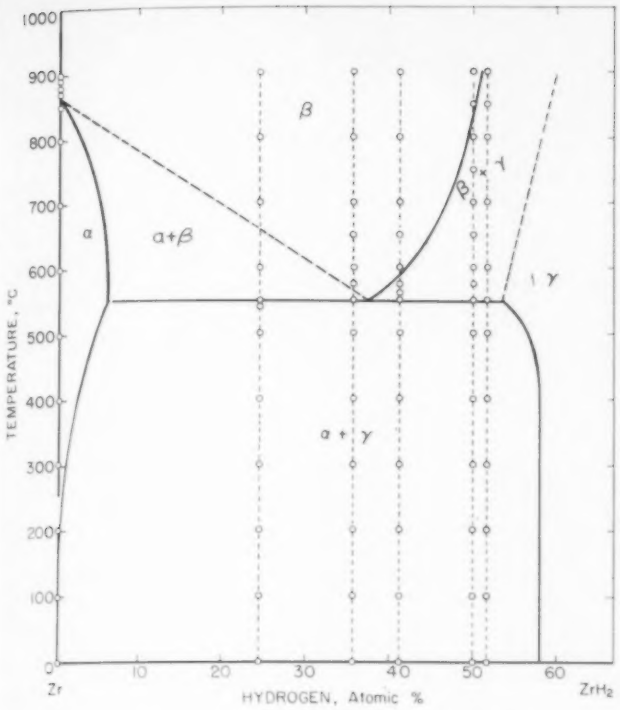

FIGURE 3. *Phase diagram of the* Zr-H *system.*

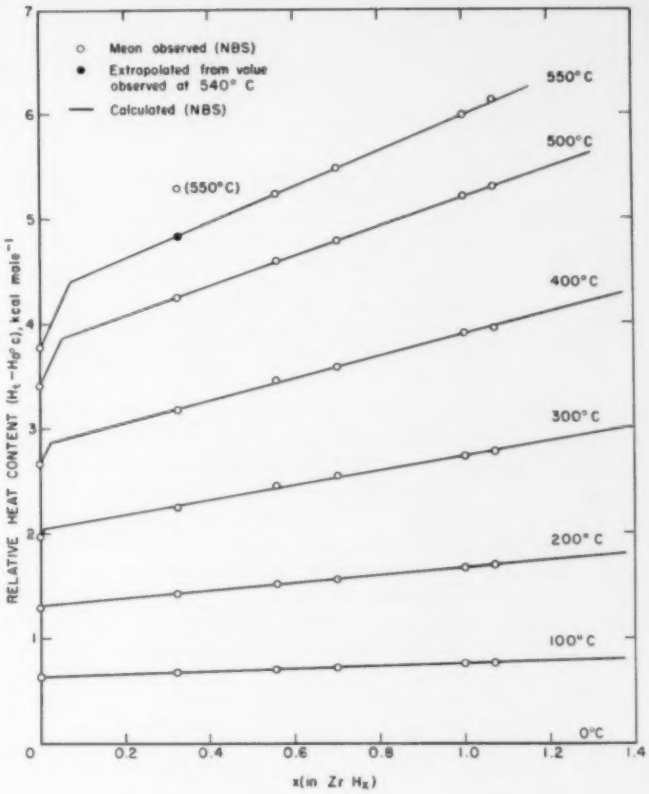

FIGURE 4. *Heat content versus composition of the* Zr-H *system, 0° to 550° C.*

6. References

[1] G. T. Furukawa, T. B. Douglas, R. E. McCoskey, and D. C. Ginnings, J. Research NBS **57,** 67 (1956) RP2694.

[2] T. B. Douglas, J. Am. Chem. Soc. (in press).

[3] W. G. Mixter and E. S. Dana, Ann. Chem. Pharm. **169,** 388 (1873).

[4] F. M. Jaeger and W. A. Veenstra, Rec. trav. chim. **53,** 917 (1934).

[5] J. P. Coughlin and E. G. King, J. Am. Chem. Soc. **72,** 2262 (1950).

[6] G. B. Skinner, Thermodynamic and structural properties of zirconium (Ph. D. dissertation, Ohio State Univ., Columbus, Ohio, 1951).

[7] R. F. Redmond and J. Lones, Enthalpies and heat capacities of stainless steel (316), zirconium, and lithium at elevated temperatures, Report ORNL–1342 (Oak Ridge National Lab., Oak Ridge, Tenn., 1952).

[8] J. L. Scott, A calorimetric investigation of zirconium, titanium, and zirconium alloys from 60 to 960° C, Report ORNL–2328 (Oak Ridge National Lab., Oak Ridge, Tenn., 1957).

[9] K. K. Kelley, Contributions to the data on theoretical metallurgy—X: High-temperature heat-content, heat-capacity, and entropy data for inorganic compounds, U. S. Bureau of Mines Bulletin 476, p. 205 (U. S. Government Printing Office, Washington, D. C., 1949).

[10] F. D. Rossini, D. D. Wagman, W. H. Evans, S. Levine, and I. Jaffe, Selected values of chemical thermodynamic properties, NBS Circ. 500, p. 718, (U. S. Government Printing Office, Washington, D. C., 1952).

[11] G. L. Miller, Metallurgy of the rarer metals—No. 2: Zirconium (Butterworths Scientific Publications, London, 1954).

[12] G. B. Skinner, C. W. Beckett, and H. L. Johnston, Thermal, structural, electrical, magnetic and other physical properties of Ti, Zr, Hf and Th and some of their simple compounds—II: Zr, its hydrides, oxides, halides, nitride, carbide, and the alkaline earth zirconates, Technical Report No 102–AC49/2–100–2 (Air Materiel Command, Wright-Patterson Air Force Base, Dayton, Ohio, 1950).

[13] D. A. Vaughan and J. R. Bridge, J. Metals **8,** 528 (1956).

WASHINGTON, December 20, 1957.

Journal of Research of the National Bureau of Standards Vol. 61, No. 1, July 1958 Research Paper 2879

Uniform Transient Error [1]

Edith L. R. Corliss

The economy of transient error is discussed. Equations describing error in power-level measurements of transients can be used to compute the design of analyzers so as to distribute transient error in a way compatible with experimental requirements. In addition, consideration of a limiting power-discrimination factor provides a measure of the largest number of bandpass filters that can be overlapped on adjacent channels to yield meaningful information about a rapidly changing signal. A scanning filter can be compared with a set of bandpass filters by calculating the effective number of overlapped bandpass filters providing the same resolution as the scanning filter. The results are applicable to autocorrelation analyzers. Restrictions on rapid signal analysis also are considered for the special case in which power-level discrimination is limited by noise.

1. Introduction

Measuring systems are limited by natural laws, and several of these guarantee that errors are inevitable. However, the distribution of errors can be controlled by the experimenter. One can choose experimental conditions that minimize errors in a region of particular interest; one can choose alternatively to spread the errors out as thinly as possible.

The transient properties of a measuring system become dominant whenever there is a restriction in time. The constraint may arise either because a signal is to be analyzed by a rapid process or because a signal may be changing rapidly in time.

In order to minimize transient error, experimental conditions must be chosen on a quantitative basis. Some prior knowledge of the signal to be analyzed is required. For the purpose of choosing the conditions of measurement, the problem of analysis can be restated as follows: Given an ensemble of signals characterized by a range of fluctuations in power over a range of intervals in time, one certain signal is to be distinguished from all other signals in the group.

A signal is discrete in time. The fluctuations in power during the existence of the signal convey its identity. If the power-level fluctuations are to be indicated within a certain degree of error, the time required for the analyzer to build up to within a corresponding fraction of its steady-state value must not exceed the shortest time interval over which a significant fluctuation of power level occurs in the component of the signal being analyzed. Thus, the rate at which the indication can build up or decay in the analyzer must exceed a limiting value. It is useful to describe this rate by reference to the response time of the analyzer, i. e., the time required to reach substantially steady-state indication after an abrupt change in signal.

Regardless of whether a frequency or a time-correlation analysis of the signal is undertaken, the results are observed as output power levels. Hence the ability to resolve a change in power level limits the discrimination that can be achieved for changes in frequency or intervals of time. The relation between the various limitations on the performance of an analyzer can be illustrated by means of a three-dimensional system (see fig. 1) in which the Cartesian coordinates are frequency, time, and either power or a function of power. The transient error then becomes a least volume in this space, within which no information about the signal can be found. The size of this least volume is limited by the natural behavior of analyzers, but its shape can be distorted to suit the needs of the experimenter.

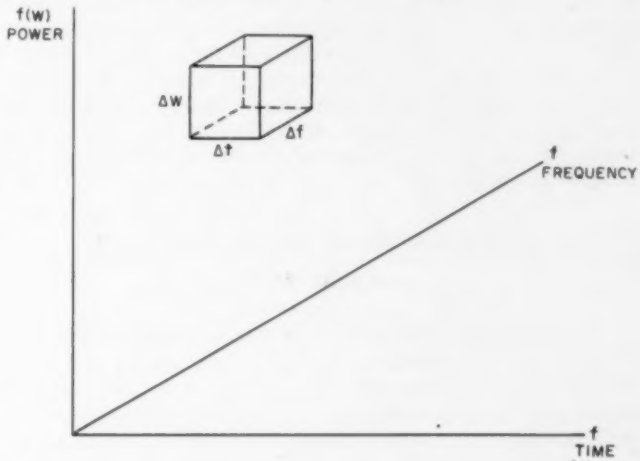

FIGURE 1. *Three-dimensional signal space.*

Resolutions in frequency and time are implicit in the Q (figure of merit) [2] of a frequency analyzer or, correspondingly, in the integration time of a correlation analyzer. To minimize the errors in an analysis, either Q or the integration time must be kept as high as possible consistent with the necessary resolution in power level.

Consider the rate at which power builds up in a linear series-resonant system, in a simple filter or a galvanometer. A family of indicial response curves for such a system is shown in figure 2, in which the coordinates have been scaled to relative values. The amplitude response has been scaled with the steady-state value as a unit; unity on the time scale is the natural, undamped period of the system. Curves in the family are plotted for different values of Q.

[1] This work was carried out as part of a program of basic instrumentation research and development cooperatively supported by Office of Naval Research, Atomic Energy Commission, Air Force Office of Scientific Research, and the National Bureau of Standards.

[2] The ratio of the energy-storage capacity of a resonating system to its energy-dissipation rate is known as its "figure of merit", or Q.

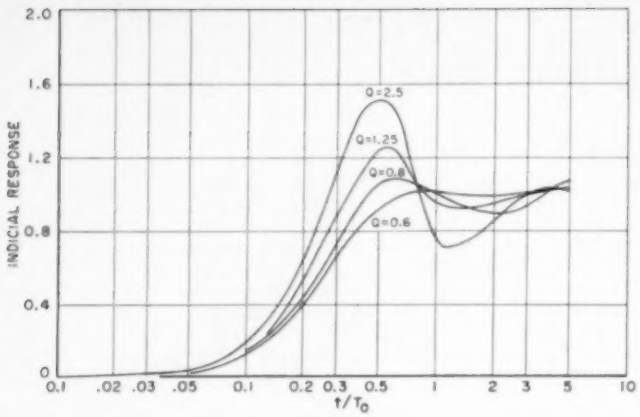

FIGURE 2. *Indicial response of a series-resonant system subjected to a step function.*

This shows the fraction of steady-state response attained as a function of the time following the impulse, scaled in units of the natural period of the system.

The analyzer may be considered to have reached a sufficient fraction of steady-state indication when it is just capable of resolving all unlike signals, whereas all like signals are indicated as being the same. Attempts either to speed up the response or increase selectivity are obtained at the expense of decreased Q or increased response time, without providing any additional information about the signal. Lengthening the response time, moreover, impairs the ability of the analyzer to indicate rapid power fluctuations, so that some features of the signal can be lost in this way.

2. Transient Limitations of a Simple Analyzer

The quantitative extent to which power-level resolution affects resolution along the coordinates of frequency and time can be found from the natural properties of the analyzer. The discussion to follow will be based on the common type of system whose behavior is described by a second-degree differential equation with constant coefficients, but its application to other systems will be indicated.

For example, consider the use of a linear series-resonant system as a tuned filter to indicate how a particular component of a complex signal fluctuates with time. If x represents amplitude, the transient response of the filter in terms of its center frequency, f_0, and figure of merit Q, is

$$x=e^{-\pi f_0 t/Q}\left(x_1 e^{j2\pi\sqrt{f_0^2-(f_0^2/4Q^2)}\,t}+x_2 e^{-j2\pi\sqrt{f_0^2-(f_0^2/4Q^2)}\,t}\right). \quad (1)$$

Let the observation interval, $\Delta\tau$, be sufficiently long compared with T_0, the undamped natural period of the filter, so that only the envelope of its response need be considered.

The analyzer should be able to change its indication by at least the smallest detectable power increment during a specified time after onset or removal of the input signal. The power built up in the filter is proportional to $|x|^2$. If W_0 is the initial power in the filter, at any time after cessation of the signal the power W_t is given by

$$W_t=W_0 e^{-\frac{2\pi f_0}{Q}t}=W_0 e^{-\frac{2\pi}{Q}\frac{t}{T_0}}.$$

Let $\Delta W=(1-e^{-\alpha})W$ be the smallest discernible change of power level in the filter; i. e., the power must decay by a factor $e^{-\alpha}$ for a change to be observed. If signal cessation is to be discerned within time

$$W_0-W_{\Delta\tau}=W_0(1-e^{-\frac{2\pi}{Q}\frac{\Delta\tau}{T_0}})\geq(1-e^{-\alpha})W_0,$$

so that

$$e^{-\left(\frac{2\pi}{Q}\frac{\Delta\tau}{T}\right)}\leq e^{-\alpha},$$

and the requirement is

$$Q\leq\frac{2\pi\Delta\tau}{\alpha T_0}=\frac{2\pi f_0\Delta\tau}{\alpha}, \quad (2)$$

if the filter is to indicate the occurrence of a change in signal during the interval $\Delta\tau$.

Equation (2) has been derived upon the basis of the finest resolution in power levels that can be achieved with the analyzer in the time interval $\Delta\tau$. Given that $\Delta\tau$ is the briefest duration of any signal component to be observed, eq (2) also shows how the Q of a filter must be adjusted as a function of its tuning in order to distribute the transient error uniformly over the frequency range. In addition, because eq (2) deals with limits of resolution, it provides a measure of the largest number of bandpass filters that can be overlapped on adjacent channels to yield meaningful information about a rapidly changing signal.

Over a range of frequencies $\Delta f=f_u-f_l$ surrounding f_o, the frequency to which the filter is tuned, the change in filter response does not exceed the smallest detectable power change. Consider the relative transmission characteristic of a filter having its Q given by eq (2) (see fig. 3). The relative power response of the filter is given by

$$W_f=\frac{W_0}{f^2/f_0^2+Q^2(1-f^2/f_0^2)^2}.$$

The precise result of solving for the discrimination limits in terms of f_u and f_l comes out as

$$\frac{f-f_l^2}{f_0^2}\geq\frac{\alpha}{\pi f_0\Delta\tau}\sqrt{(e^{\alpha}-1)+\frac{\alpha^2}{16\pi^2 f_0^2\Delta\tau^2}},$$

but if ΔW is small compared to W_o (i.e., fine-power discrimination can be made) then

$$f_u-f_l=\Delta f\geq\frac{\alpha^{3/2}}{2\pi\Delta\tau}.$$

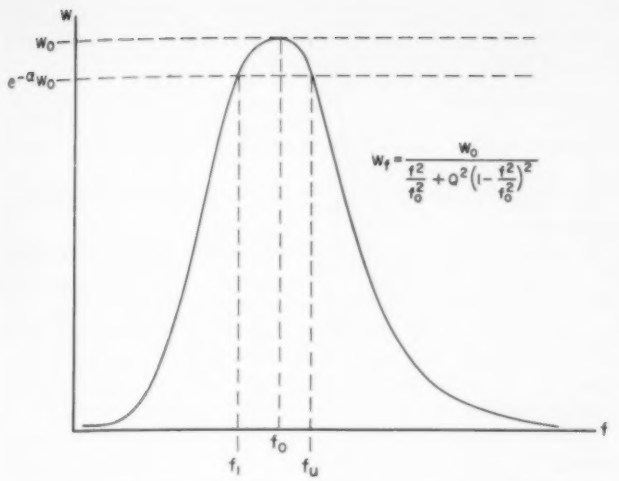

FIGURE 3. *Relative power response of a series-resonant system as a function of steady-state driving frequency.*

3. Analyzers Made Up of Overlapped Channels

For a set of filters overlapped at the limits of the power resolution, the limiting number of filters yielding meaningful information between f_l and f_b, the high- and low-frequency range limits, respectively, is given by

$$n_l - 1 \leq \frac{f_l - f_b}{f_u - f_l} = \frac{2\pi\Delta\tau}{\alpha^{3/2}}(f_l - f_b).$$

(The limits yield $n_l - 1$ rather than n_l because one-half of a filter extends beyond each end of the frequency range as defined here.)

In practice, it is usual to overlap adjacent filters at their half-power points, so that their integrated response has a flat characteristic. For this condition, $\Delta f = f_0/Q$, and the number of filters becomes

$$n_2 - 1 = \frac{f_l - f_b}{\Delta f} = \frac{Q(f_l - f_b)}{f_0} = \frac{2\pi\Delta\tau(f_l - f_b)}{\alpha}.$$

The ratio of this number to the maximum usable number of filters (overlapped at their limits of resolution) turns out to depend only on power resolution, i.e.,

$$\frac{n_2 - 1}{n_1 - 1} = \alpha^{1/2}.$$

If we are willing to take a "yes-no" type of analysis from the filter, then for a set of filters overlapped at their half-power points we can choose as a compatible condition that $\alpha = \ln 2$, i.e., the power declines at least to one-half its initial value during the observation interval $\Delta\tau$, and we get as the number of filters for this case:

$$n_b - 1 = \frac{2\pi\Delta\tau(f_l - f_b)}{\ln 2}.$$

Under these conditions, n_b invites comparison with the number of "bits" available in a given bandwidth during the time interval $\Delta\tau$.[3]

4. Scanning Analyzers

The process of scanning makes it possible to study the spectrum of a signal by means of a single channel in place of the numerous channels needed when fixed-bandpass filters are operated in parallel. When one scans by sweeping the tuning of a filter over the frequency range to be covered, the filter shows a rather complicated type of response.[4] However, one can make a quantitative study of the effects of scanning by use of simple theory, if one recognizes that another multiplicative factor will be necessary to take accurate account of the spreading of the filter's transient response due to the effects of scanning. The spreading occurs because the incoming signal beats with the ringing of the filter.

If one sweeps through a band of frequencies included between the limits f_t (high-frequency) and f_b (low-frequency) in the time interval τ, the length of time available to build up the power response of the filter at any instantaneous tuning is generally much smaller than the whole sweep interval. Call the observation interval for each effective single filter $\Delta\tau$, as for discussion of the fixed-bandpass filter. This quantity is directly related to the length of time that it takes the center tuning of the filter to change through a range of frequencies equal to the bandwidth between its half-power points. In this simplified discussion we shall take this relationship as unity, remembering that it is an approximation.

Various types of scanning functions can be used, depending upon the nature of the selectivity characteristic desired. If one wishes to have a constant Q (constant percentage bandwidth), the condition that the transient error is to be uniform throughout the range of frequencies swept over can be satisfied by scanning at a rate proportional to the square of the instantaneous center tuning of the filter. When one wishes to scan through the frequency range with a filter whose bandwidth is a constant number of cycles per second, so that the Q is directly proportional to the center tuning of the filter, the rate of sweep should be constant independent of frequency. One type of scanning filter sweeps logarithmically over its frequency range; when it is adjusted to uniform transient response, its instantaneous Q is proportional to the square root of its instantaneous tuning. Thus it is intermediate in its properties between constant-frequency bandwidth and constant-percentage bandwidth.

---

[3] R. V. L. Hartley, Transmission of information, Bell System Tech. J. **7**, 535 (1928).

[4] F. M. Lewis, Vibration during acceleration through a critical speed, Trans. Am. Soc. Mech. Engr. **54**, 253 (1932); G. Hok, Response of linear resonant system to excitation of a frequency varying linearly with time, J. Appl. Phy. **19**, 242 (1948); N. F. Barber and F. Ursell, The response of a resonant system to a gliding tone, Phil. Mag. **39**, 345 (1948); J. Marique, The response of RLC resonant circuits to EMF of sawtooth varying frequency, Proc. Inst. Radio Engrs. **40**, 945 (1952); M. C. Herrero, Resonance phenomena in time-varying circuits, Technical Report No. 69, (Electronics Research Laboratory, Stanford University, 1953); H. W. Batten, R. A. Jorgensen, A. B. MacNee, and W. W. Peterson, The response of a Panoramic Analyzer to CW and pulse signals, Proc. Inst. Radio Engrs. **42**, 948 (1954); S. S. L. Chang, On the filter problem of the power-spectrum analyzer, Proc. Inst. Radio Engrs. **42**, 1278 (1954).

The relations between Q and the sweep rate follow from the restrictions of eq (2) on minimum dwell time:

$$\Delta\tau=\frac{\alpha Q}{2\pi f_0}. \tag{3}$$

Describing the instantaneous scanning rate by the expression

$$h(f_0)df_0=dt,$$

an approximation to $\Delta\tau$ is obtained by integrating the scanning function between the half-power points of the filter. (To an approximation good to 12½ percent, even for Q as low as 1, the limits are $f_0 \pm f_0/2Q$.) Thus,

$$\Delta\tau=\int_{f_0-f_0/2Q}^{f_0+f_0/2Q} h(f_0)df_0.$$

Expanding this integral into Taylor's series:

$$\Delta\tau\cong\Theta(f_0)+f_0/2Q\Theta'(f_0)+\left(\frac{f_0}{2Q}\right)^2\frac{\Theta''(f_0)}{2}+$$

$$\left(\frac{f_0}{2Q}\right)^3\frac{\Theta'''(f_0)}{3!}+\cdots-\Theta(f_0)+\frac{f_0}{2Q}\Theta'(f_0)-$$

$$\left(\frac{f_0}{2Q}\right)^2\frac{\Theta''(f_0)}{2}+\left(\frac{f_0}{2Q}\right)^3\frac{\Theta'''(f_0)}{3!}+\cdots.$$

So that, to a close approximation:

$$\Delta\tau=\frac{f_0}{Q}\Theta'(f_0)+\frac{1}{3}\left(\frac{f_0}{2Q}\right)^3\Theta'''(f_0)+\cdots.$$

Looking back at the original integral, evidently

$$\Theta'=h(f_0)$$

and, substituting into the series

$$\Delta\tau=\frac{f_0}{Q}h(f_0)+\frac{1}{3}\left(\frac{f_0}{2Q}\right)^3h''(f_0)+\text{ higher terms.}$$

But, from eq (3)

$$\Delta\tau=\frac{\alpha Q}{2\pi f_0}=\frac{f_0}{Q}h(f_0)+\frac{1}{3}\left(\frac{f_0}{2Q}\right)^3h'''(f_0),\text{ etc.}$$

If Q is of moderate size or higher, then, very nearly

$$h(f_0)=\frac{\alpha}{2\pi}\frac{Q^2}{f_0^2}. \tag{4}$$

The precise way in which Q depends on the total scan time, the scanning function, and the total bandwidth covered can be obtained by substituting for eq (4) in the expression

$$h(f_0)df_0=dt.$$

Assigning the desired variation of Q with frequency, and integrating for the total scan time τ between the band limits f_b and f_t, we get

$$\tau=\int_{f_b}^{f_t}\frac{\alpha}{2\pi}\frac{Q^2}{f_0^2}df_0. \tag{5}$$

The magnitude of Q can be found by solving this equation.

Usually τ is the reciprocal of the repetition rate of the scanning filter. The value of α is a measure of the fineness of power-level discrimination that can be achieved. (Notice that eq (5) provides a means for assigning to α any desired dependence upon frequency, so that transient power discrimination can be distributed at will over the frequency range.)

The functioning of a scanning filter can be compared with a parallel channel set of bandpass filters by calculating the effective number of bandpass filters that will provide the same resolution as the scanning filter. The filters may be taken to be overlapped at their half-power points, and are calculated to cover the frequency range scanned with the same power-level resolution and figure of merit as those available from the scanning filter.

For a narrow frequency differential, df, in the tuning of the scanning filter, the "concentration" of filters in the range is given by

$$dn=\frac{df}{\Delta f},$$

where Δf is the width between the half-power points of the scanning filter at the instantaneous center frequency, f_0. The figure of merit, Q, is, of course $f_0/\Delta f$. Since one-half of a filter extends beyond each limit of the frequency range defined, integrating over the range gives one less than the equivalent number of parallel-channel filters that have their center tuning extending over the range, or

$$n_2-1=\int_{f_b}^{f_t}\frac{df}{\Delta f}=\int_{f_b}^{f_t}\frac{Q}{f_0}df.$$

5. Uniform Distribution of Transient Error

Table 1 summarizes the results of applying the foregoing discussion to calculate Q, the figure of merit, k, the scanning-rate parameter, and n_2, the equivalent number of filters overlapped at their half-power points, in terms of the scanning time, τ, the scanning bandwidth limits f_b and f_t, and the attenuation parameter, α. These calculations are based on uniform distribution of transient power-level discrimination, i. e., α is taken as a constant.

To facilitate adjustment of the response time of an analyzer to the least duration of any signal component to be observed, the tabulation also includes $\Delta\tau$ the observation time interval for any single filter.

Although the spreading due to ringing in the scanning filter is neglected, the relations shown in table 1 indicate quantitatively how the transient error and scanning characteristics affect the resolution of an

TABLE 1. *Relationships among variables describing the performance of scanning and fixed bandpass filters in which error in transient power-level discrimination is uniformly distributed*

Scanning rate	Q, Figure of merit for selectivity	(n_2-1), Number of filters overlapped at half-power points	K, Scanning parameter	$\Delta\tau$, Observation interval
No scan	$\leq\frac{2\pi f_0\Delta\tau_0}{\alpha}$	$\frac{2\pi\Delta\tau_0(f_t-f_b)}{\alpha}$	0	$\Delta\tau_0=\frac{\alpha Q}{2\pi f_0}$
Uniform scan, $df/dt=k$	$\leq\sqrt{\frac{2\pi\tau}{\alpha(f_t-f_b)}}f_0$	$\sqrt{\frac{2\pi\tau(f_t-f_b)}{\alpha}}$	$\frac{f_t-f_b}{\tau}$	$\frac{\alpha\tau}{2\pi(f_t-f_b)}$
Logarithmic scan, $df/dt=kf_0$	$\leq\sqrt{\frac{2\pi\tau}{\alpha\ln(f_t/f_b)}}\sqrt{f_0}$	$2\sqrt{\frac{2\pi\tau}{\alpha\ln(f_t/f_b)}}(\sqrt{f_t}-\sqrt{f_b})$	$\frac{\ln(f_t/f_b)}{\tau}$	$\frac{1}{\sqrt{f_0}}\sqrt{\frac{\alpha\tau}{2\pi\ln(f_t/f_b)}}$
Quadratic scan, $df/dt=kf_0^2$	$\leq\sqrt{\frac{2\pi\tau}{\alpha(1/f_b-1/f_t)}}$	$\sqrt{\frac{2\pi\tau}{\alpha(1/f_b-1/f_t)}}\ln\left(\frac{f_t}{f_b}\right)$	$\frac{1/f_b-1/f_t}{\tau}$	$\frac{1}{f_0}\sqrt{\frac{\alpha\tau}{2\pi(1/f_b-1/f_t)}}$

analyzer. The spreading due to ringing can be taken care of through the power-level resolution factor α.

As a numerical illustration of how the factors operate, consider what sort of analysis can be accomplished over the frequency range from 100 to 10,000 cps in 0.1 sec, if we are satisfied with a 10-percent power-level error.

From a bank of parallel bandpass filters, overlapped at their half-power points, you can get meaningful results from 6.26×10^4 filters, with a Q ranging from 6.28×10^2 at 100 cps to 6.28×10^4 at 10,000 cps.

If you scan uniformly at 10 sweeps/sec, the effective number of filters is markedly decreased because, of course, much less response time is available for each filter; in fact each filter must now respond with 90 percent of its final indication in about 4 msec. This sort of scan is equivalent to 252 filters, overlapped at their half-power points, and the available selectivity ranges from a Q of 2.52 at 100 cps to 252 at 10,000 cps.

A logarithmic scan, which allows somewhat longer dwell time at low frequencies, is equivalent to only somewhat fewer filters, 211 being the number under the conditions of the example given above. However, the Q at the low-frequency limit is 12.2, so that there has been some improvement in low-frequency resolution. This has been obtained at some loss in high-frequency selectivity; at 10,000 cps the Q is 122.

Where constant percentage bandwidth is desired, the scan rate is proportional to the square of the frequency. A correspondingly larger part of the time of observation is devoted to the low-frequency region. The limits converge on a Q of 25.2 independent of frequency, covering the range with 116 filters.

6. Limitation by Noise

The noise level associated with the signal provides a practical limit to the power-level resolution that can be obtained. Any further increase in resolution merely results in observing the noise, so that like signals may appear to differ.

An especially interesting expression results from considering the least power change observable to be limited by the noise present with the signal. If S is the signal power and N is the noise power, we take as a limit for detection

$$\Delta S\geq N.$$

Considered as a fractional power change,

$$\frac{\Delta S}{S+N}=\frac{W_0-W_t}{W_0}=1-e^{-\alpha}\geq\frac{N}{S+N}.$$

When $S/N\gg1$, $\alpha\rightarrow N/S$ and

$$\Delta f\Delta\tau\geq\frac{1}{2\pi}\left(\frac{S}{N}\right)^{-1} \tag{6}$$

and, correspondingly,

$$Q\leq\frac{2\pi\Delta\tau}{T_0}\left(\frac{S}{N}\right)=2\pi f_0\Delta\tau\left(\frac{S}{N}\right). \tag{7}$$

A higher Q can thus be used when there is a good signal-to-noise ratio. Equation (6) has a provocative resemblance to the Heisenberg uncertainty principle. The resemblance is real: both are derived by related mathematics, and both are based on the idea of a least discernible power change.

A special case of practical importance is the detection of a sinusoidal signal in the presence of "white noise." (Noise energy per unit bandwidth in cycles per second is constant.) For the filter calibrated at its peak response by means of a sinusoidal signal of power W_c, the same indication will be obtained with a white noise of E_f units per cycle per second, given by

$$E_f=\frac{QW_c}{\pi^2 f_0}.$$

This expression is obtained by integrating over the filter response.[5]

[5] D. Bierens de Haan, Nouvelles Tables D'Intégrales Définies, eq. 6, p. 47 (Edition 1867 reprinted 1939).

Detection of a sinusoidal signal of power S_0 (at the center frequency to which the filter is tuned) in the presence of a noise distribution of n_f units per cycle per second proves to require a least time interval $\Delta\tau_0$, which is independent of Q.

$$\Delta\tau_0 \geq \frac{\pi n_f}{2S_0}.$$

Narrowing the filter does decrease the amount of noise passed, but it lengthens the response time by a proportionate amount.

7. Transfer of Results to Correlation Techniques

The foregoing discussion of selectivity and response time can be transferred directly to the design of correlation analyzers. In a paper on synchronous detectors [6] Selgin derives a relationship between the integration time of a correlation analyzer and the Q of a filter exhibiting equal selectivity,

$$Q = \frac{\pi\tau}{T},$$

where T is the period of the synchronous detector and τ is the R–C integration time constant. This relation permits calculation of the transient error distribution in correlation analyzers from the results in this paper.

The author expresses appreciation to Chester H. Page, who provided much-needed advice on this work, and to whom the generalized mathematical treatment deriving the scanning function from an arbitrary Q is due.

WASHINGTON, July 26, 1956.

[6] Paul Selgin, Harmonic output of the synchronous rectifier, J. Research NBS 47, 427 (1951) RP2267.

Journal of Research of the National Bureau of Standards Vol. 61, No. 1, July 1958 Research Paper 2880

Optical T-Bench Method of Measuring Longitudinal Spherical Aberration

Francis E. Washer

A method of measuring longitudinal spherical and chromatic aberration by visual means is described. The method employs an especially constructed optical T-bench equipped with nodal slide and an angle-measuring telescope. The underlying theory of the method is presented, together with a brief description of the apparatus used. The results of measurement on a few typical lenses and an analysis of the sources of error are included.

1. Introduction

The determination of longitudinal spherical aberration is frequently required during the course of the measurement of the optical characteristics of photographic objectives. While many methods have been developed that are capable of yielding this information, it, nonetheless, seems worth while to describe a method that has been in use at the National Bureau of Standards since 1943. This is an indirect method, in that the lens is used to collimate the light from a point source located in the focal plane, and the angular deviations of adjacent beams from parallelism are measured. The determination of the longitudinal spherical aberration is based on the analysis of these angular deviations. At the time of inception it was necessary to develop a simple, rapid method of evaluating the longitudinal spherical aberration of reflector sight lenses.[1] In connection with the development of this rapid method, the present more accurate procedure was developed for the purpose of checking the results.

Early work was done with relatively simple apparatus that was rather unstable. The apparent worth of the method was, however, sufficiently high as to warrant the construction of new equipment in order that a higher degree of accuracy could be obtained. The resulting equipment consisting of the optical T-bench and a new nodal slide is shown in figures 3 and 4.

2. Theory of the Method

When a lens is affected with longitudinal spherical aberration, the effect can be described most simply by considering it as change in positions of the focal point for the various annular zones of the lens. For an ideal lens the focus is a point on the axis in the image space through which pass all rays of light that are initially parallel to the axis in the object space prior to incidence on the front surface of the lens. If the lens is reversed and a point source of light placed at the focus, the light incident on the back surface of the lens will emerge as a parallel beam of light concentric with the lens axis. This condition is shown schematically in figure 1, where

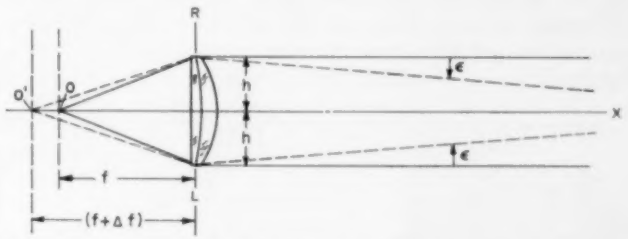

FIGURE 1. *Schematic drawing of a lens showing light incident on the lens from a point source on the axis at O.*

For O located at the focus, the emergent beam is parallel to the lens axis. When O moves by amount, Δf, to O′, the emergent beam is convergent, and a ray located at zone height, h, is deviated through the angle, ϵ.

light from the point source, O, is incident on the lens at height h and emerges parallel to the axis OX. Let the point source, O, be moved by amount Δf, to O′. If O′ is farther from the lens than O, the emergent beam is convergent. For a ray incident at height h, the emergent ray will deviate from parallelism with the axis by the angle ϵ. It can be shown that

$$\epsilon=\frac{\Delta f h}{f^2+f\Delta f}, \tag{1}$$

where f is the equivalent focal length of the lens. For known values of ϵ, the value of Δf can be determined to a close approximation from the relation

$$\Delta f=\frac{\epsilon f^2}{h}\left(1+\frac{\Delta f}{f}\right). \tag{2}$$

For Δf, very small compared with f, the above relation may be written

$$\Delta f=\frac{\epsilon}{h}f^2. \tag{3}$$

It is clear that only a 1-percent error is introduced into the determination of Δf for a value of $\Delta f=0.01f$. This can be further reduced by inserting the approximate value of Δf obtained from eq (3) into eq (2) and redetermining Δf. However, for most practical purposes the value of Δf computed from eq (3) is satisfactory.

If the lens shown in figure 1 is affected with longitudinal spherical aberration, rays of light from the point source at O incident on the lens at varying zone heights, h, will deviate from parallelism with the axis

[1] F. E. Washer, An instrument for measuring longitudinal spherical aberration of lenses, J. Research NBS **43**, 137 (1949) RP2015.

by varying amounts, ϵ. If the various values of ϵ are plotted as a function of h, a curve such as No. 1 in figure 2, A, will result. For this curve, the variation of ϵ with h, arises from a combination of two effects: (1) Out-of-focus effect, and (2) angular spherical aberration or parallax resulting from longitudinal spherical aberration of the lens. The two effects can be separated quite easily, as out-of-focus effect produces a variation of ϵ proportional to h, which plots as a straight line of constant slope passing through the zero point of the graph. This is shown by curve 3 in figure 2, A. The nonlinear portion of the curve arises from angular spherical aberration. On subtracting the abscissas of curve 3 from those of curve 1 for corresponding values of h, the resulting values of ϵ are those produced by the angular spherical aberration of the lens; this is shown as curve 2 in figure 2, A.

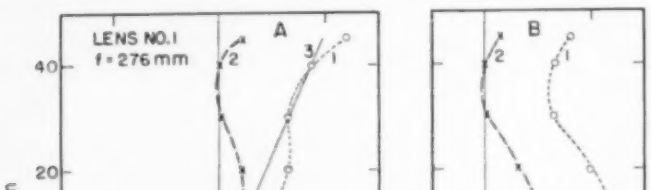

FIGURE 2. *Parallax angle ϵ versus h, and Δf versus h, for a typical lens.*

A. Curve 1 shows the variation of ϵ with h when the lens has longitudinal spherical aberration and the target is not at the position of best focus. Curve 3 shows the variation of ϵ arising from out-of-focus effect alone of Δf=0.67 mm. Curve 2 shows the angular spherical aberration alone (the difference between 1 and 3).

B. Curve 1 shows values of Δf computed before making the correction for out-of-focus effect. Curve 2 shows values of Δf after making correction for an out-of focus effect of 0.67 mm. Curve 2 is also the longitudinal spherical aberration plotted with respect to the plane of best focus for zone height, h=40mm.

When the value of f is known and the values of ϵ as a function of h have been measured for the condition of point source located on the lens axis and in the vicinity of the focal point, the values of Δf can be computed with the aid of eq (3). When the values of Δf are plotted as a function of h, the resulting curve shows the longitudinal spherical aberration. If the point source is not at the true focal point, the entire curve is displaced along the axis by an amount that is readily obtained from the graph or from the computed values of Δf.

In figure 2, B, curve 1 shows the values of Δf obtained using the same values of ϵ shown in curve 1 of figure 2, A. It is clear that the entire curve is displaced from the zero line of abscissas; this indicates that the target did not lie in the plane of best focus for any zone of the lens. When the adjusted values of ϵ (plotted as curve 2 in fig. 2, A) are used in determining the values of Δf, the result is as shown in curve 2 of figure 2, B; for this condition of focus, the target would lie in the focal plane of the zone for h=40 mm.

3. Method of Measurement

In order to measure the longitudinal spherical aberration of a lens by measuring the variations in parallax in the emergent beam, it is necessary to use equipment capable of making accurate measurements of parallax angle and zone radius h. The optical T-bench, shown in figure 3, was developed at this Bureau for use in making such measurements. It consists of two optical benches mounted at right angles to one another in the form of a T on a strong metal table. The lens under test is mounted on the nodal slide, as shown, with the target and illuminating system mounted on a separate bench slide as indicated. The viewing telescope is mounted on a movable slide located on the T-bench. The telescope is so arranged that its line of sight is approximately normal to the bench ways upon which its base slide can move. The pointing of the telescope is done with micrometers near the ocular end, which produce a small rotation about effective horizontal and vertical axes located in the flexure plate mounting near the objective end of the telescope. The change in pointing caused by a movement of the horizontal micrometer of one scale division is approximately 5.8 sec of arc. (The accurate calibration factor is 0.0283 milliradian per scale division.) In reading the micrometer, the value of the setting to the nearest one-tenth of a scale division can readily be made.

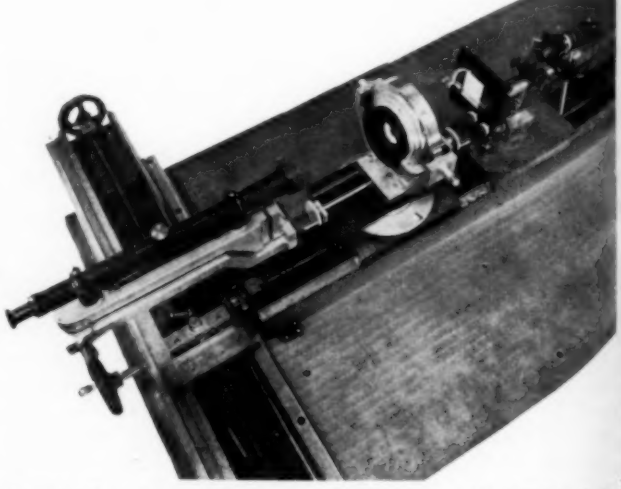

FIGURE 3. *Arrangement of apparatus on optical T-bench for determination of longitudinal spherical aberration.*

The lens under test is mounted in the nodal slide in the center of the picture. The target reticle and illuminating system are shown on the movable slide to the right of the nodal slide. The viewing telescope, equipped with diaphragm over the objective, is shown mounted on the transverse nodal slide in the left portion of the photograph.

In preparing to measure the longitudinal spherical aberration, the lens is so positioned on the nodal slide that its rear nodal point coincides with the axis of rotation of the nodal slide. The axis of the lens under test is brought into parallelism with the bench ways, and the illuminated target is placed at the rear focal point of the lens. The positioning of the target at the focal point of the lens is done with the aid of the viewing telescope, which is itself set at infinity focus. The level of lens axis, target, and center of the viewing telescope object are adjusted so that all lie in approximately the same plane, which is parallel to the plane defined by the surfaces of the two bench ways.

The telescope objective is now covered with a diaphragm having a small central aperture, which is centered with respect to the telescope objective. When an observer looks through the telescope, he sees the image of an illuminated target (either a cross or pinhole pattern) superimposed on the cross hairs in the ocular of the viewing telescope. When the telescope is moved transversely by moving the slide upon which it is mounted, the image of the reticle will either stay on the cross hairs of the ocular or move toward one side of the visual field or the other. In the event of movement of the image, it can be brought again into coincidence with the cross hairs by appropriate movement of the transverse micrometer. The angular movement thus noted is a measure of the change in direction of a small circular beam of light emergent from a given area of the lens under test from the direction of a similar beam from another given area of the lens and lying along the same diameter.

It is a simple matter to select a given size of diaphragm opening, small in comparison with the area of the lens under test, and to select a series of steps so that measurements of the deviation of these successive small emergent beams can be made for an entire diameter of the lens. If the lens has been properly focused, and the telescope so moves that it always remains parallel to itself, the angular deviations noted arise from parallax (or angular spherical aberration) in the lens under test. The bench ways are so made that the telescope does maintain this condition of remaining parallel to itself at the various positions so that possible errors from this source can be regarded as negligible.

The scale on the bench carrying the telescope is used in making the successive settings at selected intervals. These settings are recorded, and the difference of successive bench scale readings from that one in the central position is recorded as h, the zone height. The micrometer readings for the successive pointings are taken for each value of h, and their differences from that one in the central position are recorded as ϵ's. It is, of course, necessary to make a careful determination of the central position. This is usually done at the start of the experiment by noting the total range of transverse movement, throughout which the image of the illuminated target remains visible in the telescope ocular to the observer. These end points are noted, and a point midway between them is accepted as the center of coordinates.

Although it is believed that the possible deviations of the line of sight with movement of the telescope on its slide are negligible, it is presently the custom to avoid all possibility of error from this source by using an arrangement such as that shown in figure 4. Here the telescope slide remains fixed, and the scanning across the aperture of the lens under test is accomplished by moving a slide carrying an appropriately mounted pentaprism. The deviation of the beam of light by the pentaprism is not changed by small rotations of the pentaprism about its vertical axis, which might be caused by small rotations of the carrying slide as it moves along the bench ways.

It is clear, then, that with this arrangement of apparatus it is possible to measure the values of ϵ as a function of h in the emergent beam of collimated light from a lens. These values can be used to determine the values of the longitudinal spherical aberration with the aid of eq (3).

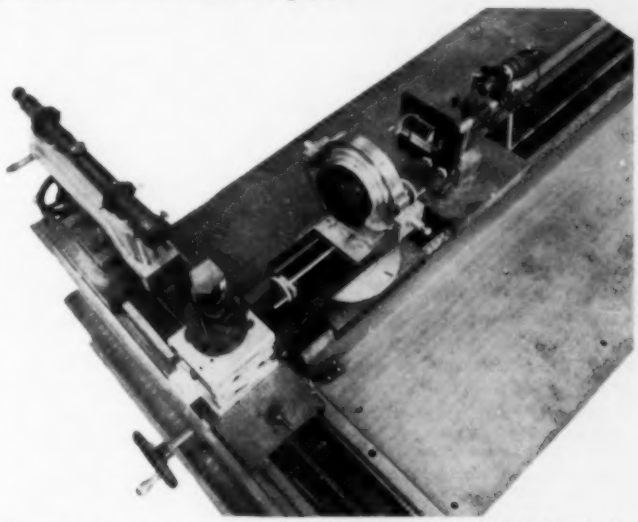

FIGURE 4. *Arrangement of apparatus on optical T-bench for determination of longitudinal spherical aberration.*

This arrangement differs from that shown in figure 3 in that a pentaprism has been placed on a movable slide on the transverse bench to eliminate transverse motion of the telescope.

4. Results of Measurement

This method of measuring longitudinal spherical aberration has been successfully used for several years at the Bureau for lenses having a wide range of focal lengths. In the succeeding sections, the results for a few typical lenses are given.

4.1. Photographic Objective Having a Focal Length of 150 Millimeters

a. Effect of Target Displacement Along Axis

Although there is no occasion to doubt the validity of the relations expressed in eq (1) and (3), it is nonetheless of interest to report the results of an experiment that confirms these relations and simultaneously puts to rest any lingering doubts concerning the proper sign of Δf. In addition, considerable

information is gained on the probable accuracy and limitations of this method of determining longitudinal spherical aberration.

The lens selected for measurement was a photographic objective, designated lens 2, having a nominal focal length of 6 in. and a maximum aperture of $f/6.3$. The measured value of the equivalent focal length was 152.4 mm, which means that the maximum value of h (the half-diameter of the aperture) was 12.1 mm. The arrangement of apparatus was as shown in figure 4. The diameter of the diaphragm opening placed over the telescope was 2.0 mm.

The viewing telescope was first focused for infinity for the condition of no diaphragm over its objective. The lens and target reticle were then accurately alined, so that the axis of the lens was parallel to the bench ways, and the center of the reticle was on the optical axis of the lens. The slide carrying the target system was moved along the bench until the reticle was in the plane of best focus of the lens under test as viewed through the telescope. The 2.0-mm diaphragm was then placed over the telescope and the center of coordinates determined. The results of measurement are shown in table 1 for five settings of the target. In this table, the target settings with respect to the lens bench scale are shown at the top; the highest numbers indicate the positions of the target nearest to the lens. The nominal values of Δf (hereafter designated δf to distinguish from the measured values of Δf), with respect to the plane of best focus, are shown on the next line of the table; these values are approximate as the bench scale is read with a vernier to the nearest tenth millimeter, and no attempt was made to make these settings to better than ± 0.1 mm. The left column shows the successive positions of the telescope (or pentaprism) on the transverse bench. The words, Left and Right, or L and R, are included in the tables to show that the measurements are initiated at the left-hand side of the lens as viewed by the observer and are made at the designated intervals with the pentaprism being moved toward the right throughout the course of the experiment. The positions where light is first seen to enter the telescope is designated first image, and the position where it just disappears as the slide moves along the bench is designated last image. No readings of the deviation ϵ are possible at these positions, but these points serve to locate the center of coordinates, which in this instance corresponds to the 40.2-mm setting. Observations of the deviation, ϵ, are made at 2-mm intervals along the transverse bench to a distance of 12 mm on each side of the central position. The values of the observed deviation are given in scale divisions for each of the five target settings. Each scale division is equivalent to 0.0283 milliradian deviation. Table 2 shows the values of h and ϵ with respect to the center of coordinates; this table is derived from table 1.

TABLE 1. *Variation of parallax angle, ϵ, with transverse setting of telescope for five positions of the target with respect to lens 2, which has a focal length of 152.4 mm*

The column headed $\delta f = 0.0$ corresponds to the position of best focus; negative values of δf indicate the target is farther from the lens.

Telescope positions on bench, mm	Target settings on lens bench, mm				
	90.1	90.6	91.1	91.6	92.1
	Nominal values of δf, mm				
	−1.0	−0.5	0.0	0.5	1.0
	Measured values of ϵ, in scale divisions				
Left					
[a] 25.3					
28.2	64.3	57.3	47.8	46.9	38.4
30.2	82.2	73.3	62.9	54.2	46.7
32.2	83.3	75.3	66.8	59.2	52.4
34.2	78.2	71.1	64.4	58.4	52.8
36.2	72.6	67.3	62.2	58.7	54.5
38.2	67.8	65.1	62.2	59.9	58.0
[c] *40.2*	*65.2*	*64.6*	*62.9*	*63.0*	*62.2*
42.2	63.5	64.2	64.7	65.4	66.6
44.2	58.7	61.9	64.1	66.5	68.7
46.2	53.5	57.9	62.6	66.7	70.1
48.2	47.4	53.8	60.9	66.7	72.2
50.2	45.8	54.3	62.3	68.8	76.2
52.2	52.1	60.8	68.9	76.6	84.1
[b] 55.1					
Right					

[a] First image.
[b] Last image.
[c] Center setting.

TABLE 2. *Variation of parallax angle, ϵ, as a function of zone height, h, for five positions of the target with respect to the position of best focus of lens 2*

This table is derived from table 1.

Zone height, h, mm	Nominal values of δf, mm				
	−1.0	−0.5	0.0	0.5	1.0
	Deviation ϵ from central position in scale divisions				
L					
[a] −14.9					
−12	−0.9	−7.3	−15.1	−16.1	−23.8
−10	17.0	8.7	0.0	−8.8	−15.5
−8	18.1	10.7	3.9	−3.8	−9.8
−6	13.0	6.5	1.5	−4.6	−9.4
−4	7.4	2.7	−0.7	−4.3	−7.7
−2	2.6	0.5	−.7	−3.1	−4.2
0	0.0	.0	0.0	0.0	0.0
2	−1.7	−.4	1.8	2.4	4.4
4	−6.5	−2.7	1.2	3.5	6.5
6	−11.7	−6.7	−0.3	3.7	7.9
8	−17.8	−10.8	−2.0	3.7	10.0
10	−19.4	−10.3	−0.6	5.8	14.0
12	−13.1	−3.8	6.0	13.6	21.9
[b] 14.9					
R					

[a] First image.
[b] Last image.

The variation of ϵ as a function of h and Δf for the conditions described in the preceding paragraph is shown graphically in figure 5. It is clear that curve 3 for $\Delta f = 0$ is a typical curve of angular spherical aberration, whereas the other four curves show the contribution of varying amounts of out-of-focus effect. Values of Δf for each value of h and ϵ for each target setting listed in table 2 were computed with the aid of eq (3), and the results are shown in table 3. These results are shown graphically in figure 6, *A*. It is evident that the successive Δf-versus-h curves are spaced along the axis of abscissas with separations closely approximating the

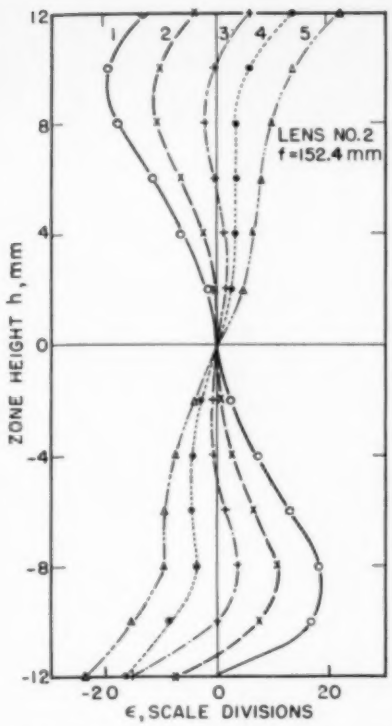

FIGURE 5. *Curves of parallax angle, ϵ, versus zone height, h, for lens 2 showing the effect of successive target displacements of approximately 0.5 mm along the axis.*

The results for a target position 1.0 mm farther from the lens than the plane of best focus are shown in curve 1. Curve 5 shows the results for a target position 1.0 mm nearer to the lens than the plane of best focus. Curves 2, 3, and 4 show the results for intermediate position (see tables 1 and 2).

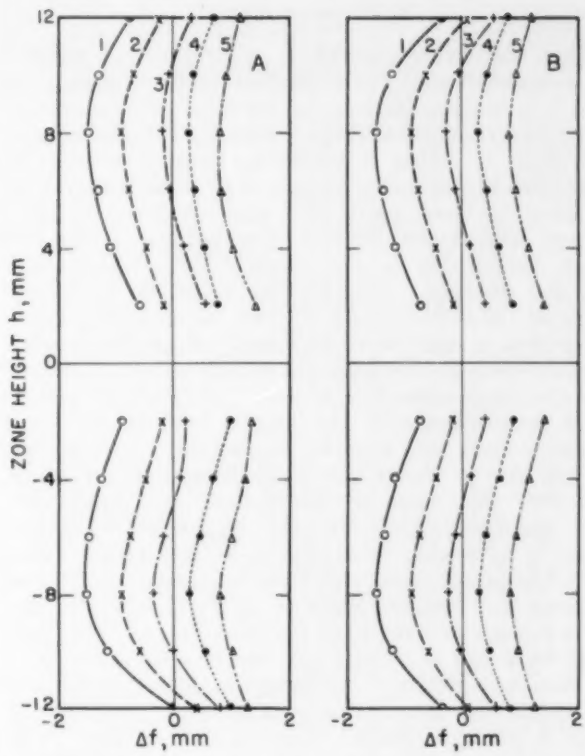

FIGURE 6. *Δf versus h curves for a series of target positions.*

A. Values of the displacement from best focus, Δf, as a function of zone height, h, for the conditions shown in figure 5 (see table 3).
B. Averaged values of Δf versus h, derived from part A (see table 4).

TABLE 3. *Computed values of Δf as a function of zone height, h, for five positions of the target with respect to the position of best focus for lens 2 (see tables 1 and 2)*

The value of focal length, f, is 152.4 mm. In converting ϵ in scale divisions to ϵ in milliradians, 1 scale division = 0.0283 milliradian.

Zone height, h, mm	Nominal values of δf, mm				
	−1.0	−0.5	0.0	0.5	1.0
	Computed values of Δf, mm				
L					
−12	0.05	0.40	0.83	0.88	1.30
−10	−1.12	−.57	.00	.58	1.02
−8	−1.49	−.88	−.32	.31	0.81
−6	−1.42	−.71	−.16	.50	1.03
−4	−1.22	−.44	.12	.71	.127
−2	−0.86	−.16	.23	1.02	1.38
0					
2	−0.56	−.13	.59	0.79	1.45
4	−1.07	−.44	.20	.58	1.07
6	−1.28	−.73	−.03	.41	0.87
8	−1.46	−.89	−.16	.30	.82
10	−1.28	−.68	−.04	.38	.92
12	−0.72	−.21	.33	.74	1.20
R					

TABLE 4. *Average values of Δf as a function of zone height, h, for five positions of the target with respect to the position of best focus for lens 2.*

These results are derived from table 3.

Zone height, h	Nominal values of δf, mm				
	−1.0	−0.5	0.0	0.5	1.0
	Average measured value of Δf, mm				
mm					
2	−0.71	−0.14	0.41	0.90	1.42
4	−1.14	−.44	.16	.64	1.17
6	−1.35	−.72	−.10	.46	0.95
8	−1.48	−.88	−.24	.30	.82
10	−1.20	−.62	−.02	.48	.97
12	−0.34	+.10	+.58	.81	1.25

nominal intervals separating successive positions of the target. The large negative values of Δf are associated with negative values of the nominal δf, so that eq (3) evidently gives the correct sign of the displacement with respect to the lens.

The curves shown in figure 6, A are not completely symmetrical about the axis but can be made so by averaging the values of Δf at corresponding values of $+h$ and $-h$. The resulting values of Δf given in table 4 are shown graphically in figure 6, *B*. The curve for nominal $\delta f = 0$ is the normal longitudinal spherical aberration curve for the lens with respect to the plane of best focus for a zone height, $h = 10$ mm.

b. Sources of Error

When the averaged values of Δf given in table 4 are compared with the initial values shown in table 3, it is clear that the departures of the individual values from the average value tend to vary somewhat with h. This is shown in table 5, where the departures of the initial values of Δf from the average are listed for each value of h and nominal δf. The average departures for the five values of nominal δf are also given in the table. It is noteworthy that the average variation for zones 4, 6, 8, and 10 are of the order of ± 0.05 mm, whereas the variation is ± 0.10 mm for zone 2 and ± 0.21 for zone 12. A small error in the location of the zero position of h on the transverse bench scale will produce appreciable asymmetries in the initial values of ϵ and Δf; the values will tend to be too high on one side and too low to about the same degree on the other. However, this type of error does not affect the final average value to an appreciable extent. Errors in Δf arising from errors in h are proportional to the fractional error in h; thus an error of ± 0.1 mm produces a 5-percent error in Δf for $h=2$ mm, but only a 1-percent error in Δf for $h=10$ mm. Similarly errors in ϵ are more serious for small values of h. For the case under consideration, an error in ϵ of ± 0.1 scale division produces an error of ± 0.03 mm in Δf for $h=2$ mm and an error of ± 0.01 mm in Δf for $h=6$ mm. The large errors at $h=12$ mm are caused by asymmetrical use of the 2-mm viewing aperture at the edge of the lens.

TABLE 5. *Departures of measured values of Δf at paired values of the zone height, h, from the average value of Δf for each value of h for five positions of the target with respect to the position of best focus.*

The average variation for each zone is also given. These results are for lens 2 and are derived from tables 3 and 4.

Zone height, h	Nominal values of δf, mm					
	−1.0	−0.5	0.0	0.5	1.0	Average departure
	Departures of initial values of Δf from average, mm					
mm						*mm*
2	±0.15	±0.02	±0.18	±0.12	±0.04	±0.10
4	.08	.00	.04	.07	.10	.06
6	.07	.01	.06	.04	.08	.05
8	.01	.00	.08	.01	.01	.02
10	.08	.05	.02	.10	.05	.06
12	.39	.30	.25	.07	.05	.21

It is of interest to compare the values of Δf obtained for each zone with each other and with the nominal vaues of δf through which the target is displaced. This comparison is given in table 6, where the difference in Δf for each zone from the value for $\Delta f=0$ is given. It is clear that the successive values compare quite favorably with each other for zones 2 through 10. It is, therefore, clear that quite reliable values of Δf are obtained by this procedure, and it appears probable that the values of the longitudinal spherical aberration so obtained are reliable to ± 0.04 mm for this particular lens.

TABLE 6. *Computed values of the separations of the target from the position of best focus for lens 2.*

These results are derived from table 4.

Zone height, h	Nominal values of δf, mm				
	−1.0	−0.5	0.0	0.5	1.0
	Average measured value of Δf, mm				
mm					
2	−1.12	−0.55	0.00	0.49	1.01
4	−1.30	−.60	.00	.48	1.01
6	−1.25	−.62	.00	.56	1.05
8	−1.24	−.64	.00	.54	1.06
10	−1.18	−.60	.00	.50	0.99
12	−0.92	−.48	.00	.23	.67
Average (2 through 10)	−1.22	−0.60	0.00	0.51	1.02

4.2. Longitudinal Chromatic Aberration of a Telescope Objective Having a Focal Length of 120 Millimeters

The axial longitudinal spherical aberration of a lens usually varies with the wavelength of the image-forming light. Thus if the longitudinal spherical aberration is measured for two different colors of light, the characteristic curves of Δf versus h will be displaced along the axis with respect to each other. The method of measurement described in section 4.1 provides a simple method of determining not only the longitudinal spherical aberration curve for a given color but also the displacement zone by zone for differing colors. To illustrate this, results of measurement are given for a lens, designated 3, having a focal length of 120 mm and a clear aperture of 40 mm.

The same procedure was followed as outlined in section 4.1 except that three successive runs were made. For each run, a different filter was placed between the light source and the target. In the present instance Wratten monochromatic filters 74 (green), 75 (blue green), and 70 (red) were used, and the results of measurement of parallax angle, ϵ, as a function of zone height, h, are shown in table 7. The variation of ϵ with h is shown graphically in figure 7, A for each of the three colors. The values of Δf computed for each value of h are likewise shown in table 7, and the averaged values of Δf for paired values of h are shown graphically in figure 7, B. The position of the target was left unchanged during the entire experiment, consequently the Δf-versus-h curves in figure 7, B, show both the longitudinal spherical aberration and the longitudinal chromatic aberration. It is noteworthy that the chromatic difference in focus between the light passed by filters 74 and 75 is negligibly small, whereas the difference for 74 and 70 is appreciable. Some out-of-focus effect is present, which shows that the target was approximately 0.27 mm farther from the lens than the position of best focus for filter 74. It can be inferred from the average values of Δf, shown in table 7, that the chromatic difference in focal length between the light passed by filters 74 and 75 is 0.03 mm and between filters 74 and 70 is 0.10 mm.

TABLE 7. *Variation of parallax angle, ϵ, and Δf as a function of zone height, h, for three colors (74 green, 75 blue green, and 70 red)*

The results are for lens 3, a telescope objective having a focal length of 120 mm.

Zone height, h	Filter number					
	74		75		70	
	ϵ, scale divisions	Δf	ϵ, scale divisions	Δf	ϵ, scale divisions	Δf
mm		*mm*		*mm*		*mm*
−20	15.3	−0.31	12.5	−0.26	15.9	−0.32
−16	11.9	−.30	9.7	−.25	9.0	−.23
−12	7.6	−.26	6.6	−.22	4.4	−.15
−8	4.8	−.24	4.1	−.21	2.4	−.12
−4	2.5	−.26	2.3	−.23	1.4	−.14
−2	1.2	−.24	1.1	−.22	0.6	−.12
0	0	------	0	------	0	------
2	−1.3	−.26	−1.3	−.26	−.5	−.10
4	−2.5	−.26	−2.5	−.26	−.9	−.09
8	−4.9	−.25	−4.9	−.25	−2.4	−.12
12	−7.7	−.26	−7.1	−.24	−4.8	−.16
16	−12.0	−.31	−11.0	−.28	−8.7	−.22
20	−16.4	−.33	−13.8	−.28	−13.1	−.27
Average..	------	−0.27	------	−0.24	------	−0.17

4.3. Telescope Objective Having a Focal Length of 167 Millimeters

In the course of making measurements on lenses of various types and focal lengths, one occasionally finds effects that are of unusual interest. The results of measurement of longitudinal spherical aberration on this lens are here included because of the unusual form of the longitudinal spherical aberration curve. The lens, designated 4, is a telescope objective having a focal length of 167 mm and a clear aperture of approximately 46 mm.

The test procedure was essentially the same as that described in section 4.2, except that only two filters, 74 and 70, were used. The data for filter 75 are omitted, as the results obtained with it are nearly identical with those for filter 74. The results of measurement of parallax angle, ϵ, as a function of zone height, h, are shown in table 8 and figure 8, A. The values of Δf were computed for each value of h and are shown in table 8. The averaged values of Δf for paired values of h are shown graphically in figure 8, B. The curves in figure 8, B show the longitudinal spherical aberration for each of two colors. It is noteworthy that the two curves are similar but are separated from each other by approximately 0.2 mm.

It is interesting to note the shape of the Δf versus h curves in figure 8, B. In the vicinity of the axis, the curves have a bulge toward the direction of shorter focal length. This anomaly does not occur in all lenses measured, but it does occur in enough to create a belief that this effect does not arise from experimental error. It is possible that it may result from a variation in the radius of curvature of one of the components of the lens under test.

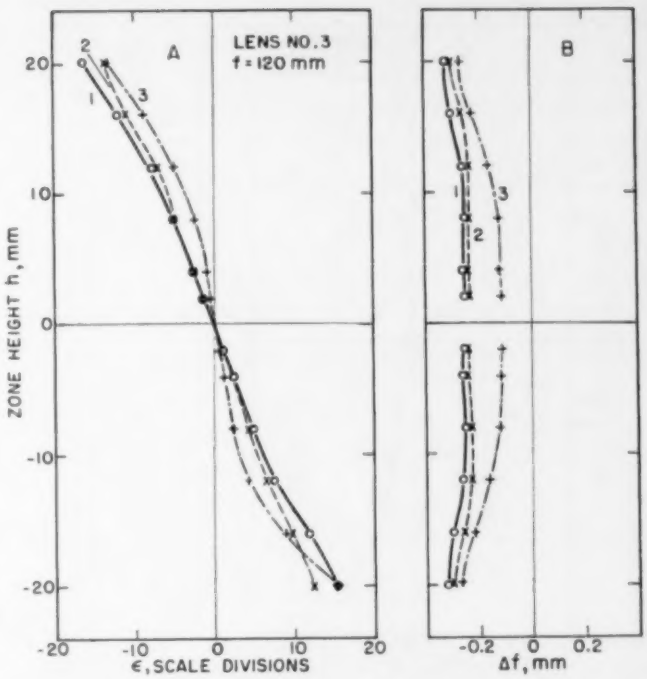

FIGURE 7. *Parallax angle ϵ versus h, and Δf versus h for three colors.*

A. The values of parallax angle ϵ, as a function of zone height h, are given in curves 1, 2, and 3, for Wratten filters 74 (green), 75 (blue green), and 70 (red), respectively.

B. Values of longitudinal chromatic and spherical aberration Δf derived from the measurements shown in part A (and table 7).

TABLE 8. *Variation of parallax angle, ϵ, and Δf as a function of zone height, h, for two colors (74 green and 70 red)*

The results are for lens 4, a telescope objective having a focal length of 166.7 mm.

Zone height, h	Filter number			
	74		70	
	ϵ, scale divisions	Δf	ϵ, scale divisions	Δf
mm		*mm*		*mm*
−23	12.2	−0.42	10.1	−0.34
−21.5	8.1	−.30	5.8	−.21
−20	5.6	−.22	2.7	−.11
−15	2.8	−.15	−1.4	+.07
−10	1.6	−.13	−2.2	.17
−7.5	1.3	−.14	−1.7	.18
−5	1.5	−.24	−0.9	.14
−2.5	0.8	−.25	−.4	.13
0	0	------	0	------
2.5	−.7	−.22	.2	.06
5	−1.3	−.20	.7	.11
7.5	−1.2	−.13	1.5	.16
10	−1.3	−.10	2.5	.20
15	−2.1	−.11	1.9	.10
20	−4.3	−.17	−2.2	−.09
21.5	−6.5	−.24	−4.8	−.18
23	−9.4	−.32	−7.2	+.25
Average..	------	−0.22	------	+0.01

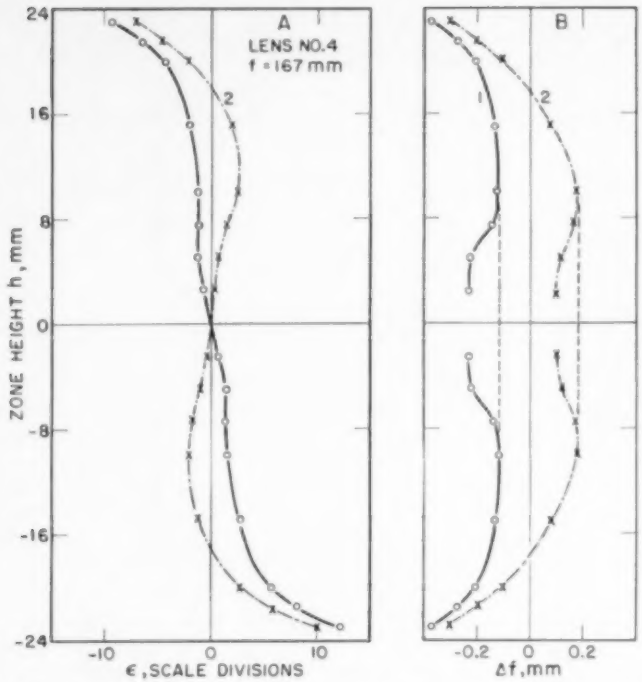

FIGURE 8. *Curves for a lens showing unusual characteristics of the longitudinal spherical aberration obtained for two colors.*

Curve 1 shows the results for Wratten No. 74 filter, and curve 2 shows the results for Wratten No. 70 filter. The curves appear to bulge in an unusual fashion away from the lens in the axial region (see table 8).

5. Sources of Error

In section 2, it is noted that an error in the location of the target reticle with respect to the focal point of the lens would produce an error in the measured values of the parallax angle, ϵ, and that this error would be propagated into the computation of those values of Δf from which the values of the longitudinal spherical aberration are derived. It is, however, a simple matter to so position the reticle that variations in the value of Δf from this cause are less than 1 percent and can be regarded as negligible. It is worthwhile to consider the magnitude of the errors induced in Δf by errors in the measured values of the zone height, h, and the parallax angle, ϵ. The effect of errors in h and ϵ are discussed briefly in section 4.1, b in connection with the measurements on a particular lens, but some additional comments are given in the following sections.

5.1. Effect of Error in the Values of h

There are two potential sources of error in the determination of the zone height, h. If the values of h are measured accurately but with respect to an incorrect zero position, the curve of ϵ versus h is not symmetric about the origin and creates the appearance of large error. This is particularly noticeable in the derived curve of Δf versus h, as it produces a very pronounced asymmetry. This error may be minimized or eliminated by averaging the values of Δf for corresponding values of $+h$ and $-h$. It is usually, however, more aesthetically satisfying to make a more accurate determination of the correct zero position and to make the computations with respect to this corrected position.

When the values of h are measured with respect to the correct zero position, then the values of Δf are affected by a given fractional error in h by approximately the same fractional error. Thus for a constant error in h, the fractional error increases with decreasing h and so places a lower limit on the value of h that may be profitably used. Assuming that h can be measured to the nearest ± 0.05 mm, the lowest value of h that can be used is ± 1.0 mm if one does not wish the error in Δf from this source to exceed 5 percent. For the same constant error in h, the error in Δf at $h = \pm 10$ mm is ± 0.5 percent, which may usually be regarded as negligible.

5.2. Effect of Errors in ϵ

The magnitude of the observed parallax angle, ϵ, is usually quite small, so that errors in ϵ provide the primary limitation in the determination of Δf. It is difficult to determine ϵ with an accuracy better than ± 0.5 sec because of limitations placed by pointing accuracy.[2] It is probable that determinations of ϵ can be made by using reasonable care, so that the error of the mean does not exceed ± 1.0 sec. For purposes of illustration, computations of the magnitude of the error in Δf caused by an error of ± 2.0 sec were made for a series of values of equivalent focal length, f, and the zone height, h, and the results are shown in table 9, A. In these computations, the equation

$$\Delta f = \epsilon \frac{f^2}{h} \tag{3}$$

was used, with value of ϵ maintained constant at ± 2 sec. Consideration of the values in part A of table 9 makes it clear that the magnitude of the error in Δf increases steadily with f for a fixed value of h, and inversely with h for a fixed value of f. For values of f above 100 mm, the errors in Δf become appreciable for the selected value of the error in ϵ. It is, therefore, interesting to consider these magnitudes of the error in Δf with the theoretical depth of focus, d_f, of a lens in the image space. Approximate values of d_f in millimeters are computed on the basis of the equation

$$d_f = \frac{4b}{R_m}, \tag{4}$$

where b is the f-number and R_m is the maximum theoretical resolving power for light having a wavelength of 575 mμ.[3] The value of R_m in lines per millimeter can be computed with the aid of the formula

$$R_m = \frac{1426}{b}. \tag{5}$$

[2] F. E. Washer, Effect of magnification on the precision of indoor telescope pointing, J. Research NBS **39**, 163 (1947) RP1820.

[3] F. E. Washer, Region of usable imagery in airplane-camera lenses, J. Research NBS **34**, 175 (1945) RP1636.

TABLE 9. *Effect of errors on the determination of longitudinal spherical aberration*

Comparison of the error produced in the determination of the longitudinal spherical aberration, Δf, by an error of ± 2 sec in the measured value of the parallax angle, ϵ, with the theoretical depth of focus in the image space, d_f, that yields maximum theoretical resolving power, R_m, for light having a wavelength of 575 mμ.

Values are given in millimeters for a series of values of equivalent focal length f, and zone height, h.

Zone height, h	A. Errors produced in the longitudinal spherical aberration, Δf, by an error of ± 2 seconds for various values of f				
	50	100	200	400	800
mm					
2.5	±0.010	±0.039	±0.155	±0.62	±2.49
5	.005	.019	.078	.31	1.24
10	.002	.010	.039	.16	0.62
20	--------	.005	.019	.08	.32
40	--------	--------	.010	.04	.16
	B. Values of theoretical total depth of focus, d_f, yielding a resolving power R_m for the following values of f				
	50	100	200	400	800
2.5	0.280	1.120	4.48	17.92	71.7
5	.070	.280	1.12	4.48	17.9
10	.018	.070	0.28	1.12	4.5
20	--------	.018	.07	0.28	1.1
40	--------	--------	.02	.07	0.3

It must be mentioned that values of d_f obtained with eq (4) are for an ideal lens; for an actual lens having aberrations the value of d_f may range from approximately $2.8b/R_m$ to $4b/R_m$.

To facilitate the computation of d_f, the values of the f-number, b, and the maximum theoretical resolving power are shown in table 10 for each value of the zone height, h, and equivalent focal length, f, shown in table 9, A. The values of d_f are computed with the aid of eq (4), and the resulting values are shown in part B of table 9 for ready comparison with the errors in Δf shown in part A of the same table. It is readily seen that the values of errors in Δf (or $\delta\Delta f$) are quite small in comparison with d_f for small values of h. The relation can be shown to be

$$\delta\Delta f = 0.014 h d_f, \tag{6}$$

indicating that the relative magnitude of $\delta\Delta f$ with respect to d_f is independent of the focal length, f, but does increase with increasing h. From these considerations, it is evident that although the error in Δf is large at small values of h, these large errors are small in comparison with the usable depth of focus, d_f. In addition, $\delta\Delta f$ becomes small with large values of h, thus compensating for the increase in relative magnitude of $\delta\Delta f$ with respect to d_f for large values of h.

TABLE 10. *Values of the f-number, b, and maximum theoretical values of the resolving power, R_m, used in computing the values of d_f shown in part B of table 9*

Zone height h	A. Values of f-number, b, corresponding to successive zones for the following values of f				
	50	100	200	400	800
mm					
2.5	10	20	40	80	160
5	5	10	20	40	80
10	2.5	5	10	20	40
20	--------	2.5	5	10	20
40	--------	--------	2.5	5	10
	B. Values of maximum theoretical resolving power, R_m, in lines per millimeter for $\lambda = 575$ mμ, for the following values of f				
	50	100	200	400	800
2.5	143	72	36	18	9
5	286	143	72	36	18
10	572	286	143	72	36
20	--------	572	286	143	72
40	--------	--------	572	286	143

6. Discussion

This method of measuring longitudinal spherical aberration and longitudinal chromatic aberration has been used at the Bureau for some time. It has been used for lenses having focal lengths ranging from 2 in. to 15 ft. and having apertures ranging from 0.5 in. to 12 in. It has an accuracy comparable to the Hartmann photographic test method.[4] It has the advantage of being a visual test method. It can, moreover, provide reasonably accurate values quickly and easily.

The author expresses his appreciation to other members of the staff of the National Bureau of Standards for assistance during this work. Some of the measurements were made by Walter R. Darling.

[4] J. Hartmann, Z. Instrumentenk. **24**, 1, 33, 97 (1904).

WASHINGTON, February 26, 1958.

Journal of Research of the National Bureau of Standards Vol. 61, No. 1, July 1958 Research Paper 2881

Mass Spectrometric Study of the Rate of Thermal Decomposition of Hydrazoic Acid

J. L. Franklin,[2] Vernon H. Dibeler, and Preston P. Morris, Jr.[3]

Hydrazoic acid vapor at low pressures (0.15 mm Hg or less), has been decomposed thermally and the rate of reaction studied mass spectrometrically at 265° to 325° C. Nitrogen and ammonia are the only reaction products, and no intermediates were observed. The disappearance of HN_3 is first order and the reaction occurs on the walls of the glass reaction vessel. The experimental activation energy is 31 kilocalories per mole. The activation energy for the reaction $HN_3 \rightarrow NH + N_2$ must be at least 39 kilocalories per mole.

1. Introduction

Recent studies [1,2] [4] of hydrazoic acid have shown that the heat of the reaction

$$HN_3 \rightarrow HN + N_2 \qquad (R1)$$

is 6 to 9 kcal/mole. However Franklin et al. [2] have pointed out, from considerations of spin-orbital correlations that this reaction cannot proceed to the $^3\Sigma^-$ ground state of NH and instead would have to go to the lowest singlet ($^1\Delta$) state of the radical. They estimated that this would be some 28 kcal/mole above the ground state, so that the activation energy for the decompositions would be about 37 kcal/mole.

For so weak a bond, one would expect the molecule to decompose readily and a measure of the activation energy for the thermal decomposition of hydrazoic acid should ordinarily correspond to the activation energy of reaction. However, Ramsperger [3] and Meyer and Schumacher [4] have shown that the decomposition of hydrazoic acid in glass occurs on the surface of the vessels and presumably is catalyzed by the glass wall. Consequently, in such a system the activation energy would at best set a lower limit to the activation energy for reaction 1. In spite of this limitation it was deemed worthwhile to study the kinetics of decomposition of HN_3 and this paper presents the results of this investigation.

2. Apparatus and Procedure

A gas analysis mass spectrometer, Consolidated Electrodynamics Corporation type 21–102, was used to observe the rate of decomposition of hydrazoic acid and the appearance of decomposition products. The all-glass sample introduction system and 2-liter sample reservoir was similar to that described by O'Neal and Wier [5] and used by them for obtaining mass spectra of high molecular weight hydrocarbons. The sample reservoir volume was enclosed in a well-insulated heating jacket and provided with thermocouples at several points. Isolation from the sample introduction manifold and the evacuating pumps was accomplished with a gallium-sealed, magnetically operated valve. The gallium valve, connecting tube, and the tube containing the effusive leak were wrapped with individually controlled heating tapes and with thermal lagging. Chromel-alumel thermocouples were provided at the valve, the leak, and at several intermediate points for temperature measurement. The maximum operating temperature was about 350° C. At 300° C, temperatures could be read and controlled with an uncertainty of about ±4° C.

Conventional mass spectrometric techniques were used for both chemical analysis and observation of the kinetics of decomposition. The sample reservoir also served as a reaction vessel. Prior to each run, it was thoroughly outgassed, usually overnight, at temperatures somewhat above the anticipated temperature range. At the start of a run and after a stable operating temperature was attained, neon was introduced into the reservoir to a nominal pressure of about 0.05 mm of mercury as measured by gas pipet. The mass range of 16 to 46 was scanned quickly to serve as a background. Then hydrazoic acid was added to a partial pressure of about 0.1 mm of mercury and the time of introduction was noted. In order to make initial observations as frequently as possible, only selected portions of the mass scale were scanned; e. g., m/e=16 to 20, 28 to 32, and 40 to 46. Each range uniformly required about 1 min to scan and the total lapsed time was noted at the start of each scan. Measurements were usually continued until the molecule ion of HN_3 (m/e=43) had decreased to about 1 percent of the original abundance. The electron energy was 70 v.

Hydrazoic acid was prepared from sodium azide and 60 to 80 percent sulfuric acid. Preparations were carried out in a vacuum and the HN_3 was purified by simple bulb-to-bulb distillation and by pumping on the product held at liquid nitrogen temperature. A mass spectrometric analysis of the product showed no impurities of higher molecular weight or of most simple gases condensible at liquid nitrogen temperature, the exception being occasional small amounts of ammonia. For reasons of safety the quantity of stored hydrazoic acid was limited to that giving a pressure less than 50 mm of mercury at room temperature in a 2-liter bulb. As HN_3 was observed to decompose slowly in storage under these conditions, periodic analyses were necessary to assure material of suitable purity.

[1] This research was performed in part under the National Bureau of Standards Free Radicals Research Program, supported by the Department of the Army.
[2] Guest scientist on leave from the Humble Oil Co., Baytown, Tex.
[3] Present address, Convair, San Diego, Calif.
[4] Figures in brackets indicate the literature references at the end of this paper.

3. Results

Table 1 summarizes the experimental data. Hydrazoic acid and neon concentrations after various reaction times are given in all runs. The nitrogen and ammonia concentrations are given for purposes of illustration only for run 6. The only products of the decomposition of hydrazoic acid that were observed were ammonia and nitrogen. Although both hydrogen and hydrazine might have been expected none was ever found. Data from a typical experiment are plotted in figure 1. Here peak heights are corrected for differences in sensitivity and the mass 28 peak is corrected for the contribution from HN_3. The curves for ammonia and nitrogen are characteristic of those for primary products of reaction formed simultaneously from the initial reactant.

It is shown later that the decomposition of hydrazoic acid is kinetically first order. For this to occur with ammonia as the final product, at least one transient intermediate is required. This might include NH or electronically excited HN_3, as the first active species and various secondary intermediates such as N_2H_2, NH_2, etc., can be postulated. Most mechanisms for the decomposition of HN_3 have postulated NH as the initial product and we thought it worthwhile to try to establish this by identifying the products of its reaction with other materials. Specifically we made experiments in which large excesses of benzene and toluene were added to the reaction mixture and the products analyzed for postulated products of reaction. Thus, if NH were present, one might expect either biphenyl or aniline from the reaction in the presence of benzene, but none was identified, although the reaction in solution gives aniline. Similarly, in the presence of toluene one would expect bibenzyl, benzyl amine or dibenzyl amine to be produced but none was ever found. Rice and Freamo [6] report that cyanic acid was formed when CO was added to HN_3 at high temperatures but the identity of masses of HNCO and HN_3 rendered this method of identification unsuitable to our studies which depended upon mass spectra for identification and analysis of the reaction products. Similar considerations prevented our using ethylene which might have been expected to add NH giving ethylene imine.

Each mass spectrum was also examined carefully for evidence of transient intermediates but none was ever found. Of course NH would be obscured by the NH^+ peak from HN_3. However, N_2H_2 and N_2H_4 if present would have been strong evidence for the presence of NH and NH_2, respectively. In two or three runs small peaks at $m/e=30$ and 32 were found. However they always occurred together and no peak at $m/e=31$ was ever observed. Therefore it was concluded that the $m/e=32$ peak was due to O_2 introduced as an impurity and the $m/e=30$ peak was NO formed by reaction O_2 with either N_2 or HN_3. Thus it was impossible to obtain any direct evidence as to the nature of the active intermediates involved in the reaction.

Although the reaction appeared to be kinetically first order, it might conceivably have involved a self-regenerating chain process. Accordingly a few percent of NO was added in one of the runs to ascertain whether the rate of reaction was markedly reduced thereby. It is evident from table 1 that NO caused only a small reduction in rate. This reduction may be enough to indicate that free radicals are involved in the reaction and are partly removed by the NO. This very small reduction in rate, however, clearly implies that a chain reaction is not being interrupted.

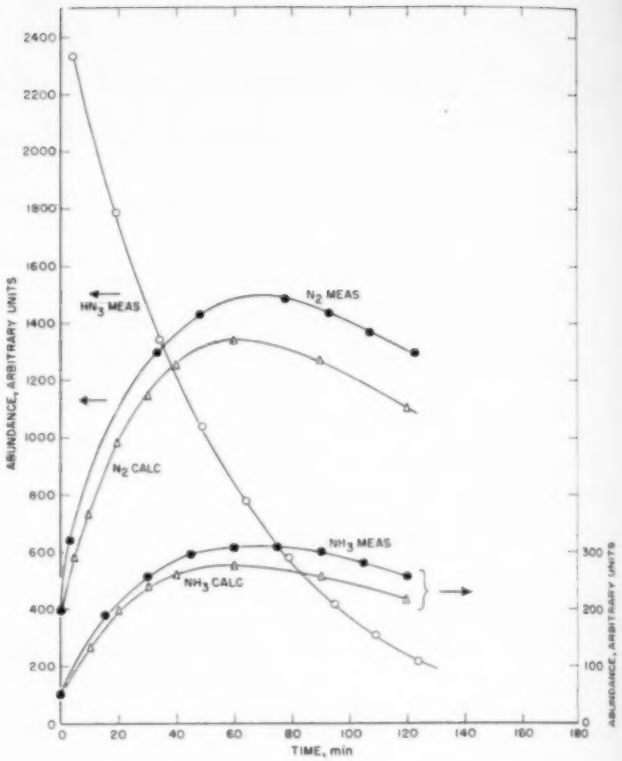

FIGURE 1. *Variation of concentrations with time for run 6.*

4. Kinetics

The gases in the reaction vessel passed into the mass spectrometer by molecular flow, the rate for various components of the gas mixture being inversely proportional to the square root of the mass. In all runs except one, neon was mixed with the hydrazoic acid in the reactor and the rate of disappearance of the neon, as indicated by the peak at $m/e=20$, was employed to calibrate the rate of flow of other components into the mass spectrometer. The rate of flow of neon from the reactor should be proportional to the neon concentration so that

$$\ln \frac{[Ne_0]}{[Ne]}=k_1 t \qquad (1)$$

where k_1 is the rate constant in reciprocal seconds. Data from a typical run plotted in figure 2 bear this out.

TABLE 1. *Summary of experimental data*

(Peak heights (PH) are given in arbitrary units.)

Run	2	3	4	5
Temperature, °C	325	300	275	275
Initial presence:				
HN_3, mm Hg	0.025	0.047	0.085	0.150
Ne, mm Hg	0.063	0.150	0.060	0.140

HN_3		Ne		HN_3		Ne		HN_3		Ne		HN_3		Ne	
t	PH	t	PH	t	PH	t	PH	t	PH	t	PH	t	PH	t	PH
min		*min*		*min*		*min*		*min*		*min*		*min*		*min*	
0	----	----	----	0	1740	----	----	0	2700	----	750	0	5800	0	----
7	87	3	390	4	1140	2	2085	3	1954	1	725	4	5440	2	1884
23	6	18	285	18.5	645	17	1800	19	1593	17	637	19	3934	17	1524
37	1	33	249	34	365	31.5	1545	34	1290	32	505	34	2980	32	1254
52	0.3	48	240	49	189	47	1320	49	993	47	476	49	2301	47	1047
----	----	73	210	64	90	62	1110	64	729	62	411	64	1773	62	882
----	----	----	----	80	41	78	940	79	531	77	353	79	1353	77	713
----	----	----	----	94	21.5	92	790	94	386	92	298	94	1017	92	589
----	----	----	----	116	8.5	113	620	108	281	106	253	109	755	107	449
----	----	----	----	146	3.5	143	430	124	138	121	183	141	409	139	336

k_e(Ne)sec^{-1}	1.5×10^{-4}	1.82×10^{-4}	1.67×10^{-4}	2.17×10^{-4}
$k_e+k_e(HN_3)sec^{-1}$	28.0×10^{-4}	7.7×10^{-4}	3.41×10^{-4}	3.11×10^{-4}
$k_e sec^{-1}$	27.0×10^{-4}	6.44×10^{-4}	2.27×10^{-4}	1.65×10^{-4}

Run	6	7	[a] 9
Temperature, °C	275	300	300
Initial presence:			
HN_3, mm Hg	0.075	0.080	0.090
Ne, mm Hg	0.160	0.100	0.040

HN_3		Ne		N_2		NH_3		HN_3		Ne		HN_3		Ne	
t	PH	t	PH	t	PH	t	PH	t	PH	t	PH	t	PH	t	PH
min		*min*		*min*		*min*		*min*		*min*		*min*		*min*	
0	2650	0	----	0	400	0	50	0	2230	0	1900	0	2300	0	----
4	2334	2	2067	3	640	----	----	4	1461	2	1674	5	1875	1	640
19	1785	17	1809	18	1040	15	190	19	768	17	1440	20	1176	16	623
34	1371	32	1557	33	1300	30	259	34	401	32	1215	35	702	31	585
49	1041	47	1347	48	1430	45	295	49	190	47	990	50	445	46	563
64	777	62	1149	63	1500	60	307	64	91	62	800	65	277	61	525
79	581	77	952	78	1480	75	310	79	41	77	663	80	163	76	498
94	419	92	805	93	1430	90	301	94	19	92	530	95	93	91	471
109	308	107	699	108	1370	105	286	110	9	108	419	110	56	106	451
124	221	122	593	123	1295	120	269	----	----	----	----	125	31.5	121	419

k_e(Ne)	1.80×10^{-4}	2.32×10^{-4}	0.58×10^{-4}
$k_e+k_e(HN_3)$	3.29×10^{-4}	8.48×10^{-4}	5.73×10^{-4}
k_e	2.04×10^{-4}	6.89×10^{-4}	5.33×10^{-4}

Run	12	14	[b] 15
Temperature, °C	265	290	278
Initial presence:			
HN_3, mm Hg	0.010	0.015	0.020
NE, mm Hg	0.010	0.015	0.051

HN_3		Ne		HN_3		Ne		HN_3	
t	PH	t	PH	t	PH	t	PH	t	PH
min		*min*		*min*		*min*		*min*	
0	340	0	123	0	340	----	----------	0	----------
5	340	----	----------	4	315	0	129	4	735
16	282	10	97	12	270	8	111	15	633
29	240	25	81	17	240	12	103	25	495
39	210	35	74	22	215	18	98	35	343
55	177	50	69	31	185	27	89	50	184
69	153	65	64	41	155	37	81	65	101
79	140	75	60	51	134	47	76	-----	----------
89	124	85	55	64	113	57	71	-----	----------
104	108	100	51	76	78	72	63	-----	----------
114	96	110	47	91	64	87	57	-----	----------
152	63	148	40	106	50	102	53	-----	----------

k_e(Ne)	1.05×10^{-4}	1.2×10^{-4}	----------
$k_e+k_e(HN_3)$	1.84×10^{-4}	3.06×10^{-4}	----------
k_e	1.12×10^{-4}	2.25×10^{-4}	----------

[a] Contains about 0.5 percent of NO. [b] Reactor packed with glass wool.

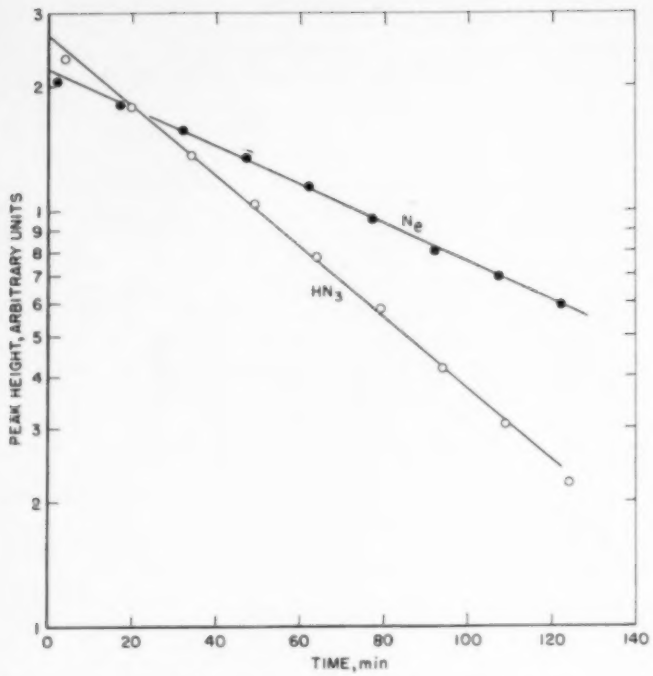

FIGURE 2. *Semi-log plot of concentration versus time for run 6. Observed rate constants are* $k_{N_2}=1.8\times10^{-4}$ *sec*$^{-1}$, *and* $k_{HN_3}=3.29\times10^{-4}$ *sec*$^{-1}$.

Hydrazoic acid will disappear from the reaction vessel by reaction and by flow into the ionization chamber. The rate of disappearance is

$$\frac{-d[HN_3]}{dt}=k_r[HN_3]^n+k_2[HN_3], \qquad (2)$$

where k_r and k_2 are respectively, the rate constant for reaction and for flow out of the reactor and n is the order of the reaction. From figure 2 it appears that $[HN_3]$ is an exponential function of time and that the reaction is first order i. e., $n=1$. However, since the over-all disappearance is influenced by the flow rate, which is first order, it seemed desirable to apply a more sensitive test of reaction order. For this the differential rate equation is more suitable than the integrated expression. Equation (2) can be rewritten

$$\frac{-d\ \ln\ [HN_3]}{dt}=k_r[HN_3]^{n-1}+k_2. \qquad (3)$$

By calculating the slopes of tangents to the curve of $[HN_3]$ versus time, such as that in figure 1, $d\ln[HN_3]/dt$ is readily calculated for various points along the curve. If this parameter varies with the concentration of HN_3 the order can be obtained graphically since k_2 is known. If $d\ln[HN_3]/dt$ is independent of the HN_3 concentration the reaction is first order. A typical set of results is given in table 2 and shows that within experimental accuracy $d\ln[HN_3]$ is independent of the HN_3 concentration and thus the reaction is indeed first order. Since $n=1$, (2) becomes $-d[HN_3]/dt=(k_r+k_2)[HN_3]$ and (k_r+k_2) can be determined from the slope of a plot of $\ln[HN_3]$ against t. Also $k_2=k_r\sqrt{M_2/M_1}$, where M is molecular weight, so k_r is determined. The rate constants for all runs were determined in this way and the results are given in table 1.

Ammonia and nitrogen are formed simultaneously by reaction and are withdrawn by effusion into the mass spectrometer. Since the total reaction is $3HN_3\rightarrow NH_3+4N_2$ we may write

$$\frac{d[NH_3]}{dt}=\frac{k_r}{3}[HN_3]-k_3[NH_3] \qquad (4)$$

$$\frac{d[N_2]}{dt}=\frac{4k_r}{3}[HN_3]-k_4[N_2] \qquad (5)$$

where k_3 and k_4 are, respectively, the rate constants for effusion of ammonia and nitrogen from the reactor. Integration leads to the following relations between concentrations and time:

$$[NH_3]=\frac{k_r\ [HN_3^\circ]}{3\,(k_r+k_2-k_3)}\{\exp\ (-k_3t)-\exp\ (-k_r-k_2)t\}+[NH_3^\circ]\ \exp\ (-k_3t) \qquad (6)$$

$$[N_2]=\frac{1.33k_r\ [HN_3^\circ]}{k_r+k_2-k_4}\{\exp\ (-k_4t)-\exp\ (-k_r-k_2)t\}+[N_2^\circ]\ \exp\ (-k_4t). \qquad (7)$$

Figure 1 gives typical curves of $[NH_3]$ and $[N_2]$ against time obtained experimentally and by calculation from eq (6) and (7). The agreement leaves something to be desired but is close enough to be considered as confirmation of the method.

TABLE 2. *Test of reaction order by differential rate equation for run 5*

t	$[HN_3]$	$-d[HN_3]/dt$	$-1000d\ [\ln HN_3]/dt$
Min			
20	3,800	70.0	18.43
30	3,200	60.0	18.73
40	2,600	52.5	20.2
50	2,150	40.0	18.6
60	1,800	32.5	18.1
70	1,500	26.3	17.6
80	1,275	21.3	16.7
90	1,075	18.7	17.4
100	900	15.0	16.7
110	750	13.8	18.4
120	625	11.2	17.9
130	525	10.0	19.1

5. Activation Energy

An Arrhenius-type plot of reaction rate constant versus temperature is given in figure 3. The data, although somewhat scattered, define a reasonably good straight line from which the activation energy $E\ddagger$, is found to be 31 kcal/mole. The rate constant is thus

$$k=4.5\times10^8\ \exp\ (-31000/RT)\ \text{sec}^{-1}. \qquad (8)$$

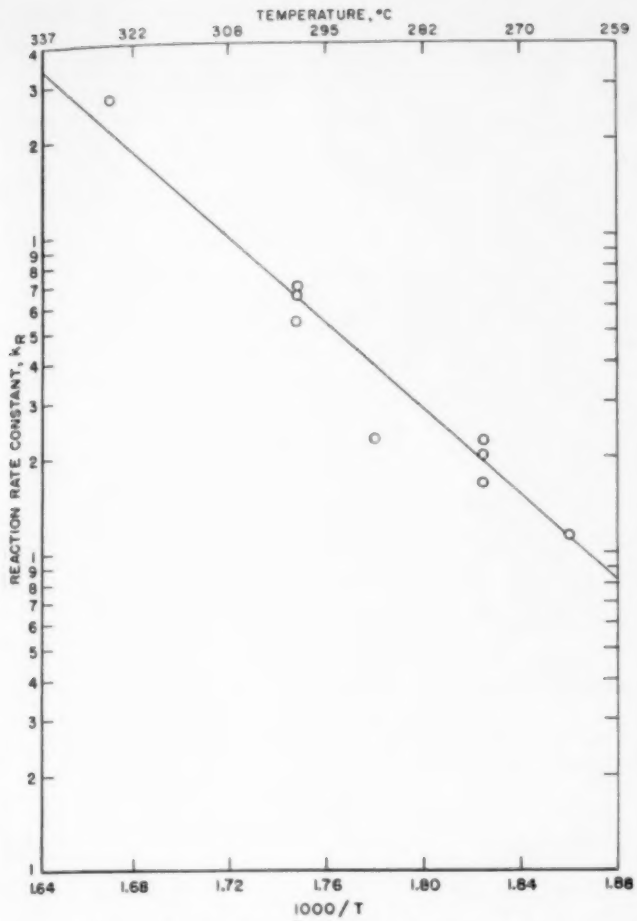

FIGURE 3. *Arrhenius plot of activation energy.*

Rice and Freamo [7] decomposed HN_3 thermally at 1,000° C and allowed the gases to impinge on a cold surface, thereby obtaining a characteristic blue solid. By varying the distance from the furnace to the cold surface they obtained a half-life of about 10^{-3} seconds for the active species which formed the blue solid and which they concluded was NH. Their results might also be explained as giving the half-life of HN_3 which decomposes to an active intermediate (such as NH) of very short life. If we calculate the half-life of HN_3 at 1,000° C from eq (8) we obtain a value of 3×10^{-4} sec which, in view of the fact that the two sets of measurements were made under very widely differing conditions, is a reasonable check on the results of Rice and Freamo [7].

Glasstone, Laidler, and Eyring [8] show that the rate constant may be expressed in terms of the experimental activation energy

$$k=\frac{kT}{h}\exp\left(2+\frac{S^{\ddagger}}{R}-\frac{E^{\ddagger}}{RT}\right). \qquad (9)$$

For reasons that will be given later (see eq 10, 11, and 12) the right-hand side of eq (9) must be multiplied by 3 to give the over-all rate constant. Taking $E^{\ddagger}=31$ kcal/mole and employing eq (8) and (9) we calculate $\Delta S^{\ddagger}$ to be -26 e. u. This is much too large a negative entropy for a gas phase, first order reaction. The value is best explained as resulting from a reaction occurring on a solid surface. Indeed, such an entropy value corresponds approximately to the entropy of condensation of a gas.

In order to corroborate this conclusion a run was made using a reactor packed loosely with glass wool. The results are not as satisfactory as those obtained with an unpacked reactor, probably because diffusion was impeded by the packing. However, they do show that the added surface greatly increased the reaction rate. We may conclude, therefore, that the reaction occurs predominately on the glass surface of the reaction vessel.

Since the reaction is kinetically first order and the surface is involved, two kinds of mechanism can be adduced which would be in accord with our observations.

1. HN_3 is adsorbed reversibly and the surface is sparsely covered. The adsorbed material undergoes a series of reactions resulting eventually in the production of nitrogen and ammonia which are desorbed. The following mechanism is one of several possibilities of this kind

$$\left.\begin{aligned} &HN_3(g) \overset{a}{\leftrightarrows} HN_3\ (ads)\\ &HN_3(ads) \overset{b}{\rightarrow} HN\ (ads)+N_2(g)\\ &HN(ads)+HN_3(ads)\overset{c}{\rightarrow}N_2H_2\ (ads)+N_2(g)\\ &N_2H_2(ads)+HN_3(ads) \overset{d}{\rightarrow} NH_3(g)+2N_2(g) \end{aligned}\right\} \qquad (R2)$$

If one assumes that reaction b is the slow, rate-controlling step and employs a steady-state treatment for all transient species the following rate expression is obtained:

$$\frac{-d[HN_3(g)]}{dt}=3k_b\,K_{ads}\,[HN_3(g)] \qquad (10)$$

where K is the equilibrium constant for the adsorption of hydrazoic acid on glass.

2. HN_3 reacts in the gas phase to give an active species which adsorbs rapidly and then undergoes a series of reactions with gaseous HN_3. It is assumed that the surface is almost completely covered by the active species. As an example

$$HN_3(g) \rightarrow NH(g)+N_2(g) \qquad (R1)$$

$$\left.\begin{aligned} &HN(g) \leftrightarrows NH(ads)\\ &HN(ads)+HN_3(g) \rightarrow N_2H_2(ads)+N_2(g)\\ &N_2H_2(ads)+HN_3(g) \rightarrow NH_3(g)+N_2(g) \end{aligned}\right\} \qquad (R3)$$

Again, if one assumes the first reaction to be the slow, rate controlling step and applies a steady-state treatment, the reaction rate is found to be

$$\frac{-d[HN_3(g)]}{dt}=3k_1\,[HN_3(g)] \qquad (11)$$

Both kinds of mechanisms give first order kinetics for the decomposition of HN_3, but the over-all rate constant for mechanisms of type 1 includes the adsorption equilibrium constant whereas those of type 2 do not.

Mechanisms of type 2 usually prevail for the recombination of atoms or simple radicals where a third body is required to remove the energy of reaction. It seems unlikely that this should be the case here since various reactions of the probable intermediates other than simple recombination can readily be visualized and these would provide a means of removing excess energy without the need of a third body or wall. Further, the rate of disappearance of HN_3 by this mechanism is given simply by $3k_1$ and so is independent of surface effects. This would not account for the negative entropy of activation and so mechanisms of this kind can be discarded.

Since the rate constant for mechanism 1 includes the equilibrium constant for adsorption of HN_3 on glass, we may write

$$k_{expt}=3k_bK=\frac{3kT}{h}\exp\left(\frac{\Delta S^{\ddagger}}{R}-\frac{\Delta H^{\ddagger}}{RT}-\frac{\Delta H_{ads}}{RT}+\frac{\Delta S_{ads}}{R}\right)$$
$$=\frac{3kT}{h}\exp\left(\frac{\Delta S^{\ddagger}+\Delta S_{ads}}{R}\right)\exp\left(\frac{-\Delta H^{\ddagger}-\Delta H_{ads}}{RT}\right). \qquad (12)$$

$\Delta S\ddagger$ for a unimolecular reaction is usually small and, as a first approximation may be taken as zero. The entropy of adsorption is negative and is often comparable in magnitude to that obtained for $\Delta S^{\ddagger}$ in these studies.

In deriving eq (10) and (12) we assumed that the adsorption of HN_3 was reversible and that equilibrium existed at all times between HN_3 in the gas and on the surface. At equilibrium, $\Delta F=O$ and so

$$\Delta H_{ads}=T\Delta S_{ads}$$

The heat of adsorption then, at temperatures near 300° C would be about 8 kcal/mole. Since

$$E^{\ddagger}_{expt}=\Delta H^{\ddagger}_b+\Delta H_{ads}$$

$$\Delta H^{\ddagger}_b=39 \text{ kcal/mole.}$$

The activation energy, $\Delta H^{\ddagger}_b$ is, of course, the activation energy of reaction b, the slow step in the process. In the example given this is shown as a bond breaking reaction but it might also be a simple elevation of the molecule to a higher electronic state. Since reaction b occurs on the surface, $\Delta H^{\ddagger}$ is not necessarily the same as it would be for the gas phase reaction. Further, it is probably somewhat smaller that it would be for the gas phase process, since otherwise, in view of the small entropy of activation of a first order reaction in the gas phase, the reaction would occur in the gas and not on the surface. Also, if the rate controlling step is some reaction other than the simple bond breaking process shown in the example then it follows that the activation energy for the gas phase reaction

$$HN_3 \rightarrow NH+N_2 \qquad (R1)$$

is greater than $\Delta H^{\ddagger}$ since otherwise the latter reaction would occur at a greater rate and would be the process observed. It follows therefore that the measured $\Delta H^{\ddagger}$ is equal to or less than the heat of activation of reaction R1; i. e., $\Delta H^{\ddagger}$ for R1 is at least 39 kcal/mole. This is surprisingly close to the value of 37 kcal/mole estimated by Franklin et al.[2] It would appear from these data that the true value of the activation energy of R1 is somewhat greater than this, but the amount would be difficult to estimate.

6. References

[1] P. Gray and T. C. Waddington, Proc. Roy. Soc. [A] **235,** 481 (1956).
[2] J. L. Franklin, V. H. Dibeler, R. M. Reese, and M. Krauss, J. Am. Chem. Soc. **80,** 298 (1958).
[3] H. C. Ramsperger, J. Am. Chem. Soc. **51,** 2134 (1929).
[4] R. Meyer and H. J. Schumacher, Z. Physik. Chem. [A] **170,** 33 (1934).
[5] M. J. O'Neal, Jr., and T. P. Wier, Jr., Anal. Chem. **23,** 830 (1951).
[6] F. O. Rice and M. Freamo, J. Am. Chem. Soc. **75,** 548 (1953).
[7] F. O. Rice and M. Freamo, J. Am. Chem. Soc. **73,** 5529 (1951).
[8] S. Glasstone, K. J. Laidler, and H. Eyring, The Theory of Rate Processes, p. 397 (McGraw-Hill Book Co., Inc., New York, N. Y., 1941).

Washington, January 22, 1958.

Journal of Research of the National Bureau of Standards Vol. 61, No. 1, July 1958 Research Paper 2882

Erosion Damage to Solids Caused by High-Speed Collision With Rain*

Olive G. Engel

The stresses that are produced when a liquid drop collides with the planar surface of a solid are discussed. These are a result of the impact pressure and the consequent radial flow of the drop. It is concluded that a rain-erosion resistant material may be either soft and rubbery or hard and rigid. If it is soft and rubbery it mitigates the applied stresses but it must be able to withstand the mitigated stresses. If it is hard and rigid it does not mitigate the applied stresses and it must be able to withstand the unmitigated stresses.

1. Introduction

The problem of the erosion damage that is produced on objects that fly at high speed into rain has become increasingly more serious as flight velocities have been increased.

During the past 10 years, a program of testing has been carried out to find materials that will resist the stresses that are brought to bear in high-speed collision with rain. The work has been done mainly at the Cornell Aeronautical Laboratory. Specimens of materials have been fastened to the ends of a propeller and have been rotated at velocities up to approximately 600 miles per hour (mph) through artificial rain. Tests of a different kind have been carried out at higher velocities by the Convair Division of General Dynamics Corporation.

During the past 5 years, research has been in progress at the National Bureau of Standards to determine the mechanism of the erosion process.

A previous publication [1] has presented three factors that are important in analyzing the damage that is produced as a result of high-speed waterdrop collision with poly(methyl methacrylate): (a) The waterdrop behaves like a hard sphere or pellet in that it produces a cup-shaped cavity in the plastic; (b) although materials do not usually fail under uniform compression, a local compression can produce tensile stresses that result in failure; and (c) in the case of projectiles that flow as a result of the collision, the solid plastic can be damaged by the stresses exerted by the flowing projectile against surface irregularities that are restrained by the underlying layers of material.

2. Collisions of Waterdrops with Aluminum

Further evidence of the behavior of water under impact conditions was obtained in a study of the damage marks left by deforming lead pellets, steel spheres, and waterdrops as a result of high speed collision with soft 1100 aluminum sheet. Figure 1, A shows an example of a damage mark made by a $\frac{7}{32}$-in.-diam steel sphere on $\frac{1}{8}$-in. 1100–H14 aluminum sheet. This particular damage mark was obtained at a relative impingement velocity of 228 feet per second (fps). The diameter of this damage mark, as measured directly on the aluminum plate with a steel rule and magnifying glass, is about $\frac{1}{32}$ in., which is considerably less than the diameter of the steel sphere. Figure 1, B shows an example of a damage mark that was made by a 0.22-in.-diam deforming lead pellet on $\frac{1}{8}$-in. 1100–H14 aluminum sheet. This particular damage mark was obtained at a relative impingement velocity of 609 fps.

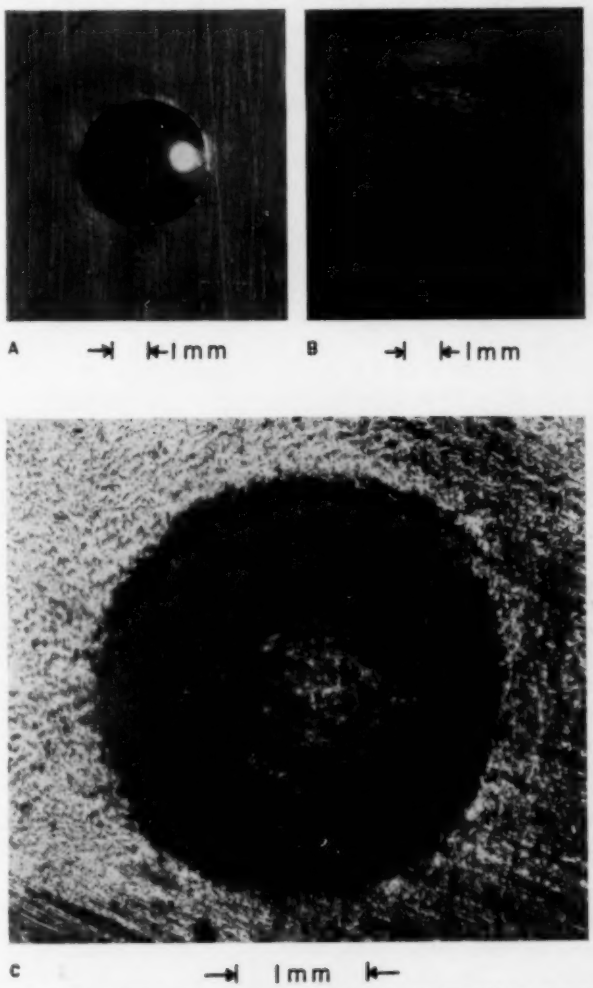

FIGURE 1. *Damage pits in 1100 aluminum formed as a result of collisions with (a) a steel sphere at a velocity of 228 fps, (b) a lead pellet at a velocity of 609 fps, and (c) a waterdrop at a velocity of 2,500 fps.*

*The work described in this paper was sponsored by the Wright Air Development Center. The material presented here has been taken largely from reports submitted to them. Their assistance and interest are gratefully acknowledged.

[1] Olive Engel, J. Research NBS **54**, 51 (1955) RP2565.

At a collision velocity of 880 fps (600 mph), waterdrop damage marks that have been observed in 1100–O aluminum resemble the mark left in 1100–H14 aluminum by impingement of a deforming lead pellet at very low velocity. When a waterdrop collides with 1100 aluminum at about 2,000 fps, an impression is made which resembles that made by a low-velocity steel sphere more nearly than that made by a relatively low-velocity lead pellet (see fig. 1). These observations lead to the conclusion that in the range of collision velocity up to about 1,000 fps a waterdrop behaves like a projectile that flows as a result of the collision, but at collision velocities of the order of 2,000 fps a waterdrop behaves very much like a projectile that does not flow as a result of the collision.

3. Destructive Action of the Radial Flow of a Waterdrop

When a waterdrop collides with the planar surface of a solid, or when the planar surface of a solid runs into a stationary waterdrop, the impact pressure that results reaches a high value in a very short time.[2] This high pressure drives the liquid that is close to the solid surface radially outward around a central stagnation point. The radially flowing liquid exerts a shear stress on the surface of the solid over which it is running. There is a shear stress between the separate layers of the flowing liquid itself, and it can be expected that a shear stress exists at the interface between the liquid and a solid surface over which it is moving. The shear stress, τ, between layers of liquid in laminar flow is given by the product of the viscosity, μ, and the velocity gradient through the moving sheet of liquid perpendicular to its direction of flow. That is, $\tau=\mu(\partial v/\partial z)$ where v is the velocity of the moving sheet of liquid and z is the direction through the thickness of the liquid sheet. The layer of liquid molecules in direct contact with the solid has zero velocity, but the velocity gradient is not zero and the shear stress is applied to the solid.

When a surface protrusion exists, the liquid from a drop that is flowing radially over it exerts forces against the protrusion acting in opposition to the cohesion of the protrusion to the underlying layers of material. Pressure, σ_p of figure 2, is exerted against the protrusion by the flowing liquid. The pressure that is exerted by the liquid tends to move the protrusion along the planar surface of the solid and results in a shear stress, τ' of figure 2, at the base of the protrusion. The flow of the liquid results in the shear stress, τ, that was discussed above. The pressure exerted by the liquid also results in a turning moment that tends to bend the protrusion over. The turning moment is the integrated cross product of the compressive force exerted by the liquid and the elevation of the protrusion above the planar surface of the solid at the point where the force is applied. As the protrusion bends, a tensile stress, σ_t of figure 2, appears on the side of the protrusion

[2] Olive Engel, J. Research NBS **54**, 281 (1955) RP2591.

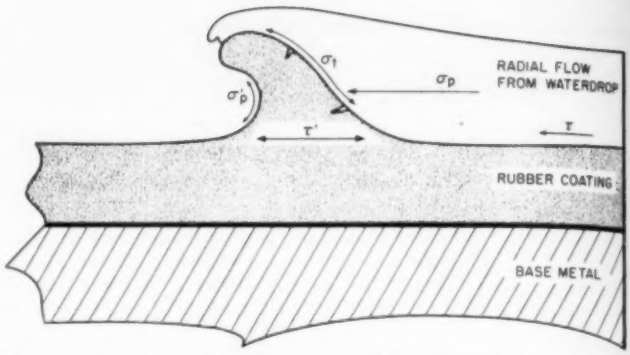

FIGURE 2. *Schematic diagram of the stresses that exist in a surface protrusion of a rubber coating as the result of the radial flow of an impinging waterdrop.*

against which the compressive force is applied and a compressive stress, σ_p' of figure 2, appears on the opposite side of the protrusion. If the force exerted by the rapidly running liquid is sufficiently great, or if the protrusion has a sufficient elevation above the planar surface, failure may occur. Whether the protrusion is simply bent over, whether it is broken off, or whether part of the solid material below the surface is torn out with it depends on the strength of the material and on where failure occurs first. Likely points of failure are marked with notches in figure 2.

If a waterdrop impinges against the planar surface of a rubberlike material the effect of the compressive stress, σ_p of figure 3, which is the direct result of the collision, is to compress the solid material at the point of impingement. The local compression results in a dimple or cup-shaped cavity. Tensile stresses, σ_t of figure 3, appear in the sides of the dimple and especially in the knee in the solid material at the rim of the dimple. If these tensile stresses are sufficiently great, tears may form in the surface layers of the solid material. The material that formerly occupied the volume that now forms the hollow of the dimple is displaced. It is moved radially outward and upward around the dimple and this results in a shear stress, τ' of figure 3. The radial flow of the liquid of the drop imposes a radial tensile stress, σ_t' of figure 3, and a shear stress, τ, which was discussed above. In the case of very thin rubbery coatings it is possible that a portion of the shear stress, τ, may be transmitted through the coating to the primer bonds,

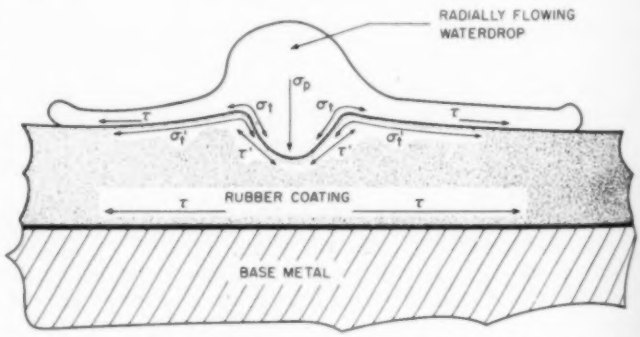

FIGURE 3. *Schematic diagram of stresses that exist in a rubberlike coating as a result of the collision and flow of a waterdrop.*

which hold the coating to the base metal, and that it may cause failure of the primer-to-rubber or of the primer-to-metal bond. However, the removal of a circle of rubber coating around the central point of the collision (stagnation point of the flow), as occurred in the case of a Neoprene coating (see fig. 6), is not necessarily the result of transmission of this shear stress through the coating. It is possible that a deep circular cut may form as a result of the tensile stress, σ_t of figure 3, in the material at the rim of the dimple or cup-shaped cavity. If this cut extends through the coating the radially flowing liquid may lift the coating with a wedge action and peel it off.

3.1. Waterdrop Traces in Fine Moist Sand

The effect of the forces that come into play when the liquid of an impinging drop flows radially can be seen in the marks that are left when waterdrops fall into fine moist sand. To obtain the picture of such traces shown in figure 4, very fine mesh sand that was just moist was gently pressed into a large petri dish. The surface of the sand was leveled and was then lightly covered with carbon black to as uniform a degree as possible. Waterdrops were allowed to fall from a flat-nosed pipet through a distance of approximately 40 ft to the surface of the carbon-covered sand. The waterdrop traces in figure 4 show clearly the existence of the stagnation point at the center of the flow where the radial flow velocity is zero; at this point the carbon has not been washed from the surface of the sand. The circular trench about the stagnation point is the result of the forces that act as a consequence of the radial flow of the liquid. The relative collision velocity was about 25 fps.

3.2. Waterdrop Traces Produced in a Neoprene Coating

Traces similar to those that formed when waterdrops were allowed to fall into the petri dish of carbon-covered sand were also found on a Neoprene [3] coated specimen that was rotated on the Cornell

[3] This was not one of the standard Neoprene coatings that fulfilled the requirements of Specification MIL–C–7439.

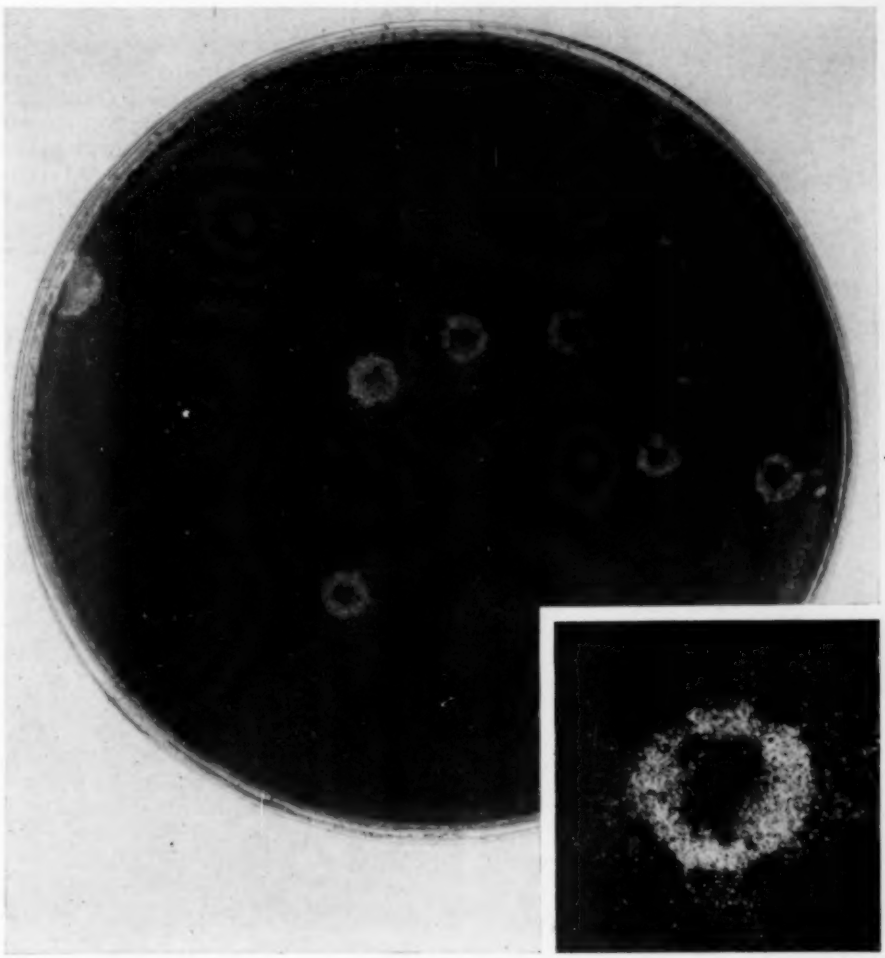

FIGURE 4. *Traces of the radial flow of waterdrops that collided with sand that was dusted with carbon black.*

The inset is a magnification of one trace.

Aeronautical Laboratory rain erosion test apparatus at a velocity of 600 mph through 1-inch per hour (iph) artificial rain for 1.5 min (see fig. 5). The average coating thickness was 8 to 10 mils. Because the surface is not completely covered with such damage marks it seems likely that traces of this kind are not produced by the first waterdrop collision with the unfatigued Neoprene coating. They are probably formed during a single collision but only after the coating has suffered deterioration of some kind (possibly permanent set) as a result of numerous radial-stretch-and-recover cycles imposed by the radial flow of waterdrops that collided earlier but that were not themselves able to produce the observable damage.

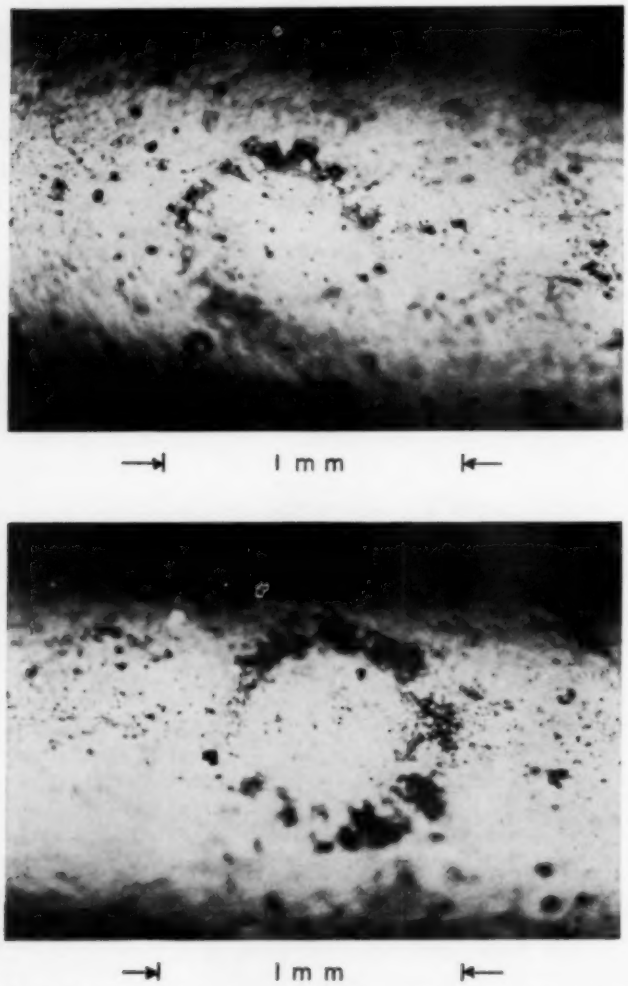

FIGURE 5. *Circular damage marks produced on an experimental Neoprene coating that collided with waterdrops at a velocity of 880 fps.*

3.3. Waterdrop Traces in Polymeric Materials

Figure 6 shows damage marks that were produced on four different polymeric materials by collision of the specimen material with waterdrops at a velocity of 2,250 fps. The experiment was carried out at Convair. The Neoprene coating was one of the standard Neoprene coatings that fulfilled the requirements of specification MIL–C–7439. Arrows in the picture point to the circular waterdrop traces. The undamaged centers, which mark the stagnation point of the radial flow, are very clear in the case of the two traces at the left of the picture. Circular damage traces were also produced in Teflon, Selectron 5003 polyester resin, and methyl methacrylate plastic. These pictures show that the forces exerted by the radial flow of a waterdrop as a result of collision with the planar surface of a solid at a velocity of 2,250 fps are effective damage tools.

4. Response of Structural Materials to High-Speed Waterdrop Impingement

The damaging properties of an impinging liquid drop that have been considered in the preceding sections are similar for drops of all liquids but vary in intensity depending on the density of the liquid, on the relative collision velocity, and on the extent to which the solid material yields under the blow. If the characteristic properties of all structural materials were the same, the appearance of damage marks produced by the impingement of drops of a given liquid against all of them at some arbitrary velocity would also be the same; there would be only one type of damage and only one mechanism by which the damage is produced. Because the characteristic properties of structural materials are different, there are as many different damage processes as there are broad groups of material properties. A specific question that was posed at the time that the research program on the mechanism of high-speed rain erosion was initiated was whether a soft rubbery material or a hard rigid material should be sought as a solution to the rain-erosion problem. These two extreme cases are considered in the following sections.

4.1. Rubberlike Yield

A material that behaves like rubber under the blow that results from collision with a liquid drop has the advantage of being a pressure reducer for the blow. When the impact pressure is reduced, the velocity of the radial flow of the liquid of the drop, which is driven by the impact pressure, is also reduced. Because the radial flow velocity is reduced, the shear stress that it exerts, which decreases as the radial flow velocity decreases, is likewise reduced. The material is, however, depressed at the point where the liquid drop struck and radial tensile stresses appear in the sides of the cup-shaped depression and around and especially over the rim of it as it forms. The surface layers of the material around the restricted area of contact between the drop and the surface of the solid are also stretched as a result of the rapid flow of liquid from the drop. A material of this kind need only have strength properties sufficient to withstand the mitigated stresses in order to remain undamaged on colliding with a liquid drop.

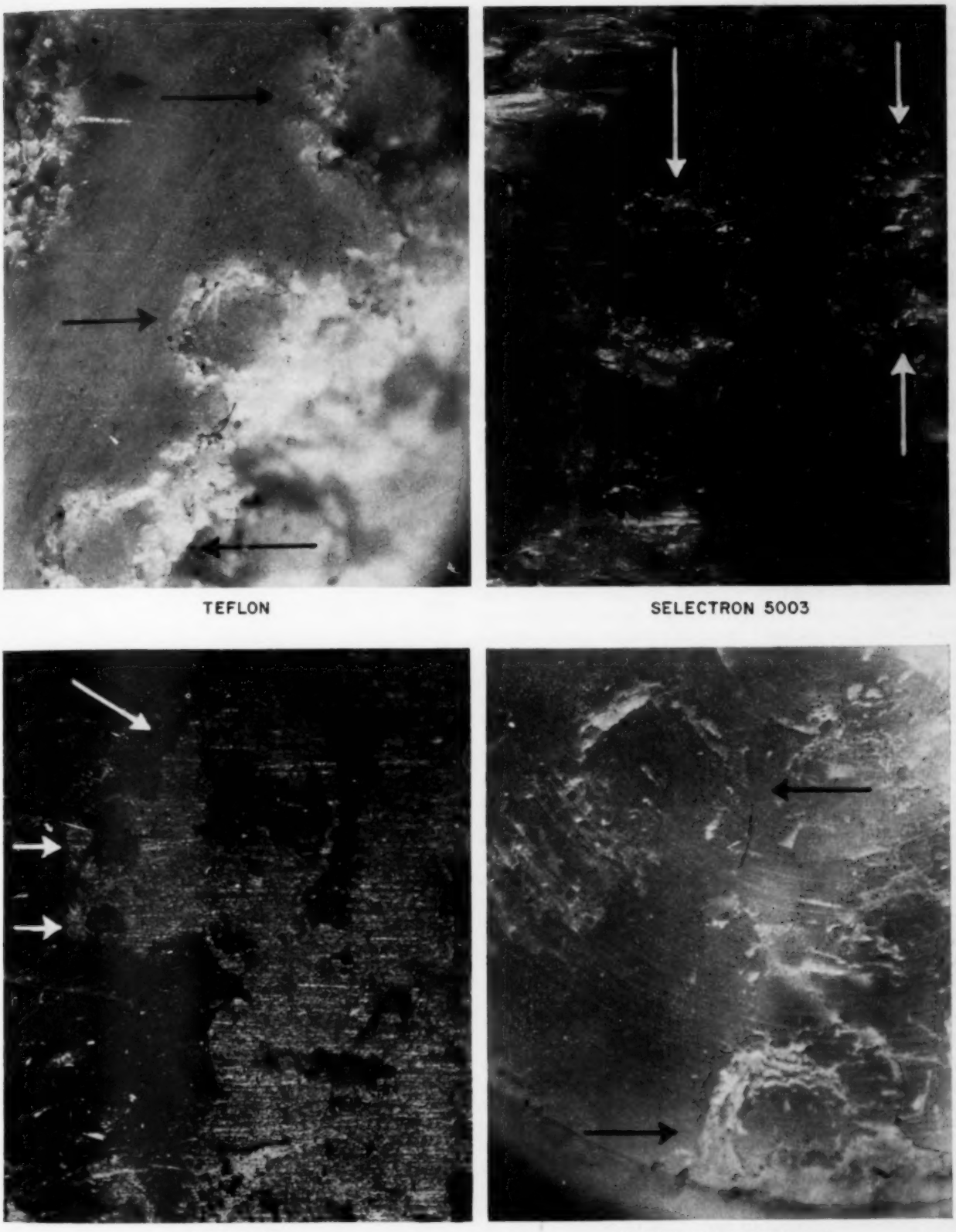

FIGURE 6. *Circular damage marks that were produced by collision with waterdrops at a velocity of 2,250 fps.*

Increase in the indentation hardness of a rubber is commonly accompanied by a decrease in its elongation under a given stress and, therefore, by a decrease in its ability to mitigate the stresses that are imposed on it by high-speed collisions with a waterdrop. The indentation hardness associated with maximum resistance against waterdrop-impingement damage at an arbitrary collision velocity is that hardness above which the gain in strength that often accompanies further hardening is unable to offset the loss in ability to mitigate the stresses that are imposed by collision with a waterdrop at the velocity in question. In terms of the rupture energy per unit volume, the optimum indentation hardness is that hardness above which the area under the stress-strain curve begins to decrease.

4.2. Resistance of Hard Materials

All materials yield to some extent under a collision blow. However, materials that do not display a high elongation under a given stress as a result of collision with a liquid drop do not mitigate to a notable degree the stresses that the colliding drop exerts. To be erosion resistant, materials of this class must be able to withstand the unmitigated stresses. Whether or not they can withstand the unmitigated stresses depends on whether they can absorb the energy of the collision before their yield or fracture strength is exceeded. If the relative collision velocity between the solid material and the liquid drop is increased without limit all the known hard materials will be found to fail at the point where their yield or fracture strength is exceeded; they will either yield with plastic flow or they will shatter.

Poly(methyl methacrylate) is a practical, rigid-material solution to the rain-erosion problem for flight velocities up to 300 mph. When specimens of poly(methyl methacrylate) are rotated through 1-iph simulated rain at a velocity of 300 mph, initial pitting of the plastic occurs after 45 min. If, however, the velocity is increased to 400 mph, initial pitting occurs after 2 min. Test results show that polystyrene and the glass-cloth-reinforced polyester resins are less resistant to rain erosion than poly(methyl methacrylate). The combined properties of rigidity and low strength eliminate these polymers as practical rain-erosion resistant materials at ordinary airplane flight velocities.

Metals undergo permanent plastic flow when their yield strength is exceeded. In the case of 1100–O aluminum, the depression in the surface caused by a single collision with a waterdrop at a velocity of 600 mph is barely perceptible. The pummeling action of repeated collisions produces, by plastic flow, a general unevenness of the surface. This unevenness appears to play a role in enhancing a delayed, drastic failure of the material. Moderately thin specimen plates of the soft and medium hard metals undergo considerable plastic flow during a single collision with a waterdrop at velocities in the range of about 1,000 to 2,000 fps; the characteristic damage mark is a pit that resembles an empty spherical segment. See figure 1, C.

The hard metals are known to afford a practical solution to the high speed rain-erosion problem at moderately low impingement velocities. Incipient failure shows up only after hours of waterdrop impingement in the erosion test at a velocity of 500 mph in a 1-iph rain density. The failure of the hard metals in this range of impingement velocity cannot be explained in terms of the impact pressure produced by collision with a waterdrop. It appears to involve pressure-raiser defects, such as microscopic pits and pores on the surface of the specimen, or weak spots in the material at or close to the surface, or both.

Of the materials that have been tested for resistance against collision with waterdrops at high relative impingement velocities, the ceramics have been found to be among the most resistant. However, if the impingement velocity is increased without limit, these materials also shatter at the point where their fracture strength is exceeded. A practical tensile strength of 30,000 psi can be expected from polycrystalline alumina compared to lower values for the soft metals and plastics.

5. Requirements for Rain-Erosion Resistance

The question that was posed several years ago as to whether the solution to the high-speed rain-erosion problem should be sought among the soft rubbery materials or among the hard rigid materials can be answered in the following way. The material may be hard and rigid, or it may be soft and rubbery and still have a high degree of rain-erosion resistance. If it is hard and rigid, it must have strength properties that will enable it to withstand, without fracture and without plastic flow, the maximum unmitigated stresses imposed by collision with a waterdrop in the velocity range for which the material is being tested; these stresses increase in magnitude as the impingement velocity is increased. If it is soft and rubbery, it need only have strength properties sufficient to withstand the mitigated stresses that are imposed by collision with the waterdrop. The velocity ceiling for the rubbery materials is the point at which they are no longer able to withstand the mitigated stresses.

These remarks apply to the ability of a material to withstand a single waterdrop blow. Under actual flight conditions successive blows on the same spot have a certain probability of being very closely spaced in time. Therefore, under flight conditions a rain-erosion resistant rubbery material must not only have strength properties adequate to withstand the mitigated stresses but must also recover fast enough to be able to mitigate the stresses of an additional blow to the extent that they do not exceed its strength properties. To be a practical rain-erosion resistant material the rubber must, furthermore, not lose its ability to mitigate the stresses through deterioration of any kind during its expected service life.

WASHINGTON, April 9, 1957.

Journal of Research of the National Bureau of Standards Vol. 61, No. 1, July 1958 Research Paper 2883

Emission Spectrum of Carbon Monoxide From 2.3 to 2.5 Microns[1]

Earle K. Plyler, Harry C. Allen, Jr., and E. D. Tidwell

The 2–0, 3–1, 4–2, 5–3, and 6–4 emission bands of carbon monoxide have been measured in the region from 4000 to 4360 cm^{-1} with a grating spectrometer. A 10,000 line per inch grating used in the second order resolved lines separated by 0.08 cm^{-1}. Several sets of measurements were made on the 2–0 band and the molecular constants were calculated. The constants in cm^{-1} are $B_0=1.922511\pm0.000025$ $D_0=6.13\pm0.02\times10^{-6}$. Using these values and the B_0 from 1–0 band in conjunction with the microwave constant a new determination of the speed of light is obtained, $c=299{,}794\pm3$ kilometers per second.

1. Introduction

The vibrational-rotational spectrum of carbon monoxide in emission was first measured in the infrared region in 1951 [1].[2] The observations were made on the harmonic band in the region from 4000 to 4360 cm^{-1}. Due to the high temperature of the flame the 2–0, 3–1, 4–2, and 5–3 transitions were observed. Recently Goldberg and Muller [2] have measured the absorption spectrum of carbon monoxide in the solar spectrum and have observed rotational lines with J values up to 75.

Other bands of carbon monoxide have also been measured. Herzberg and Rao [3] have measured the 4–0 band of CO in absorption in the near infrared, and the fundamental band at 4.67 μ has been measured by Plyler, Blaine, and Tidwell [4]. More recently 33 lines of the 2–0 band of CO have been measured by Rank and his co-workers [5]. From each set of measurements the various workers have calculated a set of molecular constants for the CO molecule and the results of different authors [2, 4, 5] are in close agreement.

Since the earlier measurements were made on the harmonic band of CO, improvements in detectors and infrared spectrometers permit more accurate measurements to be made. The bands in the 4000 to 4360 cm^{-1} region have been remeasured and this paper gives the results which have been obtained.

2. Experimental Method and Results

The emission from carbon monoxide in the 2.3-μ region was produced in two ways. First, a tube containing CO was placed in the coil of a hf oscillator. (The use of a hf oscillator for the production of molecular spectra has been previously studied by Wilkinson, Ford, and Price [6].) The pressure of the CO was 6 cm and a small flow of fresh gas was maintained. A spectrum of high intensity was observed showing transitions up to 11–9. The intensity of the rotational lines, however, varied with the pressure and the current through the oscillator coil and it was felt that more precise measurements of the lines could be made of the spectrum from a flame.

Second, the CO spectrum was observed in emission from an oxyacetylene flame. The gases were premixed and were slightly rich in fuel. The burning took place in a welding torch and a section of the flame about 2 in. above the inner cone was focused on the front slit of the spectrometer. The radiation falling on the slit was increased by reflections of mirrors around the flame [7]. A grating spectrometer with a collimating mirror of one-meter focal length and a grating of 10,000 lines/in. was used for resolving the bands. The spectrum was observed in the first and second orders, the second order giving higher resolution. Emission lines separated by 0.08 cm^{-1} were partially resolved.

The observed spectrum (4000 to 4360 cm^{-1}) includes the transitions 2–0, 3–1, 4–2, 5–3, 6–4, and 7–5. Because of the overlapping of the lines from the different transitions, precise measurements were made on the bands arising from the three lowest transitions. In figure 1 are shown the band heads and some of the rotational lines for the 2–0, 3–1, 4–2, 5–3, and 6–4 transitions. The intensity of the rotational lines with the same J values of the 2–0 and the 3–1 is about equal. In the other transitions the intensity is lower. In order to obtain sizeable deflections it was necessary to increase the amplifier gain for the other transitions; the noise level was the greatest for the 6–4 band.

The small lines appearing between the strong lines from R30 to R45 in each band arise from the band folding back on itself; these lines are part of the R branch extending up to about $J=68$. The high J values are almost superimposed on the lower J's in the 2–0 transition, but in the 3–1, 4–2, and 5–3 transitions the high J lines are well separated from the stronger lines in the region R30 to R45.

Some of the low-intensity lines observed in the 3–1 region are the R3 to R6 lines of the 2–0 band. Their low intensity shows that very few of the molecules in the flame exist in the lower rotational states. On figure 1 are given the identifications of the different lines. Precise measurements were made on the 2–0, 3–1, and 4–2 bands. When the lines of the different series overlapped they were not measured. In order to have a more complete set of measurements of the 2–0 band the lines from R20

[1] This work was supported by the Geophysics Research Directorate, Air Force Cambridge Research Center.

[2] Figures in brackets indicate the literature references at the end of this paper.

to P20 were measured in absorption. The calculated and observed wave numbers of the 2–0, 3–1, and 4–2 bands are given in table 1.

3. Discussion of Results

The molecular constants of CO have been calculated from measurements of the 4–0, 2–0, and 1–0 bands by several observers [1, 2, 3, 4, 5]. In most cases the constants determined by Goldberg and Muller; Plyler, Blaine, and Tidwell; and Rank agree within the probable error given by the authors.

The line positions measured in the 2–0 band have been used to calculate B_0, D_0 and ν_0 by the equation,

$$\nu=\nu_0+(B_2+B_0)m+(B_2-B_0-D_2+D_0)m^2-$$
$$2(D_2+D_0)m^3-(D_2-D_0)m^4.$$

TABLE 1. *Observed frequencies (cm^{-1}) and deviations from calculated values of CO lines from emission measurements*

Band	2-0				3-1				4-2			
J''	R(J)		P(J)		R(J)		P(J)		R(J)		P(J)	
	Pobs.	Pobs.−Pcalc.	Pobs.	Pobs.−Pcalc.	Pobs.	Pobs.−Pcalc.	Pobs.	Pobs.−Pcalc.	Pobs.	Pobs.−Pcalc.	Pobs.	Pobs.−Pcalc.
0	4263.842	−0.006	.....	.....	4210.91	−0.009	.....	.....	4158.15	0.011	.....	.....
1	4267.548	−.005	4256.226	[a]−0.003	4214.64	.052	.....	.....	.....	.....	.....	.....
2	4271.182	−.005	4252.308	−.006	4218.19	.002	4199.47	−0.019	4165.33	−.008	.....	.....
3	4274.750	−.001	4248.330	.000	.....	.....	4195.52	−.020	.....	.....	.....	.....
4	4278.235	−.010	4244.278	.002	4225.18	.005	.....	.....	.....	.....	.....	.....
5	4281.655	−.012	4240.150	−.002	4228.60	.038	.....	.....	4175.59	−.018	.....	.....
6	4285.013	−.006	4235.952	−.008	4231.89	.011	4183.26	−.015	4178.88	−.009	4130.74	0.000
7	4288.298	−.002	4231.694	−.004	4235.13	.005	4179.05	.002	4182.09	−.010	.....	.....
8	4291.512	.003	4227.371	.004	4238.32	.021	4174.75	−.002	.....	.....	4122.30	.013
9	4294.639	−.008	4222.974	.007	4241.41	.008	4170.38	−.008	4188.29	−.017	.....	.....
10	4297.703	−.011	4218.504	.005	4244.44	.006	4165.95	−.004	4191.28	−.024	4113.56	.001
11	4300.712	−.003	4213.962	.000	4247.40	.006	4161.45	−.002	4194.20	−.029	.....	.....
12	4303.614	−.018	4209.356	−.001	.....	.....	4156.91	.028	4197.07	−.013	.....	.....
13	4306.482	−.002	4204.673	−.010	4253.10	.001	4152.26	.017	.....	.....	.....	.....
14	4309.262	−.001	4199.931	−.010	4255.85	.007	4147.56	.023	4202.57	−.003	.....	.....
15	4311.969	−.001	4195.120	−.012	4258.52	.005	4142.80	.038	4205.19	−.020	.....	.....
16	4314.606	.001	4190.234	−.020	4261.12	.005	4137.91	−.010	4207.77	−.005	.....	.....
17	4317.173	.006	4185.302	−.007	4263.64	−.002	4133.02	.011	4210.25	−.017	.....	.....
18	4319.665	.008	4180.286	−.010	4266.10	.003	4128.05	.018	4212.67	−.017	.....	.....
19	4322.085	.011	4175.212	−.004	4268.48	.001	4123.00	.013	4215.02	−.014	.....	.....
20	4324.425	.007	4170.066	−.003	4270.79	.002	4117.89	.016	4217.29	−.018	.....	.....
21	4326.699	.010	4164.852	−.003	4272.03	.006	4112.70	.005	4219.50	−.009	.....	.....
22	4328.878	−.008	4159.564	−.009	4275.18	.002	4107.46	.011	4221.64	.004	.....	.....
23	4331.022	.012	4154.234	.009	4277.28	.004	4102.14	.004	4223.68	−.011	.....	.....
24	4333.057	−.004	4148.817	.007	4279.29	−.001	4096.74	−.016	4225.66	−.011	.....	.....
25	.....	.....	4143.33	.001	4281.21	−.023	4091.30	−.009	4227.58	.002	.....	.....
26	.....	.....	4137.79	.009	.....	.....	4085.76	−.037	4229.42	.008	.....	.....
27	.....	.....	4132.19	.023	.....	.....	.....	.....	4231.17	−.001	.....	.....
28	.....	.....	.....	.....	4286.59	−.026	.....	.....	4232.86	.004	.....	.....
29	.....	.....	4120.74	−.002	.....	.....	.....	.....	4234.47	.003	.....	.....
30	4343.804	−.010	4114.94	.010	4289.83	−.004	.....	.....	.....	.....	.....	.....
31	4345.341	−.005	.....	.....	4291.35	.019	.....	.....	4237.47	.004	.....	.....
32	4346.810	.007	4103.12	.010	4292.75	−.003	.....	.....	4238.86	.007	.....	.....
33	4348.193	.007	4097.09	−.012	4294.10	−.001	.....	.....	.....	.....	.....	.....
34	4349.494	.001	.....	.....	4295.36	−.013	.....	.....	.....	.....	.....	.....
35	4350.726	.000	4084.88	−.010	4296.57	−.001	.....	.....	4242.58	.014	.....	.....
36	4351.889	.006	.....	.....	.....	.....	.....	.....	4243.66	.007	.....	.....
37	4352.966	.002	.....	.....	4298.75	.010	.....	.....	4244.67	.005	.....	.....
38	4353.965	−.006	.....	.....	4299.72	.009	.....	.....	4245.60	−.001	.....	.....
39	4354.902	.001	.....	.....	.....	.....	.....	.....	4246.46	−.001	.....	.....
40	4355.762	.006	.....	.....	4301.42	−.006	.....	.....	4247.25	.004	.....	.....
41	4356.542	.008	.....	.....	4302.16	−.010	.....	.....	4247.96	.005	.....	.....
42	4357.241	.004	.....	.....	4302.82	−.017	.....	.....	4248.60	.013	.....	.....
43	4357.862	−.001	.....	.....	4303.41	−.018	.....	.....	4249.15	.007	.....	.....
44	4358.411	−.002	.....	.....	4303.92	−.023	.....	.....	4249.63	.007	.....	.....
45	4358.885	−.001	.....	.....	4304.36	−.021	.....	.....	4250.03	.004	.....	.....
46	4359.293	.010	.....	.....	.....	.....	.....	.....	.....	.....	.....	.....
47	.....	.....	.....	.....	4305.04	.013	.....	.....	.....	.....	.....	.....
[b]48	.....	.....	.....	.....	.....	.....	.....	.....	.....	.....	.....	.....
55	4359.367	−.006	.....	.....	.....	.....	.....	.....	4249.82	.006	.....	.....
56	4358.984	−.010	.....	.....	.....	.....	.....	.....	4249.36	−.005	.....	.....
57	4358.528	−.009	.....	.....	.....	.....	.....	.....	4248.84	.003	.....	.....
58	4357.996	−.005	.....	.....	4303.01	−.032	.....	.....	.....	.....	.....	.....
59	4357.395	.008	.....	.....	4302.37	−.022	.....	.....	4246.78	−.004	.....	.....
60	4356.691	−.003	.....	.....	4301.65	−.014	.....	.....	.....	.....	.....	.....
61	4355.922	.000	.....	.....	.....	.....	.....	.....	4245.94	−.002	.....	.....
62	4355.063	−.008	.....	.....	4299.96	−.011	.....	.....	4245.03	.009	.....	.....
63	4354.144	.004	.....	.....	4299.01	.004	.....	.....	4244.02	−.001	.....	.....
64	4353.146	.015	.....	.....	4297.93	−.031	.....	.....	4242.96	.019	.....	.....
65	4352.057	.016	.....	.....	4296.83	−.007	.....	.....	4241.79	.008	.....	.....
66	4350.885	.013	.....	.....	4295.62	−.013	.....	.....	4240.55	.007	.....	.....
67	.....	.....	.....	.....	4294.33	−.019	.....	.....	4239.24	.016	.....	.....
68	.....	.....	.....	.....	4292.97	−.015	.....	.....	.....	.....	.....	.....

[a] Lines from R20 to P20 measured in absorption. [b] No measurements were taken for $J''=48$ through 54.

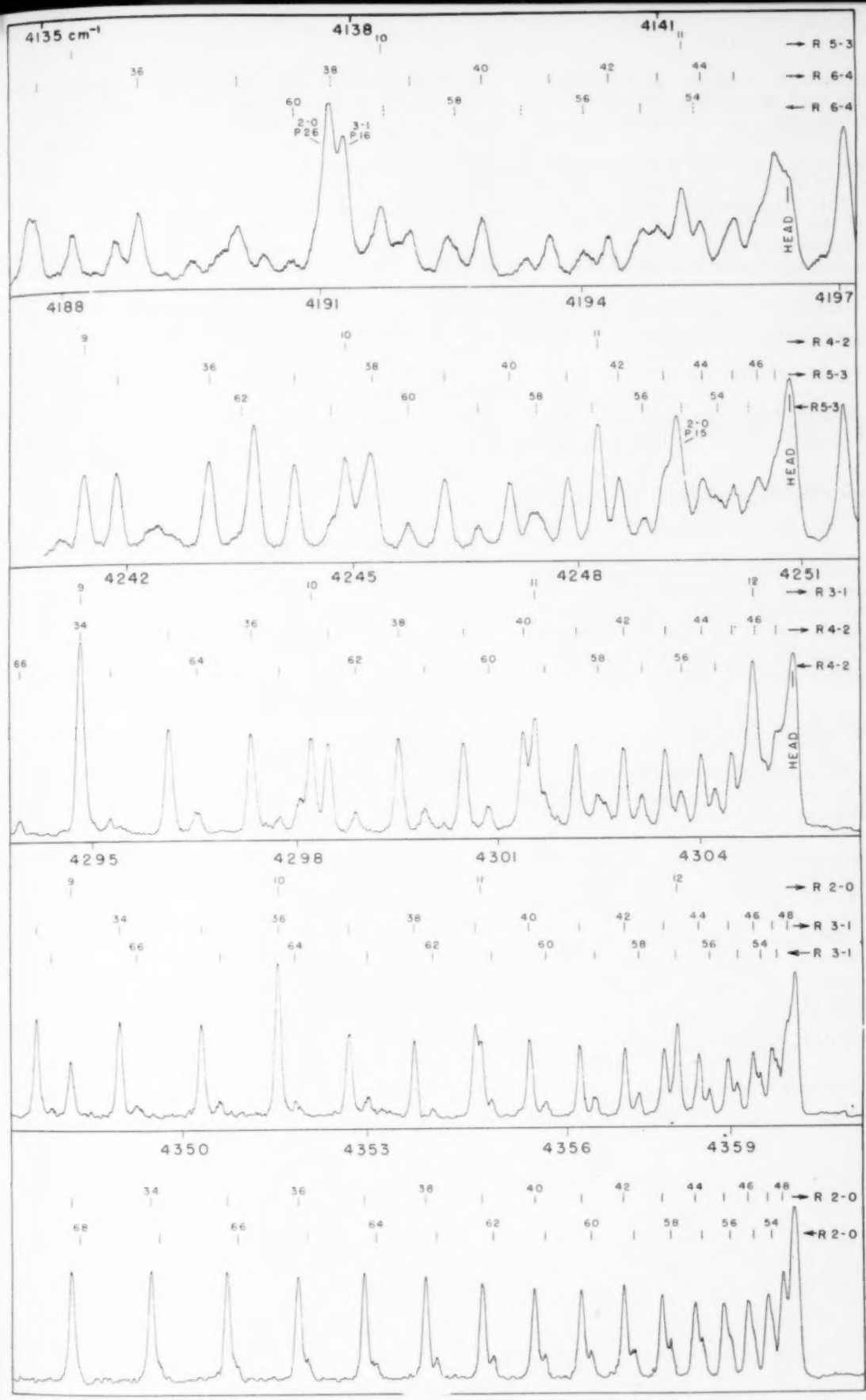

FIGURE 1.

Emission spectrum of carbon monoxide in the overtone region.

The 2-0, 3-1, 4-2, 5-3, and 6-4 band heads can be seen at the high frequency side of each trace.

The constants were calculated both with and without the m^4 term. Only very small differences occurred in ν_0, B_0, and D_0 when the fourth power term was omitted. Since D_2—D_0 is about 2×10^{-9} cm^{-1}, the contribution of this term for $J=20$ is approximately 0.001 cm^{-1} which is about one-fourth the experimental error in the measurements of the lines. Sixty-five lines of the 2–0 band were used in the calculation. They extended from R46 to P24 (see table 1). The constants obtained, in cm^{-1}, were

$$\nu_0=4260.069 \pm 0.001$$

$$B_0=1.922511 \pm 0.000028$$

$$D_0=6.13 \pm 0.022\times10^{-6}.$$

The constants B_0 and D_0 had been previously calculated from measurements of the 1–0 band [8] and found to be

$$B_0=1.922523 \pm 0.000025$$

$$D_0=6.26 \pm 0.17\times10^{-6}.$$

The standard deviations were first reported but the uncertainty is now given as probable error. The values of B_0 from the two bands fall within the error of measurements. A better value of B_0 can be obtained by combining [8] the two B_0's determined by analyses of the 1–0 and 2–0 bands, which gives the result,

$$B_0=1.922517 \pm 0.000019,$$

the uncertainty again being the probable error.

The central value of D_0 as determined from an analysis of the 2–0 band is in better agreement with the recent value of $D_0=6.131\times10^{-6}$ obtained by Gordy from the microwave spectrum [9], and the value of $D_0=6.117\times10^{-6}$ from a measurement of the 2–0 by Rank et al. [5] than was the earlier determination from the 1–0 band.

There are now two determinations for B_0 which give an average value of 1.922517 ± 0.000019. This value of B_0 is in excellent agreement with the values obtained by Rank et al. [5],

$$B_0=1.922519\pm0.000013$$

and

$$B_0=1.922521\pm0.0000035.$$

The first value was obtained from the least squares treatment of 13 Δ_2F'' values from the measurements, and the second value was the result of using a calculated value for the constant D_0 and including only the 8 largest Δ_2F'' values in the least squares treatment. Rank et al. [5] have calculated the velocity of light using the second B_0 given above and from $B_0=57{,}635.965 \pm 0.005$ Mc determined from the rotational spectrum. The result is $c=299{,}793.7 \pm 0.7$ km/sec. On using the same value of B_0 from microwave measurements and the average value from our infrared measurements, the speed of light is determined as $c=299{,}794 \pm 3$ km/sec in excellent agreement with previous determinations by this method. The central value is somewhat higher than the best value given by Bearden and Thomsen [10], 299,792.8 and also that given by Cohen, DuMond et al. [11], 299,793.0; however both of their values are within the probable error of this determination.

In conclusion, the authors thank Carroll Dannemiller for doing the least squares calculations on the Bureau's electronic computer.

4. References

[1] Earle K. Plyler, W. S. Benedict, and S. Silverman, J. Chem. Phys. **20**, 175 (1952).
[2] Leo Goldberg and Edith A. Muller, Astrophys. J. **118**, 397 (1953).
[3] G. Herzberg and K. V. Rao, J. Chem. Phys. **17**, 1099 (1949).
[4] Earle K. Plyler, Lamdin R. Blaine, and Eugene D. Tidwell, J. Research NBS **55**, 183 (1955) RP2617.
[5] D. H. Rank, A. H. Guenther, G. D. Saksena, J. N. Shearer, and T. A. Wiggins, J. Opt. Soc. Am. **47**, 686 (1957).
[6] Wilkinson, Ford, and Price, Molecular spectroscopy (Institute of Petroleum, London, 1955).
[7] Earl K. Plyler and H. J. Kostkowski, J. Opt. Soc. Am. **42**, 360 (1952).
[8] Earle K. Plyler, L. R. Blaine, and W. S. Connor, J. Opt. Soc. Am. **45**, 102 (1955).
[9] W. Gordy (private communication).
[10] J. A. Bearden and J. S. Thomsen, A survey of atomic constants (Johns Hopkins University, 1956).
[11] E. R. Cohen, J. W. M. DuMond, et al., Rev. Mod. Phys. **27**, 363 (1955).

WASHINGTON, February 5, 1958.

Journal of Research of the National Bureau of Standards Vol. 61, No. 1, July 1958 Research Paper 2884

Further Studies of the Influence of a Ridge on the Low-Frequency Ground Wave

James R. Wait and Anabeth Murphy

Computations are presented in graphical form for the perturbation of a plane wave by a semicylindrical boss on an otherwise flat ground plane of perfect conductivity. The height of the ridge is comparable to the wavelength. This is an extension of earlier work on the semielliptical boss.

A suggested model to study the effect of a nonsmooth ground for low frequencies is a semielliptical or semicylindrical boss on an otherwise flat ground plane of perfect conductivity. Using this model of a ridge, calculations were presented previously [1] for a base width of two-thirds of a wavelength and various ellipticity ratios. Recently, the computations for the semicylindrical case have been extended for other diameters. These results are presented here.

In the special case of the semicircular boss, the elliptic wave functions reduce to Bessel functions. The revelant solution is given in outline in the following.

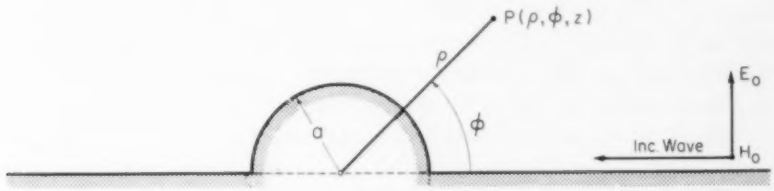

FIGURE 1. *Amplitude and phase of the field in the vicinity of a semicilindrical boss.*

Semicylindrical boss on flat ground plane and incident plane wave.

The perfectly conducting semicylindrical boss of radius a is illustrated in figure 1, along with the cylindrical coordinate system (ρ, ϕ, z). The incident wave is incident from the right, and the magnetic vector has only a z component $H_z^{\text{inc.}}$ given by [2]

$$H_z^{\text{inc.}}=H_0 e^{ik\rho\cos\phi}, \tag{1}$$

where H_0 is the amplitude of the magnetic field and $k=2\pi/\text{wavelength}$. The associated electric field is vertical and has an amplitude E_0. Using a well-known addition theorem in Bessel functions,[3] the incident field can be rewritten in the form

$$H_z^{\text{inc.}}=H_0\sum_{m=0}^{\infty}\epsilon_m e^{im\pi/2}J_m(k\rho)\cos m\phi, \tag{2}$$

where

$$\epsilon_0=1, \quad \epsilon_m=2(m=1,2,3\ldots).$$

The secondary, or scattered, field H_z is now chosen to satisfy the boundary condition that the normal derivative of the total field is zero at $\rho=a$ for $\pi>\phi>0$ and at $\phi=0$, π and $\rho>a$. Furthermore, the secondary field must contain the Hankel function $H_m^{(2)}(k\rho)$ to comply

[1] J. R. Wait and A. Murphy, Influence of a ridge on the low-frequency ground wave, J. Research NBS **58**, 1 (1957) RP2727.

[2] The time factor implied is $\exp(i\omega t)$.

[3] G. N. Watson, Theory of Bessel functions, Cambridge University Press, 2d ed. (1944).

with the radiation condition at infinity. It then follows that

$$H_z^{\text{sec.}} = -H_0 \sum_{m=0}^{\infty} \epsilon_m e^{im\pi/2} \frac{H_m^{(2)}(k\rho) J_m'(x)}{H_m^{(2)\prime}(x)} \cos m\phi, \tag{3}$$

where

$$x = ka = 2\pi a/\lambda,$$

and where the prime indicates a derivative of the Bessel function with respect to its argument.

The "relative amplitude" of the field is then defined by the quantity

$$\left[\frac{H_z^{\text{sec.}} + H_z^{\text{inc.}}}{H_0}\right].$$

The "phase lag" of the field is defined by

$$k\rho \cos\phi - \arg\left[\frac{H_z^{\text{sec.}} + H_z^{\text{inc.}}}{H_0}\right].$$

In other words, the relative amplitude is the magnitude of the total magnetic field for an incident wave of unit amplitude. The phase lag, as defined above, is the argument of the incident field less the argument of the total field.

The "relative amplitude" and "phase lag" for the magnetic field on the boss ($\rho = a$, $180° > \phi > 0°$) are plotted in figures 2,a and b, respectively, for various values of $x(=ka)$. The abscissa in both cases is the angular positon ϕ on the boss. It is immediately apparent that the amplitude of the field on the "illuminated" side ($\phi < 90°$) of the boss is approaching 2.0 as the cylinder diameter is increasing. The amplitude of the field on the shadow side ($\phi > 90°$) of the cylinder is strongly reduced for the larger cylinders. It is also interesting to note that the "phase lag" on the illuminated side is negative corresponding to a phase lead relative to the incident field while it tends to rise rather sharply on the shadow side. Geometrical optics would predict an amplitude of 2.0 and a zero phase for $0 < \phi < 90°$ and a vanishing field for $90° < \phi < 180°$. This is the asymptotic behavior as x tends to infinity.

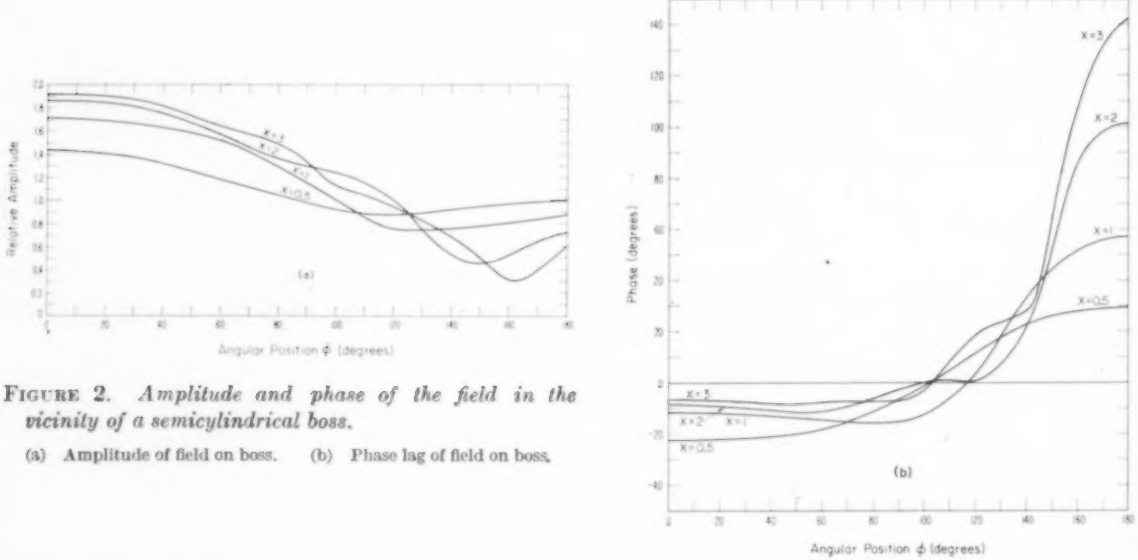

FIGURE 2. *Amplitude and phase of the field in the vicinity of a semicylindrical boss.*

(a) Amplitude of field on boss. (b) Phase lag of field on boss.

The "relative amplitude" and "phase" of the magnetic field on the ground plane in front of the boss ($\rho > a, \phi = 0°$) are shown plotted in figures 3,a and b, respectively, for a range of x. The abscissa is the distance measured from the center of the boss and expressed in radians. Here it is apparent that the secondary, or scattered, field is interfering with the incident wave to form a standing wave pattern. As would be expected, the period of the oscillation is approximately π radians or one-half wavelength.

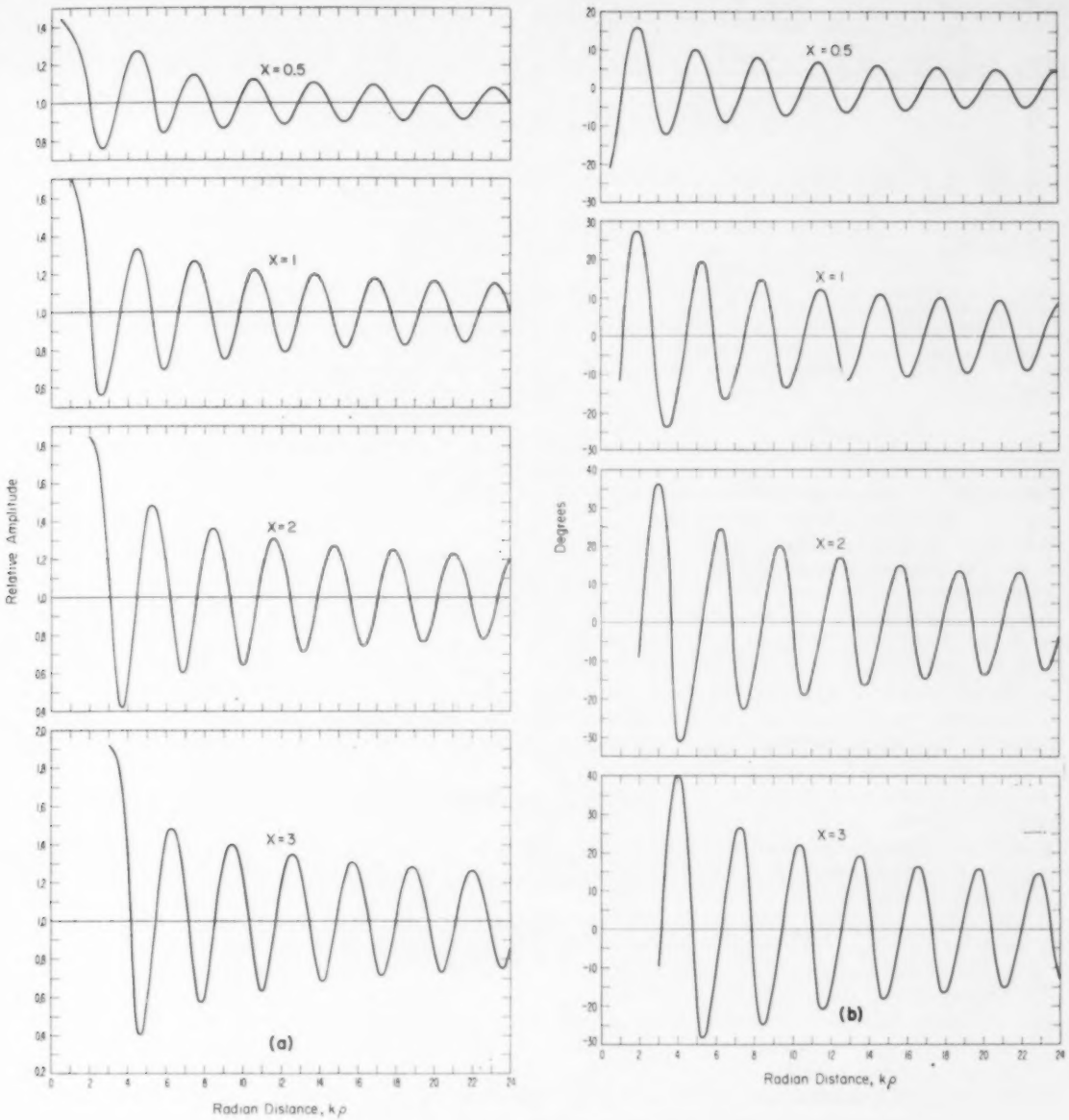

FIGURE 3. *Amplitude and phase of the field in the vicinity of a semicylindrical boss.*

(a) Amplitude of field in front of boss ($\phi=0°$). (b) Phase lag of field in front of boss ($\phi=0°$).

The same quantities for the ground plane to the rear of the boss ($\rho>a,\phi=180°$) are shown in figures 4,a and b. It is seen that the relative amplitude of the field is approaching its unperturbed value of 1.0 as the observer recedes from the ridge and the phase lag is being restored to its unperturbed value of zero. As would be expected, the larger cylinders have a more pronounced influence.

The above model is admittedly highly idealized. The restriction, however, that the conductivity of the ridge is infinite can be easily removed in the formulation. The boundary condition on the cylinder is then to be replaced by

$$E_\phi \cong -ZH_z, \tag{4}$$

where Z is the surface impedance.[4] Z for a good conductor, expressed as a ratio of the

[4] M. A. Leontovich, Approximate boundary conditions for the electromagnetic field on the surface of a good conductor, Bul. Acad. Sci., U. S. S. R. serie physique, in Russian, 9, 16, (1944).

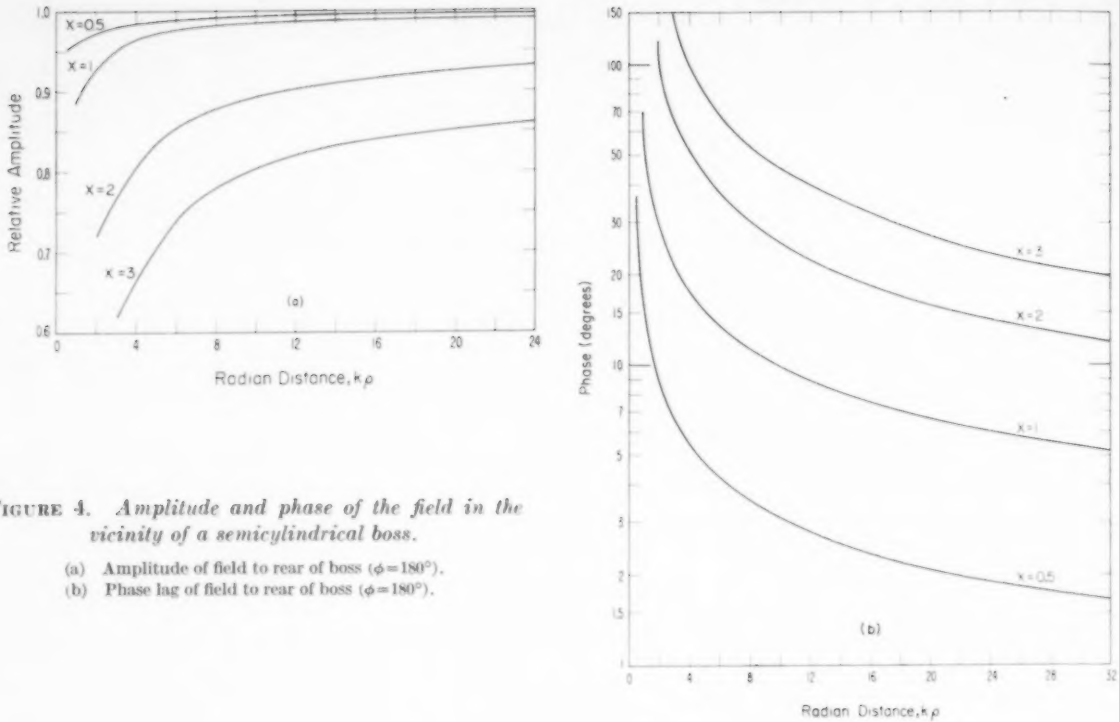

FIGURE 4. *Amplitude and phase of the field in the vicinity of a semicylindrical boss.*

(a) Amplitude of field to rear of boss ($\phi=180°$).
(b) Phase lag of field to rear of boss ($\phi=180°$).

intrinsic impedance of free space, is given by

$$Z/120\pi \cong (1+i)(\epsilon_0\omega/2\sigma)^{\frac{1}{2}}. \tag{5}$$

ϵ_0 is the dielectric constant of free space, and σ is the conductivity of the cylindrical boss or ridge. Using this boundary condition, the secondary field becomes

$$H_z^{\text{sec.}} = -H_0 \sum_{m=0}^{\infty} \epsilon_m e^{im\pi/2} \frac{J_m'(x)+GJ_m(x)}{H_m^{(2)\prime}(x)+GH_m^{(2)}(x)} H_m^{(2)}(k\rho)\cos m\phi, \tag{6}$$

where

$$G = \frac{-iZ}{120\pi} \cong (1-i)(\epsilon_0\omega/2\sigma)^{\frac{1}{2}}.$$

When $|G| << 1$ corresponding to a highly conducting cylinder, the above formula for $H_z^{\text{sec.}}$ becomes indistinguishable from its perfectly conducting counterpart given by eq (3).

The assumption of a perfectly conducting ground is not as simple to remove. However, if attention is confined to within several wavelengths of the ridge, the incident ground wave would behave locally as a plane wave at low-radio frequencies for a moderately or a well-conducting ground.

The restriction to normal incidence of the plane wave on the perfectly conducting cylindrical boss is easily removed. The only change necessary is to replace k by $k \sin\theta$ everywhere (θ is the angle subtended by the incident wave normal and the axis of the cylinder). The parameter x in the figures is then equal to $ka \sin\theta$ and $k\rho$ is replaced by $k\rho \sin\theta$.

Ground-wave propagation over ridges or obstacles of finite length could be treated in the same fashion, using semispherical or semispheroidal bosses, although the computations would become excessively tedious. The results presented here for the semicylindrical boss and the earlier ones for the semielliptical boss are believed to be satisfactory to yield an initial estimate of the magnitude of the effect. Subsequent computations for more elaborate models would be justified if careful experimental measurements could be carried out under controlled conditions.

BOULDER, COLO., March 13, 1958.

Journal of Research of the National Bureau of Standards Vol. 61, No. 1, July 1958 Research Paper 2885

Infrared Studies on Polymorphs of Silicon Dioxide and Germanium Dioxide

Ellis R. Lippincott,[1] Alvin Van Valkenburg, Charles E. Weir, and Elmer N. Bunting

The infrared spectra of coesite, low-temperature tridymite, low-temperature cristobalite-low-temperature quartz, vitreous silica, hexagonal GeO_2, tetragonal GeO_2, and vitreous germania are reported from 4,000 to 300 cm^{-1}. Wherever possible an assignment of frequencies has been made on the basis of the selection rules for the crystal symmetry. Three characteristic group frequencies near 1,100, 800, and 480 cm^{-1} are common to all the polymorphs of SiO_2. These frequencies respectively correspond to a stretching mode involving displacements associated primarily with the oxygen atoms, a stretching mode involving displacements associated primarily with the silicon atoms, and a Si-O bending mode. The presence of these group frequencies in coesite indicates that the coordination of silicon in coesite is tetrahedral and that its high density is associated with the packing of tetrahedral units at an angle approximating 120 degrees. The tetragonal and hexagonal GeO_2 polymorphs show a marked difference in spectra due in part to the change from sixfold to fourfold coordination. The assignment of observed frequencies in hexagonal GeO_2 is consistent with that made for low-temperature quartz if allowance is made for the heavier mass of the Ge atom.

1. Introduction

Several investigators have presented a detailed analysis of the vibrational spectrum of quartz [1].[2] Infrared spectra of cristobalite and fused silica have been reported but no specific assignments of their spectra appear to have been given [1]. Infrared spectra are presented of the SiO_2 polymorphs of coesite, cristobalite, tridymite, and vitreous silica; also the GeO_2 polymorphs of hexagonal GeO_2, tetragonal GeO_2, and vitreous GeO_2, in the region from 4,000 cm^{-1} to 300 cm^{-1}. A partial interpretation of the spectra in terms of respective structures and selection rules is given. Particular emphasis has been placed on locating characteristic frequencies and on classifying the observed frequencies in terms of types of vibrations. The assignment of frequencies is admittedly tentative in part because either the true crystal symmetry is not known, the spectral data are incomplete, or the spectra are too complex. Because coordination of silicon in coesite [2] has not been established, one of the objectives of this work was to furnish evidence for either the fourfold coordination of the other polymorphs of SiO_2 or for a different coordination. In the tetragonal form of GeO_2 the germanium atom has a sixfold coordination with oxygen, whereas in the quartz-type hexagonal GeO_2 the germanium atom has the fourfold coordination of silicon in quartz [3, 4]. A similar tetragonal form of silica is not known but has been predicted by analogy with germania.

2. Experimental Procedure

2.1. Samples

The cristobalite was prepared from ethyl orthosilicate by the usual hydrolysis technique. The SiO_2 thus obtained was heated to 1,600°C for 5 hr. Its X-ray powder pattern was identical with that found for natural cristobalite. A quartz sample of high purity was obtained from the Geophysical Laboratory (standard sample). Crystals of coesite were prepared from precipitated silicic acid which was subjected to 30,000 atm at 600°C for one-half hour. The X-ray powder pattern and indices of refraction of this material agree with those reported by Coes [2]. Tridymite was prepared by C. N. Fenner of the Geophysical Laboratory. The preparation was accomplished by heating pure quartz and Na_2WO_4 at 1,000° C for 71 hr, followed by careful purification of the tridymite. The fused silica was obtained by fusing a sample of pure quartz in the usual manner.

The germanium oxide was obtained commercially. Microscopic examination showed extremely fine particles less than 1 μ in size. X-ray powder patterns of the material coincided with those reported for the hexagonal form of GeO_2 [4]. The tetragonal form of GeO_2 was prepared hydrothermally. The hexagonal GeO_2 was sealed with water in a platinum capsule and heated at 800° C at a pressure of 20,000 psi for 3 days. Microscopic examination showed some crystal growth of tetragonal GeO_2, but crystals were still too small (circa 1 μ) to permit more than an estimation of the index, approximately 1.99. X-ray patterns showed tetragonal GeO_2 with a small amount—estimated at less than 5 percent—of unconverted hexagonal material. Spectroscopic analysis of the tetragonal material showed principal impurities to be Pt 0.1 to 1.0 percent; Al, Ca, Fe, Pd, and Si 0.01 to 0.1 percent; and smaller quantities of Ag, Ba, Cu, Mg, Mn, and Pb, which were found as traces. Vitreous GeO_2 was formed by quenching fused hexagonal GeO_2 in a platinum container.

2.2. Infrared Studies

Infrared spectra of the samples were obtained on a double-beam spectrophotometer with NaCl prism in the region 4,000 to 650 cm^{-1} and on a single-beam double-pass spectrophotometer with CsBr prism in the region 700 to 300 cm^{-1}. The samples were

[1] Consultant to the Mineral Products Division, National Bureau of Standards. Present address, Department of Chemistry, University of Maryland, College Park, Maryland.

[2] Figures in brackets indicate the literature references at the end of this paper.

ground in a boron carbide mortar, mixed with dry ground KBr and pressed into KBr pellets at 100,000 psi by standard techniques [5]. The concentrations range from 2 to 3 mg of sample per gram of KBr. The spectra from 4,000 cm^{-1} to 300 cm^{-1} are given in figures 1 to 15. The region above 1,500 cm^{-1} contained no fundamental frequencies for any of the polymorphs of SiO_2 or GeO_2. Absorption peaks near 3,500 cm^{-1} were due to water present in the KBr. The observed frequencies given in figures 1 to 15 are tabulated in tables 2, 4, 5, 7, 8, and 9.

3. Interpretations

A SiO_2 group in a rigid framework has 3N-3 or six vibrational degrees of freedom. There is some ambiguity as to how the corresponding modes of vibration should be classified in terms of bond stretching, bond bending, and bond-distortion types. Somewhat arbitrarily a bond-stretching and bond-bending mode will be associated with each O atom. These O-stretching modes should correspond to the highest observed frequencies in the spectrum. Two remaining degrees of freedom need to be assigned to the Si atom. One of these must be a stretching mode corresponding approximately to motions of the Si atom between the two O atoms. The one remaining mode must correspond to a low-frequency distortion or bending motion of the Si atom.

For each SiO_2 group which is added to the first to make up the unit cell, one must add nine vibrational degrees of freedom. These nine modes may be classified approximately into the following types. Because each added SiO_2 group corresponds to the addition of four bonds, four of the nine modes correspond to bond-stretching frequencies, two involving displacements associated with the O atoms and two for the Si atom. (Using another description these would correspond to two antisymmetric stretching modes of the type ←Si O→←Si, and two symmetric stretching modes of the type ←Si O Si→.) Two more of these nine modes may be classified as bending motions associated with the bending of Si-O-Si angle. The remaining three modes are associated with low-frequency bending or distortion frequencies. Table 1 summarizes this classification of the modes of vibration for various numbers of SiO_2 groups per unit cell. The case for N equal to 3 corresponds to quartz and that for N equal to 8 to cristobalite. It should be emphasized that this classification into types is only approximate and that in general a given mode will be a mixture of stretching, bending, and distortions types. The proper method of classifying these modes would be in terms of the symmetry elements of the crystal. For quartz this has been impressively illustrated by Saksena [1]. Because there is some doubt as to the true crystal symmetry of cristobalite, and that of coesite [2] has not been described in detail, this method of classifying normal modes on the basis of symmetry is not possible at the present time for these latter two forms of silica.

TABLE 1. *Descriptive classification of the modes of vibration for different numbers of* SiO_2 *groups per unit cell*

	SiO_2 groups per unit cell						Spectral region assigned for polymorphs of SiO_2.
	1	2	3	4	6	8	
Number of Si-O stretching modes involving motion primarily associated with the oxygen atoms.	2	4	6	8	12	16	1,200 to 1,000 cm^{-1}.
Number of stretching modes involving motion primarily associated with the silicon atoms.[3]	1	3	5	7	11	15	825 to 600 cm^{-1}.
Si-O bending modes	2	4	6	8	12	16	600 to 390 cm^{-1}.
Distortion modes	1	4	7	10	16	22	380 to 100 cm^{-1}.
Total modes	6	15	24	33	51	69	

The feasibility of the method outlined above for the classifications of the normal modes of various forms of silica may be tested on the assignment given for quartz by Saksena [1]. From table 1 one would expect, in order of decreasing frequency, four distinct spectral groupings consisting of six Si-O stretching modes involving displacements associated primarily with the O atoms, five stretching modes involving displacements associated primarily with the silicon atom, six Si-O-Si bending modes and seven low-frequency distortion modes. These are readily associated with the frequencies observed in the following regions of the spectrum: 1,200 to 1,000 cm^{-1}, 825 to 600 cm^{-1}, 600 to 390 cm^{-1}, and 380 to 100 cm^{-1}, respectively. The distinction between the latter two groupings is somewhat arbitrary. If one allows for the fact that frequencies assigned to species E in table 2 must be counted twice because they are doubly degenerate, it is found that these groupings contain 6, 5, 6, and 7 degrees of freedom, respectively, in agreement with the numbers expected from a unit cell containing three SiO_2 groups.

3.1. Cristobalite

The observed spectra were taken on low-temperature α-cristobalite. Since little information is available about its structure, the spectra are interpreted on the basis of that for high cristobalite for which more structural information is available [6, 7]. High cristobalite was studied by Wyckoff for which he proposed a cubic structure of space-group symmetry $O_h^7 = Fd3m$ with eight SiO_2 groups per unit cell [6]. Application of O_h selection rules shows that only 5 triply degenerate fundamental frequencies of species F_{1K} corresponding to 15 of the 69 modes of vibration for the unit cell should appear in the infrared spectrum. Because the observed spectrum of low-temperature cristobalite contains at least seven frequencies plus additional low-frequency peaks below 300 cm^{-1}, it is not feasible to interpret the infrared spectrum on the basis of $O_h^7 = Fd3m$ space-group symmetry. Barth [7] reexamined the structure of high temperature β-cristobalite and concluded that its structure corresponded to a lower symmetry and proposed a structure with space-group symmetry $T^4 = P2_13$. Application of T-selection rules to a unit cell with eight SiO_2 units predicts that seventeen triply degenerate fundamental frequencies should be observed in the infrared spectrum. At least twelve

TABLE 2. *Classification of fundamental frequencies (cm^{-1}) in α-Quartz*

Species	Spectral activity	Saksena [a]	Kirshman [a]	Barriol [a]	Simons and McMahon [a]	This work [b]	Descriptive assignment
A	Raman	207	207	207	----------	(207)	Distortion.
		356	258	356	----------	(356)	Distortion.
		466	467	466	----------	(466)	Si-O bending.
		1,082	1,082	1,082	----------	(1,082)	Si-O stretching.
B	Infrared with no dipole ' Z [c]	364	378	385	----------	374	Distortion.
		508	480	488	----------	513	Si-O bending.
		777	805	800	790	780	Si stretching.
		1,149	----------	1,190, 1,227	1,055	1,150	Si-O stretching.
E [d]	Infrared with no dipole " Z [c]	128	127	127	----------	(128)	Distortion.
		392 to 403	404	394	----------	397	Si-O bending.
		695	696	696	695	696	Si stretching.
		1,159	1,160	1,163	1,162	1,176	Si-O stretching.
		265	267	268	----------	(265)	Distortion.
		479	----------	----------	----------	462 to 475	Si-O bending.
		795 to 807	794	798	795 to 802	801	Si stretching.
		1,063	1,065	----------	1,065	1,097	Si-O stretching.
		----------	1,228	1,228	----------		

[a] See reference in text. [b] Figures in parentheses indicate the use of Saksena's assignment. [c] Direction of optic axis. [d] Species E is doubly degenerate and the observed frequencies correspond to two modes.

of these should be observed in the region above 300 cm^{-1}, and it is considered unlikely that a satisfactory interpretation of the spectrum can be made on the basis of space-group symmetry $T^4=P2_13$.

These considerations suggest that a tentative assignment and classification of observed frequencies may be made on the basis of a different symmetry which has vibrational selection rules not as stringent as an O_h structure but more restrictive than a T structure. To accomplish this, the T_d selection rules are assumed to be of approximate value [8]. The vibrational species for a structure of T_d symmetry are A_1, A_2, E, F_1 and F_2. Of these the only species which is infrared active is F_2. Ten fundamental triply degenerate infrared frequencies are predicted, of which eight should appear in the region above 300 cm^{-1}. This latter number corresponds closely with the number of observed frequencies. In table 3 are summarized the distribution of Si-O stretching, Si stretching, Si-O bending, and low-frequency distortion modes among the vibrational species for a structure of T_d symmetry. The three Si-O stretching modes may be assigned to the peaks observed at 1,204, 1,160 and 1,104 cm^{-1}, respectively. The two Si stretching modes involving displacements associated primarily with motion of the Si atoms may be assigned to the peaks observed at 798 and 620 cm^{-1}, respectively. The three bending modes have been assigned to the bands observed near 515 and 485 cm^{-1}. The two infrared active distortion modes are expected in the 150 to 200 cm^{-1} region and would not be observed. The classificaton given in table 4, based on assumed T_d selection rules and group frequencies, explains the fact that the observed spectrum is simpler than that of quartz and enables one to obtain a tentative assignment of all the observed frequencies.

A more detailed and complete assignment for cristobalite must await the obtaining of a Raman spectrum and additional infrared studies at longer wavelengths on single crystals, followed by an analysis based on the true crystal symmetry.

A comparison of the spectra of quartz and of cristobalite shows that the most intense component of the Si-O antisymmetric stretching frequencies

TABLE 3. *Section rules and group frequency classification for a T_d structure with 8 SiO_2 groups per unit cell*

Species [a]	Spectral activity	Total frequencies	Si-O stretchings	Si stretchings	Si-O bendings	Low frequency distortions
A_1	Raman	5	2	1	2	------
A_2	Inactive	1	------	------	------	1
E	Raman	6	1	1	1	3
F_1	Inactive	7	1	2	1	3
F_2	Infrared and Raman.	10	3	2	3	2

[a] The E and F species are doubly and triply degenerate and the corresponding frequencies must be counted two and three times, respectively.

TABLE 4. *Classification of observed infrared frequencies for cristobalite* [a]

cm^{-1}	Description
485	Si-O bending.
515	Si-O bending.
620	Si stretching.
798	Si tretching.
1,104	Si-O tretching.
1,160	Si-O stretching.
1,204	Si-O stretching.

[a] F_2 is the only active infrared species for T_d symmetry. The Raman active species are A_1, E_1, and F_2.

differs by only 7 cm^{-1}, with the peak for cristobalite being at the larger cm^{-1} value. This result is somewhat different from that found by Simmons and McMahon [1] with infrared reflection studies, where the Si-O stretching frequency was found at different cm^{-1} values for quartz, cristobalite, and fused silica. Likewise the Si stretching frequencies near 800 cm^{-1} do not differ greatly between the two forms. The only other frequencies that appear to be somewhat the same in both forms are those that correspond to the strong peaks occurring in the region 460 to 515 cm^{-1}. These frequencies have been assigned to a mixed Si-O-Si and O-Si-O bending mode. However, corresponding low-frequency peaks in quartz are definitely shifted to lower frequencies from their counterparts in cristobalite. This shift will be

tentatively associated with the change in angle that the tetrahedral units make with each other in the respective structures. The fact that the Si and Si-O stretching frequencies occur at nearly the same positions, respectively, in both compounds indicates that the difference in structure between the two is associated with the orientation of the tetrahedral unit rather than any great difference between Si-O bond distances or Si-O bond-stretching force constants, resulting from a change of coordination.

3.2. Coesite

The infrared spectrum of coesite given in figure 3 and tabulated in table 5 is richer and more complex than that for either quartz or cristobalite. This is expected since the crystal symmetry of coesite [2] is lower (space group C_c or $C_{2/c}$) and has 16 to 18 SiO_2 groups per unit cell. Two factors make it difficult to obtain an assignment of frequencies for coesite. First, the exact crystal symmetry is not known, nor can a pseudo structure of high symmetry be assumed to simplify the anaylsis. Second,the exact number of SiO_2 groups per unit cell is uncertain. However, the infrared spectrum of coesite shows the presence of group frequencies similar to those found in quartz and cristobalite. The Si-O stretching frequencies appear near 1,100 cm^{-1} whereas the Si stretching frequencies appear near 800 cm^{-1}. This indicates that the tetrahedral unit in coesite is still intact and that there has been no change in coordination of the Si atom or marked change in Si-O bond length or marked change in Si-O bond stretching-force constant. (It is interesting that this is not the case for the hexagonal and tetragonal forms of GeO_2.) The difference in structure appears to be due to the packing of the tetrahedral units. Evidence for this is that the mixed Si-O-Si and O-Si-O bending frequencies, which appear at 515 and 485 cm^{-1} in cristobalite and at 475 and 462 cm^{-1} in quartz, shift to 442 and 430 in coesite. We interpret this shift to be associated with the change in angle between the tetrahedral units of the three structures. Empirically one may estimate this angle in coesite by correlating this shift with the known angles in cristobalite and quartz, which are near 180° and 150°, respectively. This indicates that this angle in coesite is approximately 120° ±10°.

TABLE 5. *Classification of observed infrared frequencies of coesite*

cm^{-1}	Description
340	Distortion.
390 430 442 557 598	Si-O-Si and O-Si-O bending.
683 796 813	Si stretching (←Si-O-Si→).
1,040 1,098 1,170 1,225	Si-O stretching (←Si O→ ←Si).

3.3. Low-Temperature Tridymite

Low-temperature tridymite forms orthorhombic crystals with 64 SiO_2 groups per unit cell [9]. The true crystal symmetry is not known, but it is believed to be a distorted form of the simpler high-temperature β-tridymite, which has a simple hexagonal structure of $D_{3h}^4 = C\bar{6}2c$ or $D_{3h}^4 = C6/mmc$ space-group symmetry. In order to obtain an approximate interpretation of the infrared spectrum of the low-temperature tridymite it is assumed that the selection rules for the high-temperature tridymite of D_{3h}^4 symmetry are approximately valid despite the fact that the true symmetry is a distortion of the D_{3h}^4 symmetry. The infrared active species are A_2'' and E' corresponding to nine fundamental frequencies ($4A_2''$ and $5E_1'$). The D_{3h} selection rules [8] and a classification of Si-O stretching, Si stretching, Si-O bending, and low-frequency distortion modes are given in table 6. The two Si-O stretching modes in species A_2'' have been assigned to the peaks observed at 1,109 and 1,175 cm^{-1}. The A_2'' Si-O bending mode has been assigned to the 478 cm^{-1} peaks. The distortion mode in A_2'' would be expected near 200 cm^{-1} and has not been observed. The five frequencies of species E' have been classified as corresponding to an Si-O stretching, an Si stretching, two Si-O bendings, and a distortion mode. The Si-O stretching has been assigned at 1,109 cm^{-1}, the Si stretching at 792 cm^{-1} and the two Si-O bendings to the 478 cm^{-1} peak and its nearby component. The low-frequency distortion would be expected in the 150 to 200 cm^{-1} regions and would be missed by the instruments used in this work.

TABLE 6. *Selection rules and classification of modes of vibration for tridymite assuming space group* $D_{3h}^4 = C\bar{6}2c$

Species[a]	Spectral activity	Total frequencies	Si-O stretchings	Si stretchings	Si-O bending	Low frequency distortions
A_1'	Raman	5	2	1	1	1
A_1''	Inactive	1	.....	.....	.....	1
A_2'	Inactive	1	.....	.....	.....	1
A_2''	Infrared	4	2	.....	1	1
E'	Infrared and Raman.	5	1	1	2	1
E''	Raman	6	1	2	1	2

[a] The E frequencies are doubly degenerate and each E frequency corresponds to two modes of vibration.

This classification of frequencies based on selection rules for the $D_{3h}^4 = C\bar{6}2c$ space group enables one to obtain a tentative assignment of all observed frequencies (table 7) and to understand why the observed spectrum for tridymite is simpler than that found for both quartz and cristobalite. In particular it explains the observation that only one frequency is observed in the 850 to 625 cm^{-1} region of the spectrum corresponding to a stretching mode associated with motion of the Si atoms.

Although the actual symmetry is lower this indicates that the deviation from D_{3h} selection rules is apparently not enough to cause a significant change

in the appearance of the infrared spectrum. A more detailed analysis of the spectrum could be made if a Raman spectrum were available. It is interesting that the three observed frequencies in tridymite corresponding to an antisymmetric Si-O stretching, a Si stretching, and to a characteristic mixed O-Si-O and Si-O-Si bending, respectively, appear near the same cm^{-1} values in quartz, cristobalite, and coesite indicating that they may be classified as characteristic group frequencies. The mixed-bending frequency observed at 478 cm^{-1} corresponds to a frequency close to that observed for cristobalite. The slightly lower values observed in quartz and coesite are interpreted as being due to the change of angle of the tetrahedral units from 180°.

TABLE 7. *Classification of observed infrared frequencies of tridymite on the basis of* D_{3h} *selection rules*

Species[a]	cm^{-1}	Type
A''_2	478	Si-O bending.
E'	508	Si-O bending.
E'	792	Si stretching.
A''_2	1,109	Si-O stretching.
E'	1,175 broad	Si-O stretching.
A''_2	1,175 broad	

[a] The E frequencies are doubly degenerate and each E frequency corresponds to two modes of vibration.

3.4. Vitreous Silica

The infrared spectrum of vitreous silica is given in figure 5. The spectrum is characterized by the presence of strong bands at 1,108 cm^{-1}, 805 cm^{-1}, and 468 cm^{-1} and may be assigned as the Si-O stretching, Si stretching, and Si-O-Si bending characteristic group frequencies, respectively. These frequencies are at essentially the same positions as in the other SiO_2 modifications, but they are somewhat broader. The broad peak near 805 cm^{-1} has its peak absorption at slightly higher cm^{-1} values than the other polymorphs of SiO_2. This would indicate that there again is no change in the coordination of the tetrahedral units. The broadening of the bonds may be due to the random packing of the tetrahedral units. The infrared spectrum of vitreous silica resembles tridymite in appearance with the same number of observed frequencies.

3.5. GeO_2

The infrared spectra of three different modifications of GeO_2 are given in figures 6, 7, 8, 14, and 15, corresponding to the tetragonal, hexagonal, and vitreous forms. The tetragonal form has a rutile structure with two GeO_2 groups per unit cell, corresponding to sixfold octahedral coordination. The hexagonal form has a quartz-type structure with three GeO_2 groups per unit cell, corresponding to a tetrahedral coordination. This difference in coordination results in a large difference in frequency of the Ge-O-Ge antisymmetric stretching mode of vibration observed in both spectra. In tetragonal GeO_2 this frequency is at 720 cm^{-1}, whereas in hexagonal quartz-like GeO_2 it is found at 885 cm^{-1}, a difference of 165 cm^{-1}. This difference is due to the markedly different Ge-O bond length and bond energy for the two forms. For tetragonal GeO_2, the Ge-O bond length [3] is 1.86 A. The bond length for the hexagonal GeO_2 has not been given, but it is likely that it is shorter than 1.86 A, corresponding to a stronger bond and larger bond-stretching force constant and vibrational frequency. The large difference in the Ge-O-Ge antisymmetric stretching frequency for those two forms of GeO_2 is in marked contrast to the positions of the Si-O-Si antisymmetric stretching frequency for the various forms of silica. There is only a small shift in the position of this frequency for the various forms of SiO_2 indicating that there is no change of coordination and no, or only minor, changes in Si-O bond lengths, bond energies, and bond stretching force constants. The difference in structure of the various forms of silica must be associated with the packing of the tetrahedral units.

The selection rules [8] for a tetragonal GeO_2 structure with $D_{4h}^{14}=P4/mnm$ space-group symmetry and two GeO_2 groups per unit cell predict the presence of six infrared active fundamental frequencies (3 A_{2u} and 3 E_u). The observed frequencies and assignment are given in table 8. The three frequencies of species A_{2u} have been classified as antisymmetric Ge-O stretching, a Ge-O bending, and a low-frequency distortion mode. The first two modes have been assigned to the peaks observed at 720 and 513 cm^{-1}. The third mode of species A_{2u} is expected in the regions 125 to 200 cm^{-1} and would not be observed with the instruments used in this research. The three frequencies of species E_u have been classified as a Ge-O stretching, a Ge stretching, and a Ge-O bending, and are assigned at 720, 525, and 425 cm^{-1}, respectively. No attempt will be made to explain the shoulders appearing on the 425 cm^{-1} band.

TABLE 8. *Classification of the observed infrared frequencies of tetragonal* GeO_2

Species[a]	cm^{-1}	Type
A_u	-------	Distortion.
E_u	425	Ge-O bending.
A_{1u}	513	Ge-O bending.
E_u	515	Ge stretching.
A_{2u}, E_u	720	Ge-O stretching.

[a] Each E frequency is doubly degenerate and corresponds to two modes of vibration.

A detailed interpretation of hexagonal GeO_2 would require the obtaining of an infrared spectrum run at lower frequencies as well as a Raman spectrum. However, the observed spectrum is consistent with that found for low-temperature quartz. The strong peak at 885 cm^{-1} is clearly the analogue of the 1,100 cm^{-1} Si-O-Si antisymmetric stretching frequencies of quartz in species B and E and must consist of two fundamental frequencies. The 801 cm^{-1} and 782 cm^{-1} peaks of quartz correspond to the Si stretching modes and would be expected to shift markedly in hexagonal GeO_2 because of the heavier mass of the Ge atom. Tentatively these two peaks

TABLE 9. *Classification of the observed infrared frequencies for hexagonal* GeO_2 (cm^{-1})

Species	GeO_2	Type	Quartz assignment
A (Raman active)	.....	.....	.....
B (Infrared active)	.....	Distortion	374
	345	Ge-O bending	513
	515	Ge stretching	780
	885	Ge-O stretching	1,150
	.....	.....	128
	.....	.....	397
	585	Ge stretching	696
E (Infrared active)	963	Ge-O stretching	1,176
	.....	.....	265
	332	Ge-O bending	462 to 475
	540	Ge-stretching	801
	885	Ge-O stretching	1,097

of quartz will be respectively associated with the peaks of hexagonal GeO_2 at 540 cm^{-1} and 515 cm^{-1}. The first of these has been assigned to species E and the latter to species B of the quartz structure. The 696 cm^{-1} band of quartz must then be shifted to 585 cm^{-1} in GeO_2 and assigned to species E. The two remaining frequencies observed in hexagonal GeO_2 at 345 cm^{-1} and 332 cm^{-1} must be considered as the analogs of the mixed Si-O-Si, O-Si-O bending frequencies observed in quartz at 513 cm^{-1} and 462 cm^{-1}, respectively. The first (345 cm^{-1}) must be assigned to species B, and the second (332 cm^{-1}) to species E of the quartz structure. This assignment is given in table 9.

The Ge-O-Ge antisymmetric stretching of vitreous GeO_2 is found at 895 cm^{-1} as a broad band and indicates its similarity with hexagonal GeO_2 in that both consist of tetrahedrally coordinated GeO_2 units. No additional low-frequency bands were observed in fused GeO_2.

4. References and Notes

[1] B. D. Saksena, Proc. Indian Acad. Sci., [A] **12,** 93 (1940); R. S. Krishnan, Nature **155,** 452 (1945); J. Barriol, J. Phys. radium **7** [8], 209 (1946); F. Matossi, J. Chem. Phys. **17,** 679 (1949); R. C. Lord and J. C. Morrow, J. Chem. Phys. **26,** 230 (1957); I. Simon and H. O. McMahon, J. Chem. Phys. **21,** 23 (1953). These references contain references to earlier work on the Polymorphs of SiO_2.

[2] L. Coes, Jr., Science **118,** 131 (1953); R. B. Sosman, Science **119,** 738 (1954).

[3] A. W. Laubengayer and G. S. Morton, J. Am. Chem. Soc. **54,** 2303 (1932).

[4] W. Zachariasen, Z. Krist. **67,** 226 (1928).

[5] J. J. Kirkland, Anal. Chem. **27,** 1537 (1955).

[6] R. W. G. Wyckoff, Z. Krist. **62,** 189 (1925).

[7] T. F. W. Barth, Am. J. Sci. **23,** 350 (1932); **24,** 102 (1932).

[8] For a discussion of vibrational selection rules and vibrational species see G. Herzberg, Infrared and Raman Spectra, D. Van Nostrand Co. (1945).

[9] R. E. Gibbs, Proc. Roy. Soc. [A] **113,** 351 (1927).

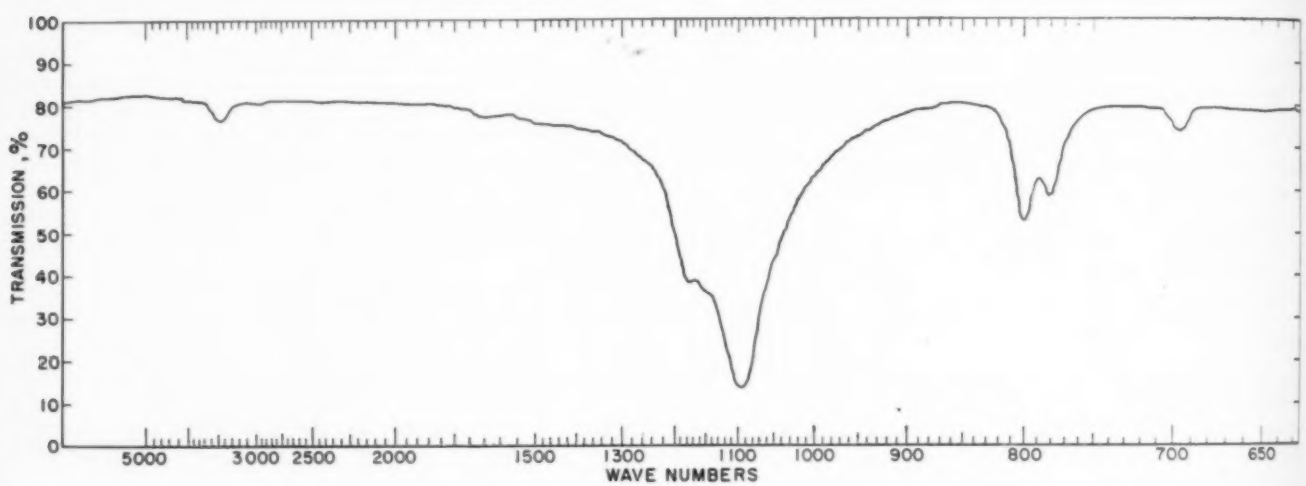

FIGURE 1. *Infrared transmission spectrogram of quartz from Lisbon, Md.*

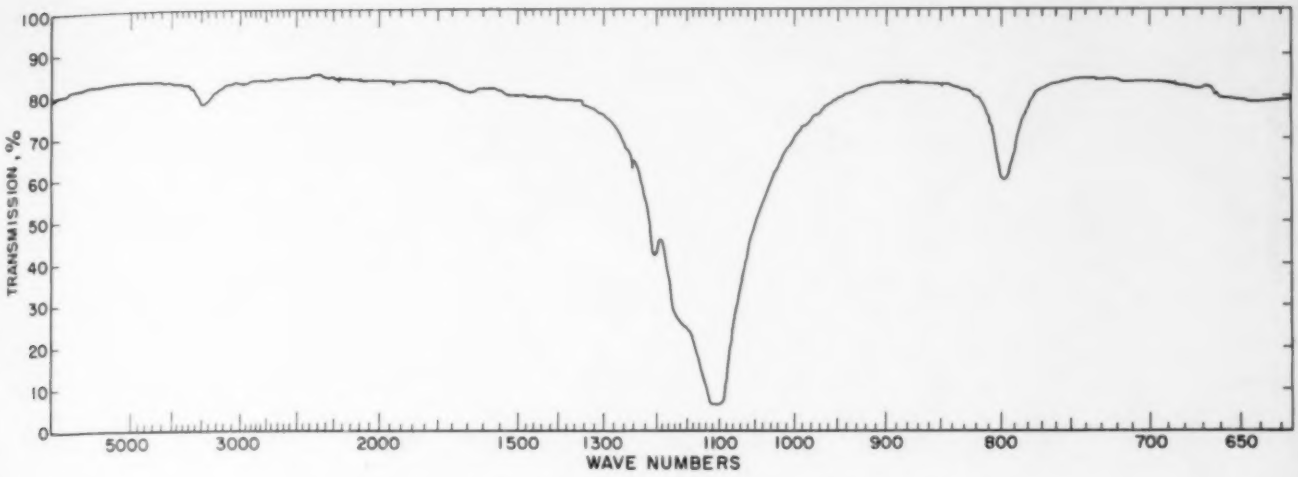

FIGURE 2. *Infrared transmission spectrogram of cristobalite.*

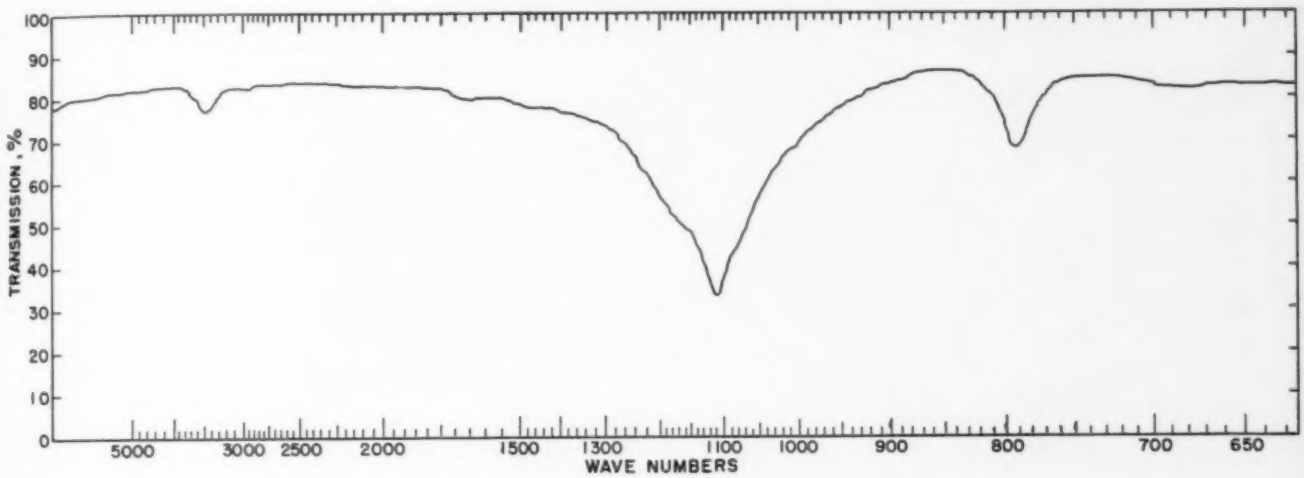

FIGURE 3. *Infrared transmission spectrogram of tridymite.*

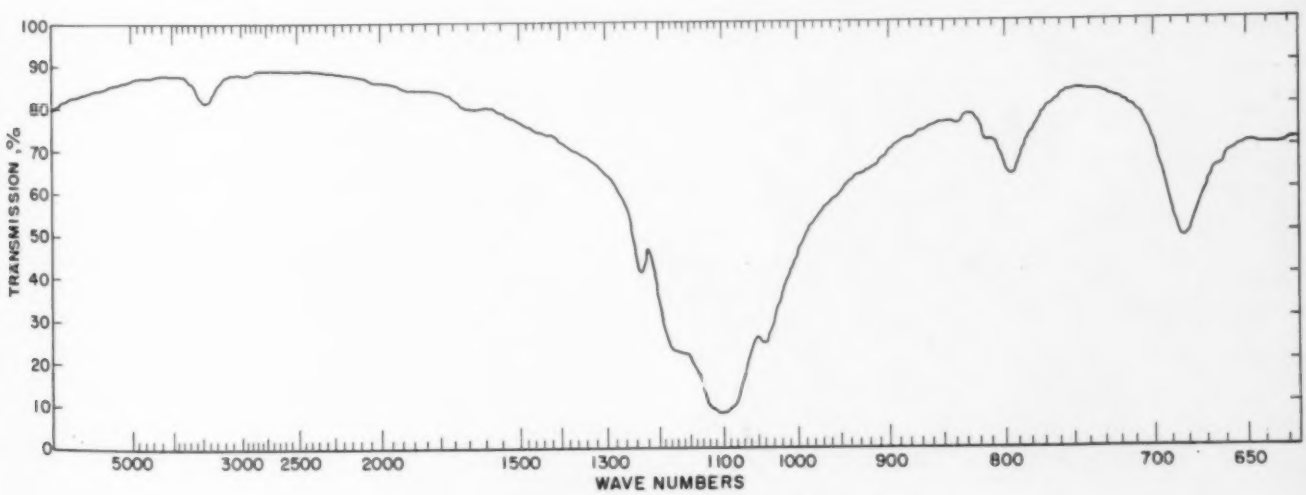

FIGURE 4. *Infrared transmission spectrogram of coesite.*

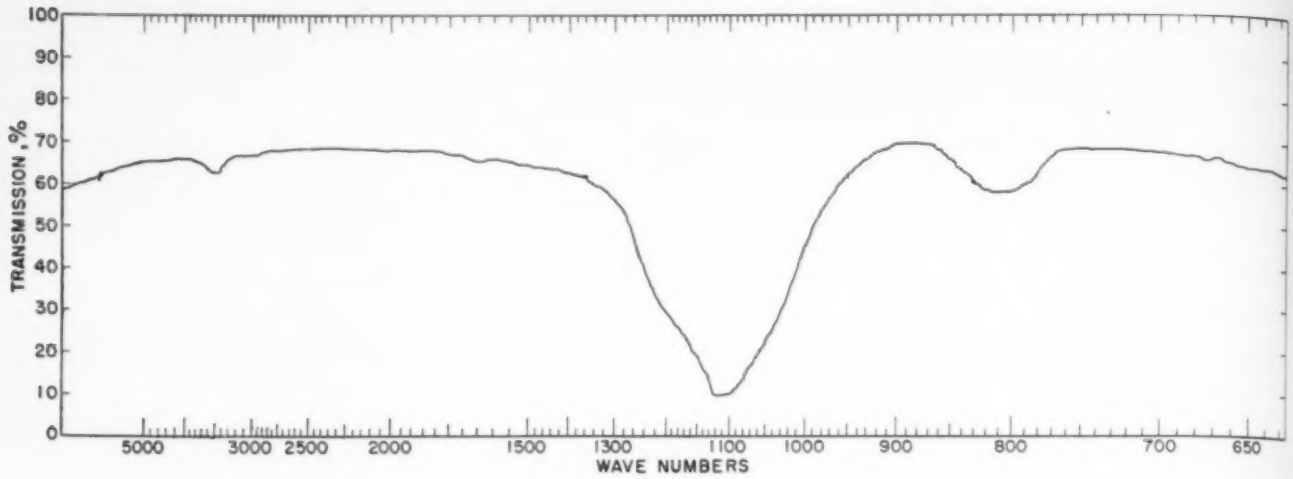

FIGURE 5. *Infrared transmission spectrogram of vitreous* SiO_2.

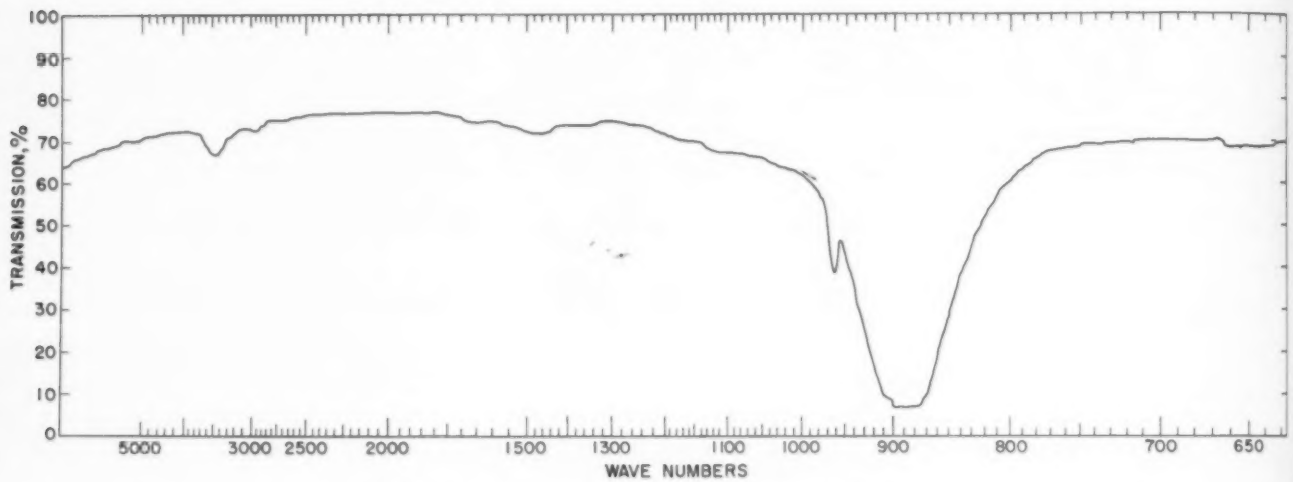

FIGURE 6. *Infrared transmission spectrogram of hexagonal* GeO_2.

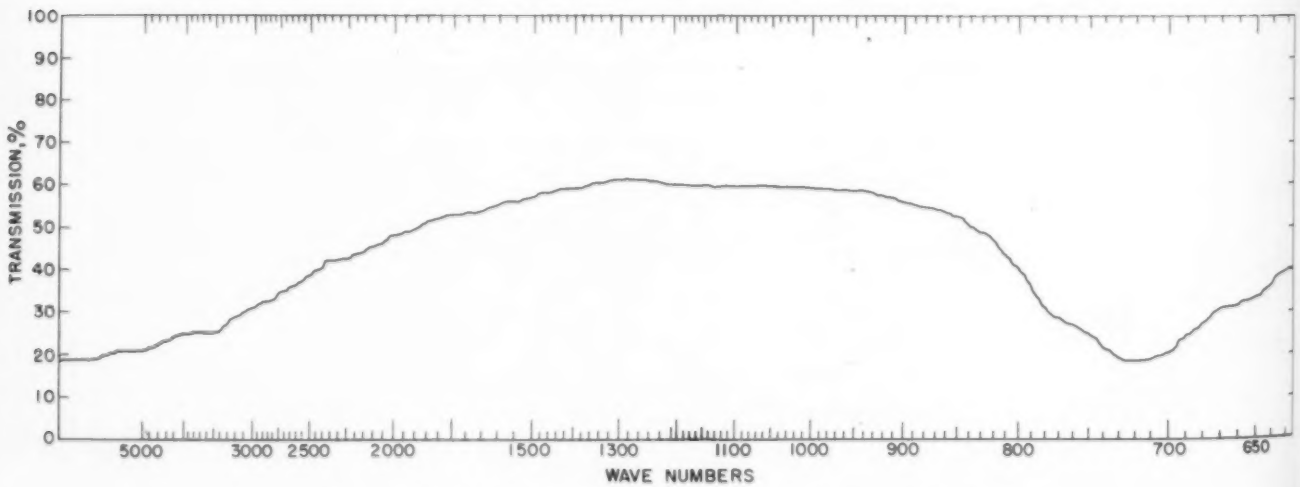

FIGURE 7. *Infrared transmission spectrogram of tetragonal* GeO_2.

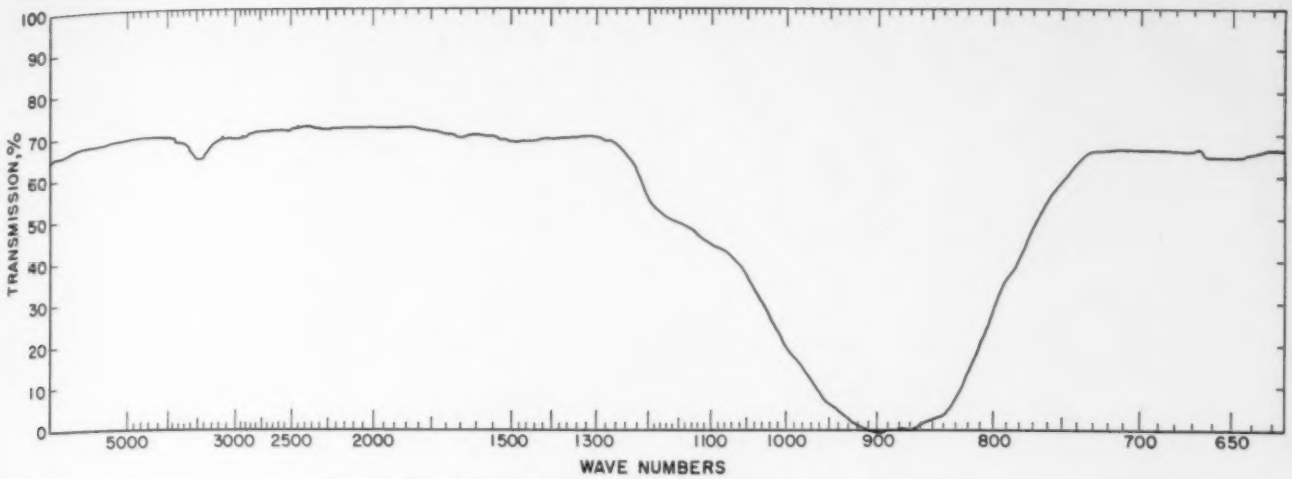

FIGURE 8. *Infrared transmission spectrogram of vitreous* GeO_2.

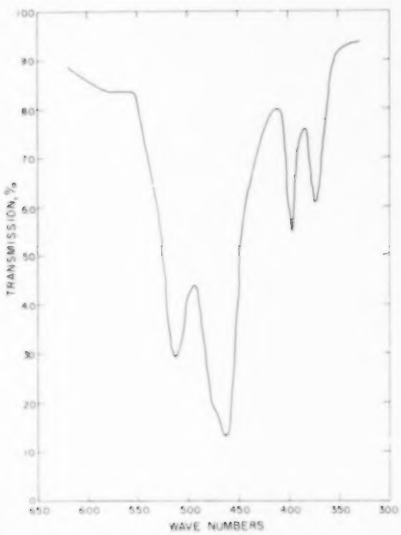

FIGURE 9. *Infrared transmission spectrogram of quartz.*

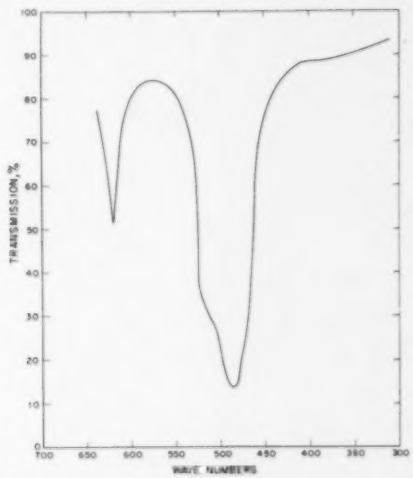

FIGURE 10. *Infrared transmission spectrogram of cristobalite.*

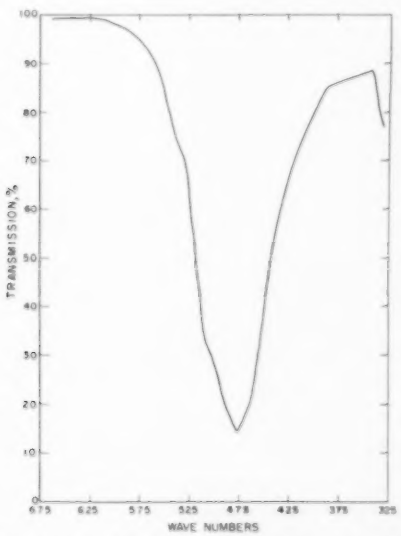

FIGURE 11. *Infrared transmission spectrogram of tridymite.*

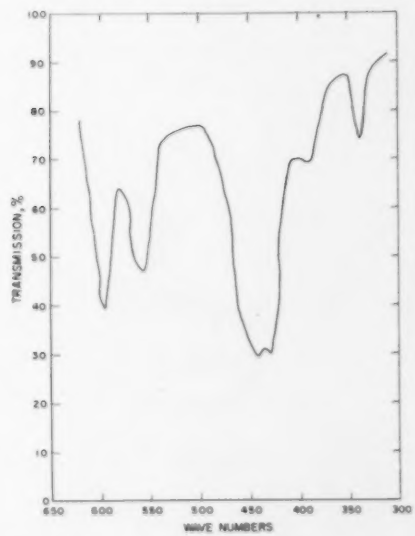

FIGURE 12. *Infrared transmission spectrogram of coesite.*

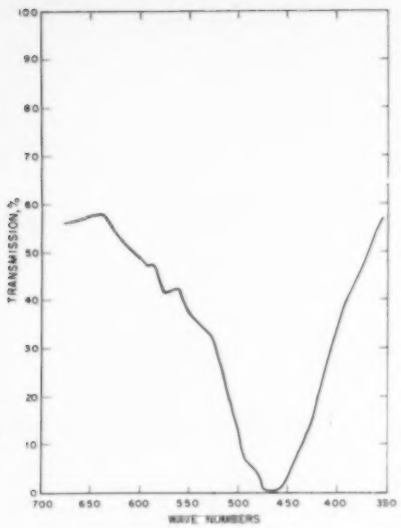

FIGURE 13. *Infrared transmission spectrogram of vitreous* SiO_2.

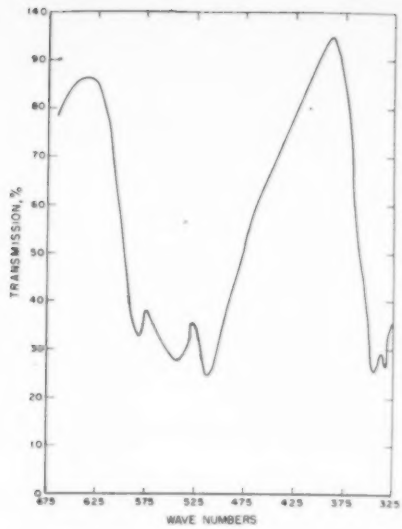

FIGURE 14. *Infrared transmission spectrogram of hexagonal* GeO_2.

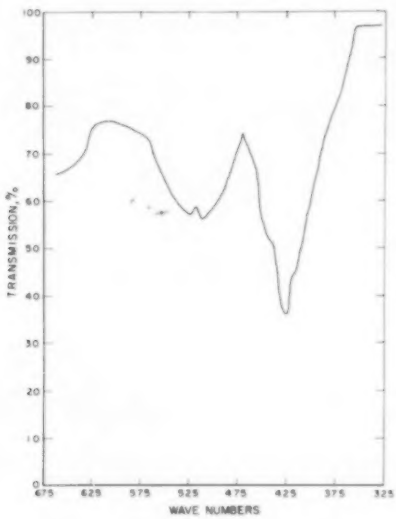

FIGURE 15. *Infrared transmission spectrogram of tetragonal* GeO_2.

WASHINGTON, March 28, 1958.

hexagonal

THE NATIONAL BUREAU OF STANDARDS

The scope of activities of the National Bureau of Standards at its headquarters in Washington, D. C., and its major laboratories in Boulder, Colorado, is suggested in the following listing of the divisions and sections engaged in technical work. In general, each section carries out specialized research, development, and engineering in the field indicated by its title. A brief description of the activities, and of the resultant publications, appears on the inside of the front cover.

WASHINGTON, D. C.

Electricity and Electronics. Resistance and Reactance. Electron Devices. Electrical Instruments. Magnetic Measurements. Dielectrics. Engineering Electronics. Electronic Instrumentation. Electrochemistry.

Optics and Metrology. Photometry and Colorimetry. Optical Instruments. Photographic Technology. Length. Engineering Metrology.

Heat. Temperature Physics. Thermodynamics. Cryogenic Physics. Rheology. Engine Fuels. Free Radicals Research.

Atomic and Radiation Physics. Spectroscopy. Radiometry. Mass Spectrometry. Solid State Physics. Electron Physics. Atomic Physics. Neutron Physics. Nuclear Physics. Radioactivity. X-rays. Betatron. Nucleonic Instrumentation. Radiological Equipment.

Chemistry. Organic Coatings. Surface Chemistry. Organic Chemistry. Analytical Chemistry. Inorganic Chemistry. Electrodeposition. Molecular Structure and Properties of Gases. Physical Chemistry. Thermochemistry. Spectrochemistry. Pure Substances.

Mechanics. Sound. Mechanical Instruments. Fluid Mechanics. Engineering Mechanics. Mass and Scale. Capacity, Density, and Fluid Meters. Combustion Controls.

Organic and Fibrous Materials. Rubber. Textiles. Paper. Leather. Testing and Specifications. Polymer Structure. Plastics. Dental Research.

Metallurgy. Thermal Metallurgy. Chemical Metallurgy. Mechanical Metallurgy. Corrosion. Metal Physics.

Mineral Products. Engineering Ceramics. Glass. Refractories. Enameled Metals. Concreting Materials. Constitution and Microstructure.

Building Technology. Structural Engineering. Fire Protection. Air Conditioning, Heating, and Refrigeration. Floor, Roof, and Wall Coverings. Codes and Safety Standards. Heat Transfer.

Applied Mathematics. Numerical Analysis. Computation. Statistical Engineering. Mathematical Physics.

Data Processing Systems. SEAC Engineering Group. Components and Techniques. Digital Circuitry. Digital Systems. Analog Systems. Application Engineering.

• Office of Basic Instrumentation.

• Office of Weights and Measures.

BOULDER, COLORADO

Cryogenic Engineering. Cryogenic Equipment. Cryogenic Processes. Properties of Materials. Gas Liquefaction.

Radio Propagation Physics. Upper Atmosphere Research. Ionospheric Research. Regular Propagation Services. Sun-Earth Relationships. VHF Research.

Radio Propagation Engineering. Data Reduction Instrumentation. Modulation Systems. Navigation Systems. Radio Noise. Tropospheric Measurements. Tropospheric Analysis. Radio Systems Application Engineering. Radio Meteorology.

Radio Standards. High Frequency Electrical Standards. Radio Broadcast Service. High Frequency Impedance Standards. Electronic Calibration Center. Microwave Physics. Microwave Circuit Standards.

Recent Publications of the National Bureau of Standards

Periodicals

Journal of Research of the National Bureau of Standards, Volume 60, No. 5, May 1958 (RP2857 to RP2866 incl.). 60 cents. Annual subscription $4.00, $1.25 additional for foreign mailing.

Technical News Bulletin, Volume 42, No. 5, May 1958. 10 cents. Annual subscription $1.00, 35 cents additional for foreign mailing.

Basic Radio Propagation Predictions for August 1958. Three months in advance. CRPL-D 165. Issued May 1958. 10 cents. Annual subscription $1.00, 25 cents additional for foreign mailing.

Circulars

Supplement to NBS Circular 460. Publications of the National Bureau of Standards July 1, 1947 to June 30, 1957. $1.50.*

C467, vol. III. Atomic energy levels. $2.50*

Applied Mathematics Series

AMS52. Integrals of airy functions. 25 cents.*

Available from the Superintendent of Documents, U. S. Government Printing Office, Washington 25, D. C. The three NBS periodicals are available on a 1-, 2-, or 3-year subscription basis, although no reduction in rates can be made.

**Foreign postage, one-fourth additional.*

UNIVERSITY OF MICHIGAN
GENERAL LIBRARY
DOCUMENTS DIVISION
1276 ANN ARBOR MICH

UNITED ST
GOVERNMENT PRIN
DIVISION OF PUBLIC DOCUMENTS
WASHINGTON 25, D. C.

OFFICIAL BUSINESS

PENALTY FOR PRIVATE USE TO AVOID PAYMENT OF POSTAGE, $300 (GPO)

Journal of Research of the National Bureau of Standards Vol. 61, No. 1 July 1958

Contents

		Page
The system lime-alumina-water at 1° C. Elmer T. Carlson.	RP2877	1
Heat content of zirconium and of five compositions of zirconium hydride from 0° to 900° C. Thomas B. Douglas and Andrew C. Victor.	RP2878	13
Uniform transient error. Edith L. R. Corliss.	RP2879	25
Optical T-bench method of measuring longitudinal spherical aberration. Francis E. Washer.	RP2880	31
Mass spectrometric study of the rate of thermal decomposition of hydrazoic acid. J. L. Franklin, Vernon H. Dibeler, and Preston P. Morris, Jr.	RP2881	41
Erosion damage to solids caused by high-speed collision with rain. Olive G. Engel.	RP2882	47
Emission spectrum of carbon monoxide from 2.3 to 2.5 microns. Earle K. Plyler, Harry C. Allen, Jr., and Eugene D. Tidwell.	RP2883	53
Further studies of the influence of a ridge on the low-frequency ground wave. James R. Wait and Anabeth Murphy.	RP2884	57
Infrared studies of polymorphs of silicon dioxide and germanium dioxide. Ellis R. Lippincott, Alvin Van Valkenburg, Charles E. Weir, and Elmer N. Bunting.	RP2885	61

[A list of recent NBS publications is given on page 3 of the cover.]

For sale by the Superintendent of Documents, U. S. Government Printing Office, Washington 25, D. C. Price 60 cents (single copy). Subscription price: $4.00 a year; $1.25 additional for foreign mailing.

UNITED STATES GOVERNMENT PRINTING OFFICE, WASHINGTON : 1958